Solubility of Nickel in Mg-Al, Mg-Al-Fe, and Mg-Al-Mn Systems

Dr.ing. thesis

Harsharn Singh Tathgar

February, 2001

Department of Materials Technology and Electrochemistry
Norwegian University of Science and Technology
IME-Rapport 2001:25

This thesis has been submitted to the Department of Materials Technology and Electrochemistry, Norwegian University of Science and Technology (NTNU), in partial fulfilment of the requirements for the doctoral degree “Doktor Ingeniør”

Preface

This work was carried out at the Department of Materials Technology and Electrochemistry at the Norwegian University of Science and Technology in close cooperation with SINTEF Materials Technology, Department of Process Metallurgy. The financial support by Norsk Hydro and the Research Council Norway under PROSMAT Cast House Technology programs is gratefully acknowledged.

I would like to thank my supervisor Professor Thorvald Abel Engh for excellent guidance. He has always had time for help and discussions and it would not be possible to have finished this work without his help.

I would like to thank Dr. Per Bakke at the Mg-MT division at the Norsk Hydro Research Centre in Porsgrunn for his guidance and support through my whole research period. I would like to thank my colleagues and friends at SINTEF Materials Technology, in particular Dr. Eivind Øvrelid (presently at SiNor A/S, Glomfjord) for helping me from the first day at the Department in every field. Dr. Frede Frisvold (Presently at Ålesund College) is thanked for proof reading of my publications, and manuscript and help in using various computer programmes. Mr. Jo Fenstad is thanked for help in conducting solubility measurements. Dr. Martin Syvertsen is thanked for help with statistical analysis of experimental data. I would like to thank Mr. Snorre Farner, who has been my roommate during my four years study for his cooperation. Mr. Morten Raanes is thanked for conducting careful Microprobe analysis of samples.

Parts of this thesis have been published:

Tathgar, H. S., Bakke, P., and Engh, T. A., (2000), "Impurities in Magnesium and Magnesium based Alloys and their Removal", *Magnesium Alloys and their Applications, Ed.: K. U. Kainer,* 5th Intl. Magnesium Conference, Munich, Germany, pp.767-779.

Tathgar, H. S., Bakke, P., Øvrelid, E., Fenstad, J., Frisvold, F., and Engh, T. A., (2000), "Solubility of Nickel in Molten Magnesium-Aluminium Alloys above 650°C", *Magnesium Technology 2000. Ed.: H.I. Kaplan, J. Hryn, and B. Clow,* TMS-AIME, Warrendale, PA, USA, pp. 181-189.

Trondheim, February 5, 2001

Harsharn S. Tathgar

Table of contents

Chapter 3

Chapter 4

Chapter 5

Chapter 6

Chapter 10

Chapter 11

APPENDIX A

List of Symbols

a	Particle radius	m
a_i	Activity of component i	
A	Fitting parameter	
B	Fitting parameter	
D	Diffusion Coefficient	m^2/s
e_i^j	First order Gibbs free energy interaction coefficient of component i on j (wt.% basis)	
E_{AB}	Bond energies between atoms A and B	J/mol
f_i	Activity coefficient of component i (wt.% basis)	
g	Gravitational constant	m/s^2
G	Gibbs energy	J/mol
G_m	Molar Gibbs energy	J
$\overline{G}_i$	Partial molar Gibbs energy of component i	J/mol
ΔG^{ex}	Integral excess molar Gibbs energy of a solution	J/mol
ΔG^{M}	Integral molar Gibbs energy change due to mixing of the components to form a solution	J/mol
ΔG°	Standard Gibbs energy of solution	J/mol
$\Delta \overline{G}_i$	Partial molar Gibbs energy of solution of component i	J/mol
$\Delta \overline{G}_i^{ex}$	Partial molar excess Gibbs energy of solution of component i	J/mol
$\Delta \overline{G}_i^{ideal}$	Partial molar ideal Gibbs energy of solution of component i	J/mol
H	Enthalpy function	J/mol
ΔH^{M}	Enthalpy of mixing	J/mol
ΔH°	Standard enthalpy of solution	J/mol
$\Delta \overline{H}_i$	Partial molar enthalpy of solution of component i	J/mol
I	Probe current	Amperes
[%i]	Mass percent of i in melt	100 kg i/kg melt
(%i)	Atomic% i in particle	100 kg i/kg particle

K	Distribution coefficient	
K	Equilibrium constant	
L	Settling distance	m
M	Number of fitting parameters	
M	Amount of melt	Kg
M_i	Atomic weight of component i	kg/kmol
M_p	Mass of particles	Kg
n	Number of sampled data sets for bootstraping	
N	Number of measurements	
N_i	Number of moles of component i	
N_A	Avogadro's number	
P	Pressure	bar, atm
P_i	Partial pressure of component i	bar, atm
R	Gas constant	8.314 J/mol K
R^2	Correlation coefficient	
$\Delta S°$	Standard entropy of solution (J/molK)	
$\Delta \bar{S}_i$	Partial molar entropy of solution of component i	J/mol
$\Delta \bar{S}_i^{ex}$	Partial molar excess entropy of solution of component i	J/mol
$\Delta \bar{S}_i^{ideal}$	Partial molar ideal entropy of solution of component i	J/mol
t	Time	s
T	Temperature	K, °C
V_s	Settling velocity	m/s
WD	Working distance	mm
X_i	Mole fraction of component i	
z	Distance	m
z	Coordination number	
α	Regular solution constant	
γ_i	Raoultian activity coefficient (mole fraction basis)	
γ_i^0	Raoultian activity coefficient (mole fraction basis) at infinite dilution	
ε_i^j	First order Gibbs free energy interaction coefficient of component i on j (mole fraction basis)	
μ_i	Chemical potential of component i	J/mol
μ	Dynamic viscosity	kg/ms
μ_i^α	Chemical potential of component i in phase α	J/mol

ν	Kinematic viscosity	m^2/s
ρ	Density	kg/m^3
$\Delta\rho$	Density difference	g/cm^3
Ω	Parameter of regular solution	

Abstract

Introduction

The corrosion properties of magnesium alloys strongly depend on the alloy composition and impurities. Heavy elements like nickel, and iron have low solubility in solid magnesium. The dissolved elements in molten magnesium precipitate out on solidification and form intermetallic particles that are the cause of corrosion. Iron content should be kept below the standards specified by ASTM B94/94 using aluminium and manganese. Manganese forms intermetallic particles with iron and aluminium thereby lowering the solubility of iron, and these particles are cathodic compared to magnesium matrix. No method for the removal of nickel has been known previously. Dissolution was the only method to lower the nickel content.

Published solubility data for nickel in pure magnesium is inconsistent and not available for magnesium alloys. Therefore various systems are studied to determine the behaviour of nickel in Mg-Al alloys. Methods for removal of nickel from Mg-Al alloys are also discussed.

Mg-X, Mg-Ni systems

Partial excess Gibbs energies of dissolution of various elements *i* in magnesium are presented in Table 3.1. The activity coefficients calculated at 1000K are also given.

Standard Gibbs energy for the solution of 1 mass% nickel in liquid magnesium calculated from activity data by Feufel (1993) is found to be:

$$\mathrm{Ni(s)} = \underline{\mathrm{Ni}} \qquad \Delta\overline{G}^{\circ}(\%) = -43500 - 22.2T$$

Standard Gibbs energy for the solution of 1 mass% nickel in liquid magnesium calculated from Kubachewski et al. (1993) is more negative and is:

$$\mathrm{Ni(s)} = \underline{\mathrm{Ni}} \qquad \Delta\overline{G}^{\circ}(\%) = -25375 - 55T$$

Mg-Al-Ni system in Al_2O_3 crucible

Solubility of nickel in liquid Mg-Al alloys has been measured in the temperature range 650-900°C and for 1-10% Al content. Compared to pure magnesium the solubility in Mg-Al alloys shows a marked reduction. Addition of only 1 wt.% Al re-

duces nickel solubility from about 37.5 wt.% to about 0.52 wt.% at 700°C whereas at 5 wt.% Al the solubility further reduces to 0.22 wt.%.

SEM-analysis of samples taken at various temperatures and compositions shows that the precipitated phases in equilibrium with the melt are AlNi and Al_3Ni_2 with the latter becoming more dominant as the aluminium concentration increases. The solubility of nickel in the melt in equilibrium with AlNi is given according to the dissolution reaction AlNi = Al + Ni. Thermodynamic data for the equilibrium between a liquid solution of Mg-Al-Ni and precipitated AlNi solid intermetallic compound is determined.

Mg-Ni-X system in iron capsule

In an iron capsule the possibility of removing dissolved nickel from (pure) magnesium has been studied by precipitating with another element X in a temperature range 660-800°C. Element X in this study was Zr, Mo, Mn, V, Hf, Ti or Ta. X was always present as a separate phase (in excess). ICP-AES and SEM analysis of samples treated with molybdenum, tantalum, and hafnium did not show any removal of nickel.

Manganese forms a γ(Fe,Mn) phase containing small amounts of nickel. The results with vanadium indicate that vanadium can remove iron even though the solubility of vanadium in magnesium is low.

The ICP-AES analysis results show the reduction of nickel from 200 ppm to less than 50 ppm in the case of zirconium. SEM analysis of samples treated with zirconium indicate the presence of various Zr-Fe phases also containing nickel. Titanium also reduces the nickel content to some extent.

Compositions of the phases formed are determined by quantitative analysis in SEM and are compared with phase diagrams. From the SEM analysis it is found that zirconium and titanium dissolve in magnesium and form various intermetallic phases with dissolved iron. Microprobe investigations confirmed the formation of Fe-Zr particles also containing nickel.

In summary, zirconium and titanium remove nickel from magnesium by forming various phases with iron also containing nickel. The various intermetallic phases identified are Zr_2(Fe,Ni), Zr_3(Fe,Ni), Zr_4(Fe,Ni), Ti(Fe,Ni) and Ti(Fe,Ni)$_2$.

Mg-Al-Ni-Fe system in Al_2O_3 crucible

The solubilities of iron and nickel in Mg-Al alloys has been measured in the temperature range 650-900°C and 0.70-9.01 wt.% Al content. The amount of iron and nickel was added such that there was an excess of these elements at 900°C. Microprobe analysis of the samples shows that the precipitated phase in the composition and temperature range is $Al(Ni_{0.89},Fe_{0.11})$. The Gibbs energy for the formation of $Al(Ni_{0.89},Fe_{0.11})$ phase in Mg-Al alloys is close to that of the AlNi phase.

Mg-Al-Ni-Mn system in Al_2O_3 crucible

The solubilities of nickel and manganese in Mg-Al alloys has been measured in the temperature range 650-900°C and 0.38-10.7 wt.% Al content. The amount of manganese and nickel was added such that there was an excess of these elements at 900°C. 'Line compounds' are determined using solubility data at various aluminium contents, and their Gibbs energy of formation is presented.

Mg-Al-Ni-Fe-X system in iron capsule

The possibility of removing nickel from Mg-Al alloys has been studied by precipitating with another element X in a temperature range 670-800°C. Element X in this study was Cr, Zr, Mo, Mn, V, Hf, RE, Ti or Ta, and there was always an excess of element X in the melt. Some samples were treated without any addition of element X.

For aluminium contents between 3-5%, FeAl is the equilibrium phase in Mg-Al alloys saturated with iron. Addition of elements Ta, Cr, Hf, V, Ti and small amounts of Mn do not seem to significantly change the composition of the precipitated FeAl particles. Higher amounts of Mn, RE and Zr give precipitates different from FeAl.

The results indicate that nickel in the FeAl particles may be regarded as an ideal solution of NiAl in FeAl.

Chapter 1

Introduction

There is a continuous increase in the demand for magnesium. The international Magnesium Association (IMA) shipments in 1998 showed an 8% increase from the previous record set in 1997, to 360,300 MT (metric ton) (Edgar 1999). The magnesium die casting industry has grown significantly over the past several years. IMA shipments to the die casting segment in 1998 increased by 14,800 MT or 15.5%. The automotive industry accounts for 90% of the casting demand (Edgar 1999). While this consumption generates considerable amounts of process scrap today, it will in the long turn give significant amounts of postconsumer magnesium scrap as well. Unlike in aluminium, there are no real markets for secondary magnesium alloys, forcing the recycling processes to be capable of regaining the original chemical composition and cleanliness of the magnesium alloys. Molten metal refining is thus an important step in recycling. Magnesium growth will be more economical and environmentally accepted if all the options for re-using pre- and post-consumer scrap are exploited. The primary objective of any magnesium die-casting company is to make the maximum use of magnesium alloy ingot. As a result, several processes are already in use to recycle die casting magnesium returns (Brassard and Riopelle 1997). In this chapter, impurities (dissolved elements and inclusions) in magnesium and magnesium-based alloys are reviewed; their origin, their effects on properties, and their removal. Principles for removal of inclusions and dissolved elements by means of flux and without flux are highlighted. Technologies used in the magnesium industry today, including gas purging and refining by salt, illustrate the principles.

Recycling in general, and used scrap recycling in particular, may result in contamination of the recycled metal. Pure magnesium is highly corrosion resistant but small amounts of iron, nickel, copper, and cobalt have deleterious effects on corrosion properties (Emley 1966, p. 670). The solubility of these elements is small in solid magnesium alloys and therefor intermetallic particles are formed on cooling molten magnesium containing impurity elements. Byun et al. (1997) have shown that manganese has a positive effect on the removal of iron from magnesium and magnesium-alu-

minium alloys. Aluminium and manganese form various intermetallic compounds also containing iron that are heavier than magnesium alloy melts. Hence these intermetallic compounds are removed by settling. The iron content in equilibrium with the Mg-Al-Mn melts is lower than the limit specified by ASTM (American Society for Testing of Metals) B-93 standards (Tathgar et al. 2000b). The possibility of removing nickel using aluminium and the effect of other elements for example; manganese, iron, zirconium, molybdenum, vanadium, hafnium, titanium, tantalum and chromium will be discussed in the following chapters.

Lubricants, inserts, and paints, as well as occasionally failing sorting routines may introduce new and uncommon elements. Clean scrap generated at die casting plants, i.e. runners, biscuits, trimmings and rejected cast (Class 1 scrap (Pinfold and Øymo 1993)) is supposed not to contain painted or lacquered scrap, machine turnings or cast parts containing inserts of foreign materials. However, significant nickel pick-up may take place due to contact with nickel-containing tools during molten metal processing. Also, there might be a chance for metallic contamination during sorting. As an example, electroplated magnesium alloy components in mobile phones may contain up to 1% nickel by mass.

Hanawalt et al. (1942) have shown that the corrosion resistance of pure magnesium is considerably reduced if the nickel content increases to more than 8 ppm. For alloys, ASTM B-93 standards specify nickel concentrations below 0.001 wt.% (14 ppm) for magnesium alloy die-casting ingots, whereas the upper limits for nickel in die-cast parts is 0.002 wt.% (24 ppm) (Aune et al. 1997).

At 650°C liquid magnesium dissolves about 32 wt.% nickel (Nayeb-Hashemi and Clark 1988, pp. 219-225). The ternary system Mg-Al-Ni has not been investigated in detail for the magnesium-rich alloys. However, it may be anticipated that aluminium significantly reduces the solubility of nickel because aluminium and nickel form intermetallic phases (Massalski 1990, pp. 181-184) having high melting points.

Melting and recycling of magnesium is very often carried out in iron crucibles so there will always be iron in contact with the alloy. The content of iron will depend on the temperature and alloying elements. At 650°C the solubility of iron in pure magnesium is 0.018 wt.% (Nayeb-Hashemi and Clark 1988, pp. 118-121). Both iron and nickel are detrimental elements with respect to corrosion. ASTM B-93 standards specify iron concentrations below 0.004 wt.% for magnesium alloy die-casting ingots (Aune et al. 1997). Byun et al. (1997) have shown the effect of aluminium on the solubility of iron. As mentioned previously the solubility of iron decreases significantly with an increase in aluminium content. In Mg-Al-Fe systems the precipitated phases in equilibrium with liquid Mg-(2-4%)Al and Mg-(6-9%)Al alloys are FeAl and $FeAl_2$, respectively (Byun et al. 1997). As iron will always be present in

the magnesium alloys held in iron crucibles it is important to study the mutual solubility of iron and nickel in magnesium-aluminium alloys.

Various methods for removing iron are employed commercially but at present no method for removal of nickel is known. Hanawalt et al. (1941) have shown that there is a critical proportion of iron, e.g. about 0.002 wt.% in the case of Mg-Al alloys, below which these alloys are highly corrosion resistant. It was shown that iron is soluble to an extent well below 0.002 wt.% in molten magnesium and magnesium based alloys when these metals are saturated with manganese.

Simensen et al. (1989) have shown the effect of iron in Mg-4 wt.%Al-Mn alloys. For manganese concentrations larger than 0.15 wt.% and above 750°C the equilibrium phase is β–Mn(Al) containing iron. Below 750°C the equilibrium phase is $Al_8(Mn,Fe)_5$.

1.1 Impurities in Magnesium

Impurity elements are defined as elements present in solution in the molten alloy that have deleterious effects on the metal properties (Aune et al. 1997). Impurities in metals can be classified into five main groups (Engh 1992, p. 2):

I Volatile elements
II Reactive elements
III Non-reactive elements
IV Reactive Inclusions
V Non-reactive inclusions

Inclusion types in magnesium and magnesium based alloys have been reviewed (Bakke and Karlsen 1997) emphasising the methods for sampling and quantitative assessment of inclusions. The most important inclusions in magnesium and magnesium based alloys are:

-Oxides, appearing as lumps, films and apparently loosely connected agglomerates or clusters
-Intermetallic particles
-Chlorides

The double oxide $MgO.Al_2O_3$ (spinel) is the most stable oxide in magnesium alloyed with aluminium. Nitrides, carbides, sulphates, sulphides and fluorides are rarely discovered.

1.1.1 Sources of Impurities

All the elements in the periodic table are present in magnesium in small or trace amounts (Simensen 1981). There are a number of ways that inclusions and dissolved elements may enter magnesium including natural occurrence and carry-over from the raw materials, the smelting process, alloying, and primary ingot casting; in the die casting shop: remelting of ingots, holding and casting. Recycling, of course, needs special attention.

1.1.1.1 Oxidation

The oxide film on magnesium is protective below 450°C in dry oxygen and below 380°C in moist oxygen for considerable lengths of time (300 hours). At higher temperatures, thickening of the film results in loss of protection, and thereafter oxidation proceeds linearly with time, which means that the oxide formed on magnesium is non-protective against further oxidation, contrary to the case for aluminium (Kubaschewski and Hopkins 1962, p. 208).

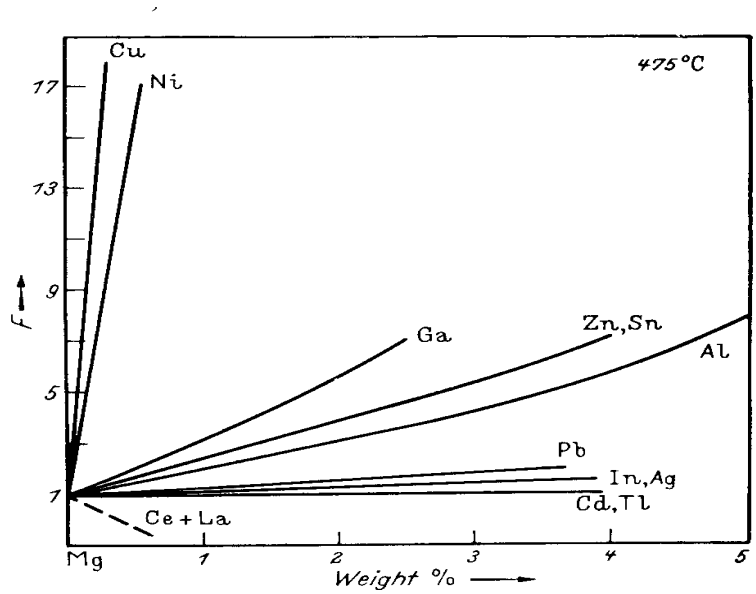

Figure 1.1: Effect of various metals on the oxidation of solid magnesium (Kubaschewski and Hopkins (1962), values taken from Leontis and Rhines (1946). F is the effect of additions on the linear oxidation relative to pure Mg).

Kubaschewski and Hopkins (1962) have demonstrated the effect of alloying elements on the oxidation of solid magnesium at a temperature of 475°C (see Figure 1.1). F is the amount of magnesium oxidized compared to pure magnesium. All of

the alloying elements were nobler than magnesium itself and most of them were present in a single concentration only (ca. 3.8%). The oxidation took place at the metal-oxide interface. Only cerium + lanthanum, which lower the oxidation rate of magnesium a little, were enriched in the surface layer. All the other elements were present in both phases but with smaller concentrations in the surface layer. The increase in oxidation rate is explained by the lowering of melting point by the addition of the alloying elements except for cerium and lanthanum. Ichikawa and Saito (1965) have studied the concentration gradient of beryllium from the surface and into the metal at various atmospheres and various temperatures. Their findings indicate that in the presence of oxygen containing atmospheres there will be a segregation of beryllium towards the magnesium surface even in solid state.

Hallstedt (1993) estimated the solubility of oxygen in mole fraction to be $2.2*10^{-9}$ in liquid magnesium at the melting point. The solubility at the melting point estimated by other authors differs by almost four orders of magnitude. This gives a hint of the uncertainty of the estimates.

Molten magnesium is volatile and reacts with oxygen to create MgO when the melt is exposed to the atmosphere. Oxidation of magnesium accelerates dramatically as the temperature increases beyond 650°C (Hu and Luo 1996). Removal of dross and sludge may result in the formation and introduction of oxide inclusions.

As mentioned earlier there are three types of oxides (solid lumps, clusters, and oxide films) present in magnesium (Øymo et al. 1994). Solid lumps of magnesium oxide probably originate mainly from the electrolytic process and may also be produced during recycling. Due to their large size (>10 μm) and high relative density, the majority of the lumps are easily removed by settling prior to ingot casting. Oxide films are entrained in raw magnesium due to reactions and turbulence occurring on the melt surface. These films are extremely thin, and do not readily settle out.

Oxide films and clusters are entrapped from the melt surfaces when stirring, removing dross or sludge, or ladling (Bakke and Karlsen 1997). Ingots are covered with a layer of oxide that may be introduced in the melt on remelting and charging. Oxide films and oxide clusters have large surface/volume ratios, possibly they are covered by gas films, and thus are not readily removed by settling.

Simensen and Oberländer (1980) have found that MgO is commonly found together with magnesium nitride and chlorides. Thermodynamic calculations indicate that magnesium nitride will not form unless the partial pressure of oxygen becomes extremely low (Bakke and Karlsen 1997). Oxygen in the entrapped air bubbles reacts completely to form MgO, thereby reducing the partial pressure of oxygen to such low levels that nitrogen starts to react. The presence of nitrides is explained by entrapment of air bubbles for instance during melt transfer.

1.1.1.2 Smelting process

Magnesium produced by electrolysis may contain traces of chlorides and oxides carried over from the electrolysis cells. Usually these inclusions are removed in the foundry. In magnesium electrolysis molten magnesium is in contact with iron, thus molten magnesium metal usually contains 200-400 ppm of dissolved iron.

Magnesium produced by silicothermic reduction of magnesium oxide with silicon, for instance, by the Pidgeon process (Emley 1966, pp. 52-57), may sometimes contain silicon in the 300-500 ppm range. Inherent in the silicothermic production is a potential to give very low amounts of other trace elements. However, the pick-up of trace elements like iron and other heavy metals may occur in the foundry. In silicothermic magnesium, oxide inclusions containing CaO can also be observed. This is likely due to the use of dolomite ($MgCO_3.CaCO_3$).

1.1.1.3 Alloy production

Iron contents in the range 200-400 ppm will be present in pure magnesium held in iron crucibles, roughly corresponding to the solubility. In the production of High Purity alloys, manganese together with aluminium are used to remove iron from magnesium. Intermetallic particles containing iron, manganese and aluminium are precipitated. The composition of these particles is dependent on the aluminium content (Holta et al. 1996). Inevitably, some intermetallic particles of micron size as well as dissolved manganese will remain in the magnesium.

As aluminium is added in amounts up to 9 wt.% in the commercial High Purity magnesium alloys, the quality of the aluminium to be added is important. As nickel is a relatively unimportant element in aluminium, it is difficult to avoid introduction of nickel with the alloying of aluminium.

The choice of materials for tools and equipment in the primary casthouse as well as in the die casting shop should emphasise prevention of the pick up trace elements, especially nickel.

1.1.1.4 Ingot casting

Depending on the mould filling technique, turbulence and splashing may cause formation of foam and oxides. Some producers put effort in skimming off the surface just after completed filling to improve the customer's impression of the ingots. Mould coatings that are used for easing the release of the ingots may sometimes attach to ingots. Cold shuts, if present, may give some additional surface.

In AZ91 ingots porosity is concentrated at the top centre of the ingot, along the centre line, but not uniformly distributed along the ingot's length (Bakke et al. 2000a). This porosity, caused by interdendritic flow of low melting point eutectic during the last stages of solidification, is connected to the atmosphere, causing significant additional surface. The finely distributed porosity in magnesium-alloy ingots is the counterpart to the localised cavity in pure magnesium ingots. It is a consequence of ingot casting, and should be considered as a natural part of the ingot.

It may be added that an ingot is not a product as such, it is rather an intermediate storage of metal. This means that there is no one-to-one correspondence in the quality of an ingot and the quality of a cast part.

1.1.1.5 Remelting of ingots in the die casting shop

Remelting of ingots in a die casting shop is not necessarily a straightforward operation. Preheating should eliminate possible surface moisture that may represent a safety hazard. Gentle charging minimises unnecessary splashing and entrapment of surface oxides. Although the reasons are not satisfactorily understood, it is observed that most of the surface of ingots (and scrap) floats to the surface when the parts melt (Hillis and Mercer 2000). This happens in spite of the fact that these impurities should have a density higher than magnesium. Presumably the explanation is that a gas layer attaches to the oxides, thus lowering the mean density. Such gas layers have been detected for Al_2O_3 in aluminium (Haugland 1998, p. 79). The growing layer of oxides on top of the melt puts strong requirements on the household of the furnace(s), including removal of surface dross and bottom sludge. If dross and sludge are not allowed to accumulate, modern transfer and dosing techniques will probably not introduce additional inclusions. However, in cases where hand-ladling is still practised surface oxide may be fed directly to the die casting machine.

Sludge is partly a result of precipitation of intermetallic particles, which is minimised by good temperature control (Holta et al. 1996) and rapid melting. Excellent temperature control can be achieved by melting in one furnace and casting from a second furnace. Temperature gradients generated during charging are thus confined to the melting furnace, and the metal to be cast comes from a constant temperature reservoir. Furthermore, a system like this gives a long and evenly distributed metal residence time, facilitating good and consistent metal quality.

Inclusions are also entrapped during the die casting, due to oxidation in the shot sleeve, entrapment of air during casting, and possibly pick-up of lubricants from the die. In sand casting, sand grains are also picked up due to turbulent flow, thereby also increasing the silicon content in the metal.

1.2 Effects of impurity elements and inclusions

In this section the various impurities and their negative effects on magnesium properties will be discussed, partly in connection with maximum limits set by international standards.

1.2.1 Nickel

Nickel is about 35-75 times as detrimental as copper in promoting corrosion of both die cast and permanent mould cast AZ91 (Bakke et al. 1999) and AZ81 (Höllrigl-Rosta et al. 1980). As mentioned earlier the solubility of nickel in liquid magnesium at 650°C is approximately 32 wt.%. Alloying elements such as aluminium reduce the solubility of nickel considerably. Compared to pure magnesium the solubility of nickel in Mg-Al alloys shows a marked reduction due to the formation of AlNi phase (Tathgar et al. 2000a). For instance the solubility of nickel reduces to 0.15% at 650°C with addition of only 3 wt.% aluminium. To ensure acceptable corrosion properties the ASTM B-93 standards specify nickel concentrations below 0.001 wt.% for magnesium-alloy ingots. For some reason the upper limit for nickel in die-cast parts is 0.002 wt.%.

Manganese in combination with aluminium also reduces nickel levels to some extent but the concentration of nickel in equilibrium with $Al_X(Ni,Mn)_Y$ phases has not been determined. The thermodynamics of molten Mg-Al-Ni-Mn system will be discussed in this thesis.

There are three methods for dealing with the problem of nickel (Foerster 1975). One obvious method is to dilute the nickel-contaminated magnesium metal with substantially pure magnesium until the nickel content is reduced to acceptable levels. Those having access to pure magnesium can use this method. A second method is to remove nickel by distillation of magnesium from nickel. This is presently not of commercial interest. A third method for reducing the nickel content is by precipitation with another element. Zirconium reduces nickel content from about 2% to about 0.2% in pure magnesium is use of zirconium. It is claimed that nickel may be reduced from about 0.2% to as low as 0.001% by adding zirconium and aluminium to the magnesium melt.

Some nickel may precipitate alongside iron in the Al-Mn-Fe phase. However, no industrial process for removal of nickel from molten magnesium base alloys is practised, except for dilution.

1.2.2 Iron

The solubility of iron in pure magnesium is 0.018 wt.% at 650°C increasing to approx. 0.040 wt.% at 750°C (Nayeb-Hashemi and Clark 1988, pp. 118-121). The principles for removing iron by means of manganese and aluminium, thereby getting a considerably more corrosion resistant alloy, was discovered more than 70 years ago (Bakken 1926; Beck and Schmidt 1929). However, the industrial importance of this was not recognised until the 1980's. Holta et al. (1996) have discussed the metallurgical principles for removal of iron by addition of manganese extensively, and investigated the mutual liquid solubilities of iron and manganese in the various alloys. Their results also show that manganese additions beyond the amount needed to bring the iron content below the high purity limits reduce the corrosion resistance. According to Holta et al. (1996), to ensure acceptable corrosion performance of the parts, the maximum iron content should not exceed 0.004 wt.%. ASTM standard B-93 specifies iron concentrations below 0.004 wt.% for most common high purity magnesium alloy ingots, and 0.005 wt.% for die cast parts, allowing for a slight pick-up of iron in the die casting shop.

Hillis and Green (1988) have described a process for removing iron contamination from molten magnesium by adding a mixture of boron-containing compound and a flux. The iron content in the magnesium product can be reduced from about 400 ppm to less than about 10 ppm. Other ways to remove iron reported in the literature include beryllium (AlBe master alloy or $BeCl_2$ (Holdeman 1941)), zirconium (as flux containing $ZrCl_4$ (Fox and Bushrod 1944)) and titanium (as flux containing $TiCl_4$ (Emley and Fox 1945)).

1.2.3 Copper

The solubility of copper in molten magnesium is about 70 wt.% at 650°C (Nayeb-Hashemi and Clark 1988, pp. 94-103). The ASTM B-93 standard specifies copper concentrations below 0.008% for high purity AM alloys and below 0.025 wt.% for die cast parts. Copper has an adverse effect on the corrosion on AZ and AM alloys. However, the sand casting alloys ZC63 contains 3 wt.% copper in addition to 5 wt.% zinc and 0.5 wt.% manganese (Unsworth and King 1986), but the corrosion properties are reported to be acceptable. According to Polmear (1994) most of the copper is incorporated in the eutectic $Mg(Zn,Cu)_2$ phase which appears to be rather harmless. On introducing aluminium, the copper containing phase changes and the Mg-Al-Zn-Cu alloy is heavily attacked by corrosion (Hillis 1983).

Although some copper may precipitate alongside iron in the Al-Mn-Fe phase, there is no known process for removal of copper from magnesium alloys (Bakke et al. 1999).

1.2.4 Cobalt

The elements iron, nickel and copper are quite common in materials that may be considered for use with magnesium. Although cobalt is present in some steels, the main problem with cobalt may be its presence in some paints that may be used on magnesium alloy parts. This may result in contamination during recycling.

Although Hanawalt et al., (1942) showed that cobalt is as harmful as nickel, very little attention has been given to cobalt and no standards are specified for it. Cobalt contents in samples from different producers are reported to be less than 10 ppm (Aune et al. 1997).

Results from Bakke et al. (1999) showed the same effect of nickel and cobalt on AZ91. It should be considered to add cobalt to the list of elements that is specified in international standards. Tentatively, maximum allowed cobalt content should be the same as for nickel.

1.2.5 Hydrogen

Øvrelid (1997, p. 1) points out that there will always be some hydrogen present in magnesium due to pick-up of hydrogen from moisture in the air and in flue gas from gas or oil burners. $MgCl_2$ is strongly hygroscopic and easily picks up water. Dissolved MgOHCl is reduced at the cathode during electrolysis resulting in the evolution of hydrogen. Some of the evolved hydrogen may end up in the metal. When hydrogen from H_2O enters the metal, oxidation also takes place leading to metal losses and possibly contamination of the melt.

Magnesium has a much higher solubility for hydrogen than aluminium. Thus when magnesium is added to aluminium, a considerable amount of hydrogen is added. Aluminium-magnesium alloys with more than 0.15 ppm hydrogen may contain porosity, depending on the casting process. While hydrogen in molten aluminium or Al-Mg alloys may be reduced fairly easily by gas purging, this is not the case in molten magnesium due to unfavourable thermodynamics (Bakke 1992). However, hydrogen in magnesium die-casting is normally not considered a problem as possible hydrogen porosity adds to the porosity usually present anyway. Molten magnesium saturated with hydrogen rejects only 32% during solidification as compared to aluminium that rejects 95% (Øvrelid 1997, p. 7).

1.2.6 Oxides

The impact of oxide inclusions on the mechanical properties of die cast products is extremely difficult to quantify. The reason is that oxides are not the only defect, they normally add to other casting defects such as porosity (Bakke et al. 2000b). Recent findings indicate that depending on the presence of casting defects, deterioration typically starts at 500 ppm of oxides. This is in contrast to earlier findings indicating 2000 ppm as a critical content (Haerle et al. 1996).

1.2.7 Other elements

As mentioned earlier, manganese, zirconium and rare earth metals are beneficial as they reduce the solubility of iron by forming stable compounds with iron and possibly also with aluminium, nickel, cobalt, and copper. Nitrogen, carbon and sulphur may be present as nitrides, carbides, oxides, sulphates and sulphides, while the lightest halogens, alkali metals and alkaline earth metals may be found as salt inclusions.

1.3 Recovery of Magnesium from Scrap

In typical magnesium die-casting operations, only around 50% of the purchased ingot appear as finished castings, the remainder as scrap (King and Thistlethwaite 1994).

Aune et al. (1997) have defined closed-loop recycling as recycling die-caster returns and post-consumer scrap back to a quality needed to produce the same part. Such recycling will inevitably lead to pick-up of trace elements and inclusions. Therefore closed-loop recycling of high-purity magnesium die-casting alloys requires careful control of chemical composition and metal cleanliness. Closed-loop recycling of die-caster returns today is a reality but there are still some challenges. To facilitate closed-loop recycling of post-consumer scrap, it may be required to design vehicles so that dismantling of parts for re-use and recycling becomes more cost competitive.

There are various classification systems for magnesium scrap. King and Thistlethwaite (1994) described a generic classification for typical recyclable material derived by Magnesium Electron. Norsk Hydro has also a quite similar classification system.

Clean scrap generated at die-casting plants, i.e. runners, biscuits, trimmings and rejected cast parts are referred to as Class 1 scrap (Pinfold and Øymo 1993). Rejected castings containing inserts, painted parts, and/or machines turnings, are not included

in Class 1 scrap. Recycling processes in operation today deal mainly with Class 1 scrap. Table 1.1 shows classification of typical recyclable magnesium scrap.

TABLE 1.1: Classification of typical recyclable magnesium scrap.

Category	Description	Content	Others
Class 1A	Dense high-grade clean scrap.	Scrap castings, biscuits etc.	
Class 1B	Clean scrap with high surface area.	Thin wall castings, flashings etc.	
Class 2	Clean scrap with inserts.	Steel/aluminium inserts.	Copper or brass contamination not allowed.
Class 3	Painted castings.	With or without steel/aluminium inserts.	Copper or brass contamination not allowed.

Class 4, 5, and 6 scrap (Table 1.2) are considerably more difficult to recycle, but may be considered for other applications, for instance desulphurization of steel melts.

TABLE 1.2: Types of scrap considerably more difficult to recycle.

Category	Description	Content	Others
Class 4	Unclean metal scrap.	Al alloys, Si and Cu contamination.	Oily and wet.
Class 5A	Chips and swarf machinings.	Clean/dry/uncontaminated.	
Class 5B	Chips, swarfs and machinings.		Oily and/or wet.
Class 6A	Flux-free residues.	Crucible sludge, dross etc.	It should be dry and free from Si.
Class 6B	Flux residues.	Crucible sludge, dross etc.	It should be dry and free from Si.

Most of the scrap produced by die-casters is of Class 1, which is further divided into two categories according to surface area. Class 2 scrap is not easily recyclable. Direct remelting of painted scrap (Class 3) is prohibited by European legislation. It is necessary to remove all coating material prior to melting. Magnesium die-castings, which are coated with nickel, are not included in any of the above categories. Recycling of class 4 material always requires some manual pre-sorting to remove non-magnesium contaminants before further treatment. Recycling costs for such materials usually exceed the value of magnesium recovered. Generation of this type of scrap can be minimized by maintaining clean operating conditions. The difference in scrap 5A and 5B is that the first one is dry and the second is wet. Overall efficiency of recovery depends on the size range, as coarser materials are easier to handle. Class 6B is classified as hazardous material, requiring more costly storage and transportation.

1.3.1 Methods for recovering metal from scrap

Two principally different methods for refining of scrap may be utilised (Waltrip 1990):

1. Flux based metal protection and refining.

2. Flux-free refining using protective gas (presently SF_6) for melt protection and a filter and/or argon-gas purging for non-metallic impurity removal.

Traditionally, melting and refining under flux has mainly been used. Generally, both processes include the following steps (Waltrip 1990):

I Scrap casting storage
II Compacting/ size reduction
III Degreasing/ de-painting
IV Preheating (the scrap) thoroughly to minimum 150°C
V Charging and melting
VI Analysing and alloying
VII Refining
VIII Holding, transferring, casting
IX Sludging, drossing

In case of clean process scrap, step III may be omitted.

1.3.2 Refining using fluxes

1.3.2.1 Principles

When refining with flux, the principle is to use sufficient flux to absorb all the oxide present in the melt, whereafter the salt (with oxides) and metal is allowed to separate. When recycling magnesium by means of salt, Emley (1966, p. 216) reports that two factors are important in coalescence of finely divided metal thinly dispersed in a salt. Firstly, the salt must strip the oxide films from the droplets, and secondly sufficient amounts of fluorides must be present in the salt to produce an appreciable contact angle between salt and droplet. Salts consisting of alkaline chlorides are ineffective, and $MgCl_2$ (or $CaCl_2$) must be present. As the content of $MgCl_2$ increases, so does the metal recovery up to a certain point (Komura et al. 1973). Beyond this concentration, a further increase in $MgCl_2$ leads to lower recoveries. In aluminium, Friesen et al. (1997) have found that as the concentration of $MgCl_2$ increases in the $MgCl_2$-KCl system the ability for aluminium droplets to coalesce decreases. According to Emley (1966) there is a threshold concentration of CaF_2 which must be reached in the salt before appreciable coalescence occurs. This content depends on the alloy content of the dispersed metal and also varies with the $MgCl_2$ content in the salt melt. Friesen et al. (1997) concluded that as the concentration of fluoride additives increased in both NaCl-KCl and $MgCl_2$-KCl salt systems, coalescence of aluminium droplets also increased. Emley (1966, p. 217) also claims that CaF_2 addition appears to be a phenomenon involving contact angle, and when the threshold concentration of CaF_2 has been reached, the salt no longer wets the metal droplets easily and coalescence proceeds quite readily.

The magnesium oxide (film) covering the magnesium alloy drops constitutes a barrier to coalescence. In aluminium-salt systems, fluoride ions facilitate removal of oxide (stripping) of the oxides from the surfaces of the metal drops (Ye and Sahai 1996; Ho and Sahai 1990). Such removal of oxides from the droplets must take place before coalescence of metal droplets can occur. The oxide stripping is not a thermodynamically spontaneous process and the explanations for its happening are not completely clear (Ye and Sahai 1996). When the oxides are removed, it can be shown that coalescence of metal droplets is thermodynamically spontaneous (Ho and Sahai 1990).

The temperature during refining is also important. Waltrip (1990) suggests 704±10°C. Too low temperature results in entraining flux and other impurities in the metal, and a too high temperature may cause excessive oxidation and reduced pot life. The melt is refined using 2-3% flux and stirred for 15 minutes so that melt and flux mix intimately. For heavily contaminated scrap, more salt may be necessary to get a satisfactory refining and avoid “dry” sludge. The latter means that the salt con-

tains so much oxides that it affects the viscosity of the sludge and thereby the ability to separate it from the metal.

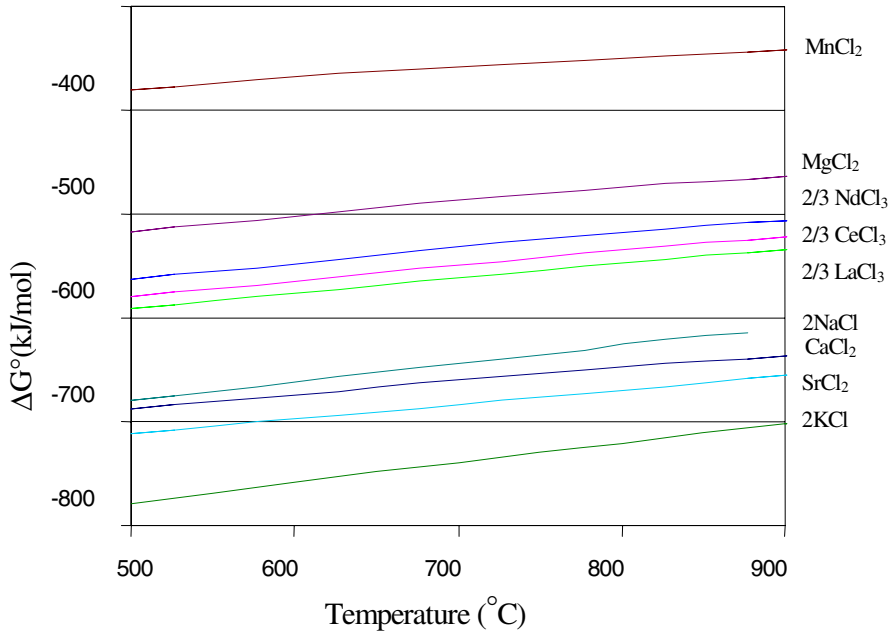

Figure 1.2: ΔG° for some chlorides. Based on thermodynamic data from Kubaschewski and Alcock (1979)

It must be noticed that not all alloys are suitable for flux refining. If any of the alloy elements forms chlorides that are more stable than $MgCl_2$, these will react with the molten salt and eventually be removed from the alloy. Figure 1.2 shows Gibbs energies of formation for some chlorides. It is seen that magnesium alloys with calcium and strontium cannot be flux refined without losing calcium to the salt ($CaCl_2$ and $SrCl_2$ are more stable than $MgCl_2$). Likewise, alloys containing rare earth elements (Ca, La, and Pr) will also be affected by a magnesium chloride containing salt. However, the most important alloying elements, aluminium, zinc and manganese will not be affected.

1.3.2.2 Methods

The standard method for flux refining, which also is used in the industry today, is to melt scrap and flux batchwise and stir in the flux and alloying elements (if necessary). Then, after allowing some time for separation and refining by settling, the metal is transferred into a second furnace from where the metal is cast, either batchwise or continuously. In the second furnace, additional salt-metal separation takes place,

and only small mounts of salt are used. Sludge is removed from the melting furnace between every batch. The use of two furnaces instead of one increases the capacity and improves the quality and consistency of the metal.

Wallevik and Rønhaug (1992) describe a more sophisticated method and a unit for melting and refining of magnesium and magnesium-alloy scrap. It is based on the use of molten salts for melting of the scrap. Molten salts with a composition of 40-60% calcium chloride and 3-7% calcium fluoride are preferred. The rest of the melt may contain sodium chloride and magnesium chloride. This method gives good protection against oxidation. It is not necessary to preheat the metal. This method also gives an ideal refining effect when spraying of molten salts melts the scrap. The oxides that lie on the surface are removed efficiently by the salt and are carried down to the molten salt, thereby separated from the metal. The metal is heated only slightly over the melting point allowing removal of intermetallic particles. For the production of High Purity alloys, manganese salts can be used.

Faure (1995) describes a process for recovery of magnesium from magnesium alloy waste by charging an electric furnace with a flux that is inert with respect to magnesium, and has a melting point lower than 1000°C. An attractive mixture for use as flux is magnesium fluoride (MgF_2)-cryolite (Na_3AlF_6), near the eutectic composition, from 77 to 85% by weight of Na_3AlF_6 and from 15 to 23% of MgF_2. This mixture melts at 920°C and has a density of 2000 kg/m^3 at about 1100°C. The elements which are more dense than magnesium, such as iron, titanium, zirconium, silicon and aluminium, accumulate at the bottom of the furnace in a residual alloy which is continuously removed.

1.4 Fluxless refining

Recycling of magnesium employing salt fluxes has a potential to improve the recovery. But the disadvantages with the salt flux are that it presents a heat transfer barrier, is corrosive to the surrounding equipment, and can combine with impurities in the molten melt or moisture in the atmosphere to form a sludge-like residue in the lower section of the crucible. Furthermore, chlorides may combine with organic residues on the scrap forming highly toxic compounds, creating need for comprehensive off-gas cleaning systems. An alternative is to use fluxless refining processes where salt is not used.

1.4.1 Principles

Fluxless refining includes all refining processes where salt is not used. Settling/floatation and filtration are among these. It has been claimed that gas purging of magne-

sium alloys removes "a lot of" inclusions (Petrovich and Waltrip 1988; Housh and Petrovich 1992; King and Thistletwaite 1994; Jacques et al. 1997). However, quantitative results are to a great extent missing. Although the systems used are different, a reduction by roughly a factor of two is reported in aluminium (Frisvold et al. 1996).

Fluxless refining requires the use of a protective atmosphere. Particles (inclusions) are to be removed from the bulk melt and transferred either to the bath surface, settle to the bottom, or stick to the walls. The purified metal may then be transferred from the bulk melt through a hole into a holding container or removed through a siphon tube. Stirring must be limited since otherwise the inclusions will be re-entrained into the bulk melt. This usually means that the only mechanism for removal is gravity. Since magnesium is such a light metal, one might expect that the heavier inclusions would settle to the bottom. However, as discussed previously (Hillis and Mercer 2000) many particles float up. Probably, the explanation is that they are covered with a gas layer. Perhaps water vapour and dissolved hydrogen play a role in creating the gas layers. The fact that there is a gas layer shows that the particles prefer gas to the magnesium melt, the particles are "wetted" by gas. This fact indicates that particles may be floated up by gas purging (sparging). Essentially only inert gas can be employed since the presence of reactive gases such as chlorine or fluorine-containing gases would give salts. When gas is purged through a melt, the impurities come into contact with the bubbles by various effects mentioned below. If the impurities are wetted by the bubbles but not by the melt, there is a high probability that the impurities remain trapped at the bubble-melt interface and are carried up to the dross or top-slag layer. Various mechanisms for the transfer of inclusions to a bubble are listed below (Engh 1992, p. 247):

I Interception
II Inertia
III Gravitation
IV Diffusion

Figure 1.3 illustrates the mechanisms. The most important mechanisms for removal by gas purging are gravity and interception. If the particle follows the streamline until it collides with the bubble, we have collision due to interception.

It is important for a number of reasons that the purge gas is fed in as small bubbles. The melt/surface contact area is inversely proportional to bubble size. Small bubbles rise slowly up through the melt. The contact area is proportional to the residence time of the bubbles. Finally, small bubbles will not disturb and break up the protective layer of magnesium oxide on the bath surface. It is important that the bubbles are dispersed evenly over the cross-section of the melt. Small bubbles may be formed employing rotors or perforated tubes or porous plugs.

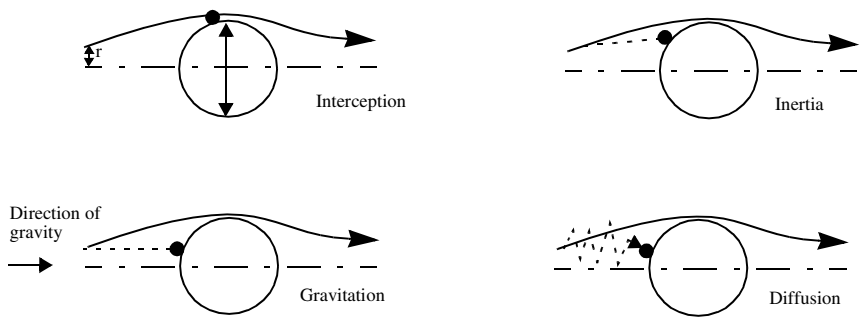

Figure 1.3: Various mechanisms for the transfer of spherical inclusion to a spherical bubble (Engh 1992, p. 247).

Taking gas cost, metal loss due to oxidation of continuously forming surfaces and evaporation of magnesium to bubbles giving MgO dust and increased need for cover gas into account, gas purging of magnesium alloys has its obvious drawbacks. In salt-metal systems, however, gas introduced into the underlying salt phase may be used to effectively distribute salt into the metal phase as a salt layer still surrounds the bubbles even when the bubbles are in the metal phase. This may have a refining effect, probably not due to the gas itself, but rather due to the salt being effectively distributed into the metal. In salt-metal systems one might therefore also consider employing argon and a reactive gas.

1.4.2 Methods

Reding (1976) presents a method for melting magnesium without requiring a salt flux cover on the magnesium surface. The method describes the refining of magnesium containing solid contaminant particles. Magnesium is melted in a melting container. The molten magnesium flows through a hole into a holding container. It is claimed that the solid particles are retained within the melting container. Purified molten magnesium is removed from the holding container. Melting is carried out using a protective gas cover. As pointed out earlier, oxide films and other contaminants usually rise to the surface of the melting container. They are excluded from the holding container by a wall portion. The magnesium melt is removed from the holding

container by a pump. It is claimed that the metal can be used for producing commercial castings without further refining.

Petrovich and Waltrip (1988) discuss a process that utilises the protective atmosphere of an SF_6-CO_2-air protection system with a 0.3% to 0.5% SF_6 concentration and incorporates a filtering system for what is said to be effective reduction of non-metallic inclusions (see Figure 1.4). Utilising a pump equipped with a suitable suction filter, molten metal is transferred into ingot moulds, to a transfer pot, holding pot, or die cast shot sleeve.

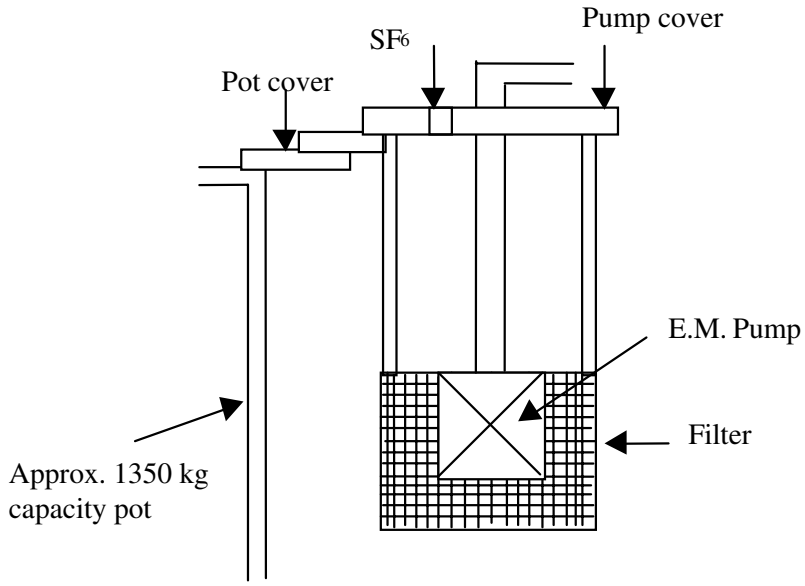

Figure 1.4: A section of pump and suction filter assembly (Petrovich and Waltrip 1988).

Øymo et al. (1992) have described a method for fluxless remelting of magnesium die casting scrap in a two-furnace system. In this method preheated primary magnesium ingots and scrap were melted in a 100 kW resistance heated furnace with a steel crucible containing ~500 kg of metal. Preheating of ingots and scrap were performed in order to keep the melt surface at constant temperature. From the melting furnace, metal flows through a siphon tube into a similar sized casting furnace. From the casting furnace, the metal was metered intermittently through a siphon tube into a 100-kg ingot mould simulating the die-casting process. Figure 1.5 shows the melting and casting system. Melt surfaces were protected with a mixture of 20% CO_2, 0.2% SF_6 and dry air. The metal flow rate was 4 kg/min. The retention time of the melt in the two furnaces was nearly two hours. An average yield of 92.6% was attained independent of scrap content.

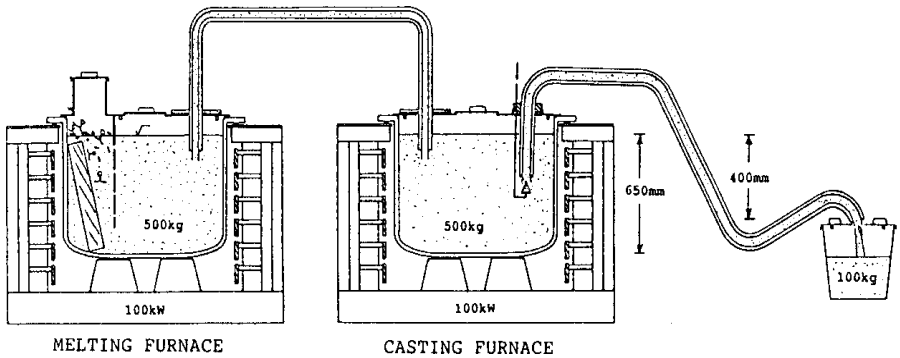

Figure 1.5: Principle drawing of the melting/casting system (Øymo et al. (1992)).

Housh and Petrovich (1992) discuss a fluxless process incorporating inert gas purging and filtering techniques to remove non-metallic inclusions from magnesium scrap. They claim that results from this refining process indicate that the magnesium scrap can be remelted and refined to a quality equal to or better than virgin ingot. The process is claimed to have several advantages over a flux refining system, including the removal of dissolved gases, decreased melt losses, and the elimination of chlorides. It is also claimed that mechanical properties of the recycled magnesium improve after inert gas purging as the number of non-metallic inclusions is decreased. As pointed out earlier, a significant effect of inert gas purging on the removal of hydrogen cannot be expected.

A continuous fluxless process for recycling of process scrap has recently been described (Berkmortel et al. 2000). Also, a major furnace supplier has developed a continuous fluxless solution based on a three chamber furnace equipped with baffles (Schmitz & Apelt 2000).

Chapter 2

Precipitation of nickel-enriched phases and removal of these phases

A number of elements have been tested with respect to the formation of Ni-containing phases or reaction products from high purity magnesium and magnesium-aluminium alloys. The elements zirconium, molybdenum, manganese, vanadium, hafnium, titanium, and tantalum were chosen based on a feasibility study by Simensen and Kolby (1995).

The methods for removal of nickel may be:

1. Partial melting, i.e. the nickel will be enriched in the liquid phase. The solubility of nickel in solid magnesium is low (Nayeb-Hashemi and Clark 1988, pp. 219-225). As magnesium is solidified more and more nickel will be concentrated in liquid phase.

2. Partial solidification - also in this case nickle will be enriched in the liquid phase.

3. Evaporation - same as in 2 above.

4. Precipitation of nickel enriched phases and removal of these phases.

The latter method is the most likely to become an industrial process, because of its similarity with existing methods for removal of iron from magnesium. Therefore, an experimental set-up (in laboratory scale) has been developed in order to study the precipitation and/or filtration of nickel from magnesium (and/or its alloys).

2.1 Theory

Deposition of nickel-enriched phases may occur on a solid (filter) of element X or by reaction with dissolved element X in the magnesium. The former case involves transfer (diffusion) of dissolved nickel to the (filter) walls. In the latter case X dissolves in magnesium, reacts with nickel and precipitates as a solid nickel-enriched phase.

2.1.1 Removal by diffusion

In this case removal is controlled by diffusion of nickel in magnesium and/or by the contact area between X and the melt. Nickel is either deposited as a separate nickel-enriched phase at the interface or it diffuses into the X-phase. In the first case the reaction rate between nickel and X to give a reaction product may be rate limiting. In the second case rates may be low due to low solubility of nickel in solid X and low diffusivities in this phase.

Can diffusion in the molten metal be the controlling step in the present experiments? A rough calculation of the diffusion coefficient of nickel in magnesium may give us an indication. In the experiments, capsules with a diameter of 8.5 mm were used and the shortest of the holding times was in excess of 24 hours.

Assuming that we have an unsteady-state diffusion problem in a semi-infinite cylinder, the key experimental variable is R^2/Dt (Cussler 1997, p. 48). When this variable equals unity, the diffusion process has proceeded significantly. In other words, where R^2 equals Dt, the diffusion has penetrated a distance R in the time t. Using the numbers above (capsule diameter and holding time) we find that the low value $D = 2.1 \times 10^{-10}$ m^2 /s is sufficient for nickel to diffuse from the center of the capsule to the outer diameter. Diffusion coefficient of nickel in magnesium is of the order of 10^{-9} m^2 /s in 400-600°C temperature range (Weast 1980, p. F-66). In conclusion we may say that in our experiments diffusion in molten magnesium is not the controlling mechanism.

2.1.2 Removal by precipitation

The content of X should ideally be so low that it does not harm the mechanical properties of the alloy. Therefore, when nickel is removed from molten magnesium as a nickel-enriched phase, the solubility product of nickel and X should be very low. Precipitation should occur in the following steps:

1. X dissolves in magnesium (reacts with the melt).
2. X reacts with nickel (and possibly also magnesium or other dissolved elements).
3. The nickel containing phase(s) precipitates.

The efficiency of this process depends on the percent nickel in the particles, on the particle size and on the relative density of the particles compared to the melt (and possibly particle shape; flakes settle slower than more compact particles). These considerations are due to the fact that the particles will have to be removed from the molten metal by sedimentation. The largest possible settling velocity is given by Stokes law (strictly valid for spherical particles):

$$v_s = \frac{2a^2 \Delta\rho g}{9\rho\nu} \tag{2.1}$$

where a is the particle radius, $\Delta\rho$ is the density difference between melt and particle, g is the gravitational constant, ρ is the density of the melt and ν is the kinematic viscosity of the melt. Particles may also be removed by, for instance filtration.

To obtain a rough estimate of the smallest intermetallic practical particle size we look at the following case

$\Delta\rho / \rho = 2$

Density of magnesium at 700°C = 1570 kg/m^3 (Weast 1980, p. B-224)
Dynamic viscosity at 700°C, $\mu = \nu\rho = 1.10*10^{-3}$ kg/(ms) (Lide 1990, pp. 6-156)

Settling distance L = 0.5 m and available time t = 3 hours. The kinematic viscosity of magnesium is $\nu = 0.7 \times 10^{-6}$ m^2 /s. Then

$a = 2.73 \times 10^{-6}$ m

Assuming no thermal convection, the calculation gives that to settle, particles should be larger than 5.46 µm in size. Probably, it is more realistic to require that they be greater than 10 µm.

Chapter 3

Thermodynamics

3.1 Partial molar quantities

It is felt that it would be valuable to compile the existing thermodynamic data for solubilities in molten magnesium. To describe the thermodynamic behaviour of individual components in a given phase (melt, solid solution, or intermediate phase), the partial molar quantities are used. The partial derivative of any extensive function Y with respect to number of moles of a component i –keeping constant the number of moles of the other components is called a *partial molar* property

The chemical potential of i (μ_i) is the partial molar Gibbs energy of i:

$$\overline{G}_i = \left(\frac{\partial G}{\partial n_i}\right)_{P,\,\mathrm{T},\,\mathrm{n}_j} = \mu_i \qquad (i \neq j) \tag{3.1}$$

The integral molar Gibbs energy of the solution is:

$$G = \sum_{i=1}^{k} X_i \overline{G}_i = \sum_{i=1}^{k} X_i \mu_i \tag{3.2}$$

i.e., the Gibbs energy of a system is the sum of the chemical potentials of its constituents.

The independent variables for all these derivatives are $P, T, n_1, n_2,\ldots, n_j,\ldots,n_k$ $(j \neq i)$. The partial molar quantities of phases consisting of only one component are obviously identical with the corresponding molar quantities.

Homogeneous systems consist of a single phase. A heterogeneous system consists of several phases.

At equilibrium, the chemical potentials of the components in the various phases must be equal. Thus for a component *i* distributed in two phases α and β at equilibrium:

$$\mu_i^{\alpha} = \mu_i^{\beta} \tag{3.3}$$

3.2 Excess Gibbs energy

The partial molar Gibbs energy of solution of a component *i*, $\Delta\overline{G}_i$, is given by:

$$\Delta\overline{G}_i = \Delta\overline{G}_i^{\text{ideal}} + \Delta\overline{G}_i^{\text{ex}} = RT\ln a_i = RT\ln X_i + RT\ln\gamma_i \tag{3.4}$$

$$\Delta\overline{G}_i^{\text{ex}} = RT\ln\gamma_i \tag{3.5}$$

It may be necessary to split up the excess Gibbs energy into an enthalpy and an entropy term:

$$\Delta\overline{G}_i^{\text{ex}} = \Delta\overline{H}_i - T\Delta\overline{S}_i^{\text{ex}} \tag{3.6}$$

3.2.1 Activity

From equation (3.4) it is seen that the activity $a_i = X_i\gamma_i$, where γ_i is called the activity coefficient of component *i*.

The integral molar Gibbs energy of mixing is given by:

$$\Delta G^{\text{M}} = RT\sum_{i=1}^{k} X_i\ln a_i = RT\sum_{i=1}^{k} X_i\ln(\gamma_i X_i) \tag{3.7}$$

The activity coefficient and activity are concentration and temperature dependent.

Activity is defined as a thermodynamic function that correlates changes in the *chemical potential* with changes in experimentally measurable quantities, such as *concentrations or partial pressures,* through relations formally equivalent to those for ideal systems.

$a_i = 0$ for $X_i = 0$, and $a_i = 1$ for $X_i = 1$

The special solutions for which $a_i = X_i$ are called *ideal solutions.* The deviation from ideality is given by the *activity coefficient* γ_i.

For ideal solution: $\Delta\overline{H}_i = 0$, and $\Delta\overline{S}_i = -R\ln X_i$

For ideal solutions $\gamma_i = 1$ at all concentrations. In real solutions, it is a function of composition, temperature, and pressure and its deviation from the value of 1 will measure the deviation of the behaviour from the ideal model.

3.3 Regular solutions

For non-ideal solutions: $a_i \neq X_i$ and $\Delta\overline{H}_i \neq 0$

Various mathematical formalism are developed to classify non-ideal solutions and the simplest one corresponds to *regular solution behaviour.*

For regular solutions: $\Delta\overline{H}_i \neq 0$ and $\Delta\overline{S}_i = \Delta\overline{S}_i^{\text{ideal}} = -R\ln X_i$

For a regular solution of two components *A* and *B*

$$\Delta G^{\text{ex}} = RT\alpha X_A X_B = \Omega X_A X_B \tag{3.8}$$

where α is an inverse function of temperature.

$$\alpha = \frac{\Omega}{RT} \tag{3.9}$$

For a regular solution,

$$\ln\gamma_B = \alpha_B X_A^2,\ \ln\gamma_A = \alpha_A X_B^2 \tag{3.10}$$

$$\Delta\overline{G}_A^{\text{ex}} = RT_1 \ln\gamma_{A(T_1)} = RT_2 \ln\gamma_{A(T_2)} = \alpha X_B{}^2 \tag{3.11}$$

and hence, for a regular solution,

$$\frac{\ln\gamma_A(T_2)}{\ln\gamma_A(T_1)} = \frac{T_1}{T_2} \tag{3.12}$$

where $\alpha_A = \alpha_B = \dfrac{\Omega}{RT}$

From a statistical model (Gaskel 1995, p. 258)

$$\Delta H^{\text{M}} = \Omega X_A X_B = \Delta G^{\text{ex}} = RT\alpha X_A X_B \tag{3.13}$$

$$\ln\gamma_A = \frac{\Omega}{RT} X_B{}^2 = \alpha X_B{}^2 \tag{3.14}$$

The value of $\dfrac{\Omega}{RT} = \alpha$ is determined by the bond energies between atoms *A-A*, *B-B* and *A-B* and given by:

$$\Omega = zN_A\left[E_{AB} - \frac{1}{2}(E_{AA} - E_{BB})\right] \tag{3.15}$$

Where z is the coordination number and N_A the Avogadro's number.

3.4 Standard states

The Raoultian standard state $X_i \to 1$ is commonly used for theoretical applications. In industrial practice concentrations are often expressed in mass percent. If $\%i$ is the

concentration of the solute in mass percent and M_i its atomic or molecular weight (per mole) in a solution with m components including the solvent, then:

$$X_i = \frac{\%i/M_i}{\sum_{i=1}^{m}(\%i/M_i)}$$ gives the mole fraction of i corresponding to $\%i$.

$$\Delta\overline{G}_i^{ex}(X_i \to 0) = RT\ln\gamma_i^0$$

For 1 weight percent standard state:

$$\Delta\overline{G}_i^{ex}(i = 1\text{wt}\%) = RT\ln\gamma_i^0 + RT\ln X_i(i = 1\text{wt}\%)$$

Using the above equation we get for a binary system

$$\Delta\overline{G}_i^{ex}(i = 1\text{wt}\%) = RT\ln\gamma_i^0 + RT\ln X_i \tag{3.16}$$

using (Equation 3.6)

$$= \Delta\overline{H}_i - T(\Delta\overline{S}_i^{ex} - R\ln X_i) \tag{3.17}$$

or

$$\Delta\overline{G}_i^{ex}(i = 1\text{wt}\%) = \Delta\overline{H}_i - \Delta\overline{S}_i^{ex}T + RT\ln\frac{1\text{wt}\%i/M_i}{1\text{wt}\%i/M_i + 99\text{wt}\%1/M_1} \tag{3.18}$$

Index one in equation (3.18) represents the solvent.

Then from equations (3.5) and (3.6)

$$\ln\gamma_i^0(T_2) = \ln\gamma_i^0(T_1) + \frac{\Delta\overline{H}_i}{R}\left(\frac{1}{T_2} - \frac{1}{T_1}\right) \tag{3.19}$$

Table 3.1 gives partial excess Gibbs energies of dissolution of element i in magnesium values for both the Raoultian standard state and the 1 wt.% standard state. The activity coefficients γ_i^0 calculated at 1000K are also given:

TABLE 3.1: Partial excess Gibbs energies of dissolution of element *i* in magnesium.

Element (i)	$\Delta\bar{G}_i^{ex} = RT\ln\gamma_i^0$ (J/mole)	$\Delta\bar{G}_i^{ex}$ (i = 1 wt%) (J/mole)	Temp. (K)	γ_i^0 at (1000K)	References
Al (l)	-9865.9+3.86T	-9865.9-35.29T	1073	0.486	Kubaschewski et al. (1993, pp. 340-341)
Bi (l)	(-74542)[a]	-74542-56.1T	975	$1.3*10^{-4}$	Hultgren et al. (1973, pp. 428-431)
Ca (l)	(-69178)[a]	-69178-42.4T	1200	$2.4*10^{-4}$	Hultgren et al. (1973, pp. 550-553)
Ca (s)	(-59716-8.54T)[a]	-59716.1-51T	1200	$2.2*10^{-4}$	Hultgren et al. (1973)
Cd (l)	-23313+8.05T	-23313-42.91T	923	0.160	Kubaschew-ski et al. (1993, pp. 340-341)
Cu (l)	-49204+28.89T	-49204-17.34T	1100	0.087	Kubaschew-ski et al. (1993, pp. 340-341)
Cu (s)	-36154+19.27T	-36154-26.96T	1100	0.131	Kubaschew-ski et al. (1993)
Fe (s)	68687+2.7T	68687-42.46T	1000	5355	Siebel (1948)
Ga (l)	-44790+8.35T	-44790-38.65T	923	0.012	Hultgren et al. (1973, pp. 912-917)
In (l)	-29665-6.87T	-29665-58.00T	923	0.012	Kubaschew-ski.et al. (1993, pp. 340-341)
Li (l)	-12636+3.46T	-12636-24.62T	1000	0.332	Kubaschew-ski.et al. (1993, 340-341)
Mn (s)	40140-4.20T	40140-49.2T	1000	75	Elliott (1965)

TABLE 3.1: Partial excess Gibbs energies of dissolution of element *i* in magnesium.

Element (i)	$\Delta\bar{G}_i^{ex} = RT\ln\gamma_i^0$ (J/mole)	$\Delta\bar{G}_i^{ex}$ (i = 1wt%) (J/mole)	Temp. (K)	γ_i^0 at (1000K)	References
Ni (l)	-61000+33.5T	-61000-12.10T	1000	$3.7*10^{-2}$	Feufel (1993), See also Chapter 6, pp. 79-82
Ni (s)	-43500+23.4T	-43500-22.20T	1000	$8.9*10^{-2}$	Feufel (1993)
Pb (l)	-39748-14.42T	-39748-70.45T	973	$1.5*10^{-3}$	Kubaschew-ski et al. (1993, pp. 340-341)
Si (l)	(-53040)[a]	-53040-39.5T	1358	$1.7*10^{-3}$	Gaskell (1995, pp. 442-446)
Si (s)	(-2500-30.0T)[a]	-2500-69.5T	1358	$5.5*10^{-3}$	Gaskell (1995)
Sn (l)	(-79308)[a]	-79308-51.41T	1073	$7.2*10^{-5}$	Kubaschew-ski et al. (1993, pp. 340-341)
Tl (l)	-26569-1.81T	-26569-57.73T	923	0.033	Kubaschew-ski et al. (1993, pp. 340-341)
Zn (l)	-21757+8.54T	-21757-37.93T	923	0.204	Kubaschew-ski et al. (1993, pp. 340-341)
Zr (s)	7350.42+45.41T	7350.42-3.82T	1000	570	Nayeb-Hashemi et al. (1988, pp. 365-370)

a. Regular solution assumed (see equation 3.12).

Partial excess Gibbs energies for solid Ca, Cu, Ni and Si in Table 3.1 are calculated using Gibbs energies for the reaction solid to liquid (Engh 1992, pp. 407-425).

Some of the data given above should be regarded as preliminary results. For instance the solubility of silicon has been obtained only at 1358K. There seems to be a large scatter in the data for zirconium.

3.4.1 Unified Interaction Parameter Formalism

Wagner (1952, p. 51) proposed the standard interaction parameter formalism by a Taylor series expansion for the excess partial molar energy or the logarithm of the activity coefficient. The following expression is obtained for the activity coefficient of component i in a solution of n solutes.

$$\ln\gamma_i = \ln\gamma_i^0 + \sum_{j=2}^{n}\left(\frac{\partial}{\partial X_j}\ln\gamma_i\right)_{X_1\to 1} X_j + \sum_{j=2}^{n}\frac{1}{2}\left(\frac{\partial^2}{\partial X_j^2}\ln\gamma_i\right)_{X_1\to 1} + \sum_{j=2}^{n-1}\sum_{k>j}^{n}\left(\frac{\partial^2}{\partial X_j \partial X_k}\ln\gamma_i\right)_{X_1\to 1} + \ldots \tag{3.20}$$

If the solution is sufficiently dilute then all the second order terms may be neglected and equation (3.20) becomes

$$\ln\gamma_i = \ln\gamma_i^0 + \sum_{j=2}^{n}\varepsilon_i^j X_j \tag{3.21}$$

Where $\ln\gamma_i$ is the activity coefficient of component i in a solution with the mole fractions X_1, X_2, ... X_n of various solutes and $\ln\gamma_i^0$ is the Raoultian activity coefficient if there had been no interaction between the solute components.

ε_i^j are the interaction coefficients defined as:

$$\varepsilon_i^j = \frac{\partial\ln\gamma_i}{\partial X_j} \tag{3.22}$$

Various Gibbs energy interaction parameters are defined when $\text{wt}\%1 \to 100$ and $X_1 \to 1$ in Table 3.2.

TABLE 3.2: Definition of various interaction coefficients (Lupis1983, p. 254).

Order	Free energy interaction coefficients		system
	X (mole fraction)	wt.%	
Zero	$\ln\gamma_i^0$	$\log f_i = 0$	1-i binary
First	ε_i^i ε_i^j	e_i^i e_i^j	1-i binary 1-i-j ternary
Second	ρ_i^i ρ_i^j $\rho_i^{j,k}$	r_i^i r_i^j $r_i^{j,k}$	1-i binary 1-i-j ternary 1-i-j-k quarternary

The logarithm of the activity coefficient of the solute i with respect to mole fraction of the solutes will be given by:

$$\ln\gamma_i = \ln\gamma_i^0 + \sum_{j=2}^{m} \varepsilon_i^j(X_i) + \sum_{j=2}^{m} \rho_i^j X_j^2 + \ldots \tag{3.23}$$

If the composition coordinates are used on the weight percent basis the activity coefficient is given by:

$$\log f_i = \sum_{j=2}^{m} e_i^j(\%j) + \sum_{j=2}^{m} r_i^j(\%j)^2 + \ldots \tag{3.24}$$

Reciprocal relations between interaction parameters are:

$$\varepsilon_i^j = \varepsilon_j^i \tag{3.25}$$

$$e_i^j = \frac{M_j}{M_i} e_j^i + \frac{1}{230}\left(\frac{M_i - M_j}{M_i}\right) \tag{3.26}$$

$$\varepsilon_i^j = 230\frac{M_j}{M_1} e_i^j + \frac{M_1 - M_j}{M_1} \tag{3.27}$$

Bale and Pelton (1990) have given an expression for the first-order interaction parameters (Unified Interaction Parameter Formalism, UIPF) for the whole composition range of solutes. The expression of ln γ_i for each solute is given by:

$$\ln\gamma_i = \ln\gamma_i^0 + \ln\gamma_{\text{solvent}} + \sum_{j=2}^{n} \varepsilon_i^j X_j \tag{3.28}$$

The expression for the activity coefficient of the solvent is given by:

$$\ln\gamma_{\text{solvent}} = -\frac{1}{2}\sum_{j=2}^{n}\sum_{k=2}^{n} \varepsilon_i^j X_j X_k \tag{3.29}$$

Calculated first order interaction coefficients using Wagnerian formalism (equation 3.21) and UIPF (equation 3.28) are given in Table 3.3.

TABLE 3.3: Calculated first order self-interaction coefficients at 1000K in liquid Mg-*i* binary alloys.

Element (i)	$\ln\gamma_i^0$	$\ln\gamma_i$ (X_i=0.1)	ε_i^i UIPF	ε_i^i Wagner	$e_i^i(X_i)$ UIPF	$e_i^i(X_i)$ Wagner	References
Al	-0.722	-0.725	-0.03	-0.03	$3.1*10^{-4}$	$3.1*10^{-4}$	Kubaschew -ski (1993)
Bi	-8.965	-8.319	6.8	6.46	$7.3*10^{-3}$	$7.1*10^{-3}$	Hultgren (1973)
Ca (l)	-8.32	-1.829	68.33	64.91	$1.8*10^{-1}$	$1.7*10^{-1}$	Hultgren (1973)
Ca (s)	-8.21	-1.42	71.51	67.93	$1.9*10^{-1}$	$1.8*10^{-1}$	Hultgren (1973)

TABLE 3.3: Calculated first order self-interaction coefficients at 1000K in liquid Mg-*i* binary alloys.

Element (i)	$\ln\gamma_i^0$	$\ln\gamma_i$ (X_i=0.1)	ε_i^i UIPF	ε_i^i Wagner	$e_i^i(X_i)$ UIPF	$e_i^i(X_i)$ Wagner	References
Cd	-2.07	-1.823	2.0	1.9	$5.3*10^{-3}$	$5.2*10^{-3}$	Kubaschew -ski (1993)
Cu (l)	-2.44	-2.20	2.54	2.41	$6.9*10^{-3}$	$6.7*10^{-3}$	Kubaschew -ski (1993)
Cu (s)	-1.905	-1.873	2.54	2.41	$6.9*10^{-3}$	$6.7*10^{-3}$	Kubaschew -ski (1993)
Ga	-4.38	-3.96	4.47	4.25	$1.0*10^{-2}$	$1.0*10^{-2}$	Hultgren (1973)
In	-4.692	-3.279	14.52	13.79	$1.7*10^{-2}$	$1.6*10^{-2}$	Kubaschew -ski (1993)
Li	-1.104	-1.309	-2.16	-2.05	$-4.4*10^{-2}$	$-4.2*10^{-2}$	Kubaschew -ski (1993)
Ni (l)	-3.31	-2.57	7.79	7.4	$1.7*10^{-2}$	$1.6*10^{-2}$	Chapter 6.3
Ni (s)	-2.43	-1.68	7.89	7.5	$1.7*10^{-2}$	$1.6*10^{-2}$	Chapter 6.3
Pb	-6.648	-4.648	21	19.95	$1.4*10^{-2}$	$1.4*10^{-2}$	Kubaschew -ski (1993)
Si (l)	-6.4	-5.2	12.6	12.0	$4.8*10^{-2}$	$4.6*10^{-2}$	Gaskell (1995)
Si (s)	-5.2	-4.0	12.6	12.0	$4.8*10^{-2}$	$4.6*10^{-2}$	Gaskell (1995)
Sn	-8.89	-6.363	28.53	27.1	$2.9*10^{-2}$	$2.8*10^{-2}$	Kubaschew -ski (1993)
Tl	-3.68	-3.236	4.67	4.44	$6.2*10^{-3}$	$6.1*10^{-3}$	Kubaschew -ski (1993)
Zn	-1.81	-1.468	3.23	3.07	$7.9*10^{-3}$	$7.7*10^{-3}$	Kubaschew -ski (1993)

3.5 Gases in Metals

Gases like hydrogen, oxygen, and nitrogen are soluble in most liquid metals. In solution the gases are present in the atomic state and are therefore not significantly different from other alloying elements (Rosenqvist 1983, p. 79). Solubility of gases in metals also changes when alloying elements are added. For small alloy additions the activity coefficient f_i represents the difference in solubility from that of the pure metal. The i atoms will interact with each other and with the j atoms. This will change the enthalpy of solution for the i atoms and also the structure around the i atoms and thus effect the entropy of the i atoms. The activity coefficient f_i can be expressed in terms of the interaction coefficients

$$\log f_i = \sum_{j=2}^{k} e_i^j [\%j] \tag{3.30}$$

The interaction coefficient e_i^j for each alloy component j is usually determined experimentally.

3.5.1 Hydrogen solubility in magnesium alloys

Hydrogen dissolution into molten metals can be described by the equation.

$$\frac{1}{2}\mathrm{H}_2 = \underline{\mathrm{H}} \tag{3.31}$$

Equilibrium solubility of hydrogen in magnesium is given by the equilibrium constant:

$$K_1 = \frac{[\%\mathrm{H}]f_{\mathrm{H}}}{P_{\mathrm{H}_2}^{1/2}} \tag{3.32}$$

At $P_{\mathrm{H}_2} = 1$ and for pure magnesium ($f_{\mathrm{H}} = 1$), we get

$$-R\ln[\%\mathrm{H}] = \frac{\Delta H^\circ}{T} - \Delta S^\circ \tag{3.33}$$

Plotting the logarithm of the solubility concentrations vs. inverse temperature, a straight line with slope ΔH° should be obtained.

For pure molten magnesium the following thermodynamic data and standard errors have been obtained (Bakke 1992, p. 51)

$$\Delta H^\circ = 21200 \pm 3500 \ \text{J/mol}; \ \Delta S^\circ = -23.1 \pm 2.5 \ \text{J/molK} \tag{3.34}$$

For pure solid magnesium

$$\Delta H^\circ = 20800 \pm 1700 \ \text{J/mol}; \ \Delta S^\circ = -26.6 \pm 1.3 \ \text{J/molK} \tag{3.35}$$

Whereas Øvrelid (1997, p. 139) has reported the following parameters:

For molten magnesium above 650°C:

$$\Delta H^\circ = 23784 \pm 510 \ \text{J/mol}; \ \Delta S^\circ = -20.5 \pm 0.13 \ \text{J/molK} \tag{3.36}$$

For pure solid magnesium below 650°C

$$\Delta H^\circ = 15317 \pm 1327 \ \text{J/mol}; \ \Delta S^\circ = -33.0 \pm 0.76 \ \text{J/molK} \tag{3.37}$$

3.5.2 Solubility of oxygen in magnesium

The solubility of O in liquid magnesium in equilibrium with MgO is given by (Hallstedt 1993)

$$\text{MgO} = \text{Mg(l)} + \underline{\text{O}}, \quad \Delta G^\circ = -448000 + 67.5\text{T}\left(\frac{\text{J}}{\text{molO}}\right). \tag{3.38}$$

Chapter 4

Apparatus and procedure for capsule experiments

4.1 Preparation of samples

The high purity (99.99%) magnesium granules supplied by Alfa Johnson Matthey GmbH were melted in a steel (ST37) crucible. A gas mixture of 0.2% SF_6 (99.8% pure) and CO_2 (Industrial grade) was used to protect the melt from oxidation. To prevent excessive oxidation, the metal pieces were compacted with a steel rod as soon as they softened. One of a precasted magnesium piece was used to add the nickel powder (99.5%). A hole was drilled in the piece and the correct amount of nickel powder was sprinkled into the hole. When the melt had reached a temperature above 750°C, the piece of magnesium containing nickel powder was dropped in the melt, while the melt was being stirred with the steel rod. After at least one hour of holding with stirring every 20 minutes, the melt was cast in a copper mould designed to give six rods (15 x 100 mm) of uniform composition. A nickel yield of nearly 100% was attained in case of Mg-Ni alloys. In the case of magnesium-aluminium alloys, pure aluminium (99.999%) was added to the melt. The geometry and supplier of various materials used in the experiments are given in Table 4.1. Problems were experienced when adding nickel to magnesium-aluminium alloys as the nickel yield was below 50%. This problem was solved by adding first nickel in the pure magnesium melt, keeping the temperature of interest for about one hour and stirring every 15 minutes. Aluminium was finally added, and the alloy was cast after stirring. Cylindrical samples, 8.5 mm x 75 mm, were turned from the cast rods. Chips from machining of one of the six samples mentioned above were analysed by ICP-AES (Inductively Coupled Plasma - Atomic Emission Spectroscopy) technique in order to determine the start concentration of nickel. The samples were numbered with a three-digit code. The first number gives the number of the casting. The second digit is the number of the treatment in the gold furnace and the third number indicates the element X used for the treatment.

The capsules used for heat treatment were made by machining a steel rod (ST 37) in an automatic turning machine and the lids were cut out of a 0.8 mm steel plate (the chemical composition of the steel (ST 37) is given in Appendix A). A magnesium alloy rod along with an element X used to remove nickel was placed inside a capsule. The solid elements X used in these experiments were in the form of foils, wires or pieces (the Certificates of Analysis of the elements X are given in Appendix A). The foils and the threads were rolled around the magnesium alloy rod, while pieces were placed on the top of the magnesium alloy at the open end. The capsules were sealed in a specially designed welding apparatus (Figure 4.1, Øvrelid et al. 1997).

The welding encapsulation procedure is as follows:

1. The capsule with sample is placed in a hollow water-cooled electrode in the welding apparatus. The lid is positioned on the open end of the capsule with a 3 mm thick stainless-steel plate between the lid and the right electrode. The right electrode is adjusted to keep the lid and the stainless steel plate in position.

2. The silica-tube is then slid to the position shown in Figure 4.1, giving a vacuum-tight chamber. The chamber with the capsule is evacuated for at least one hour, to remove traces of water and solvents.

3. Force is applied to the right electrode by tightening a spring. A contact switch is positioned to allow 0.5-1 mm movement before the power is cut off. The welding is started by pushing the power button.

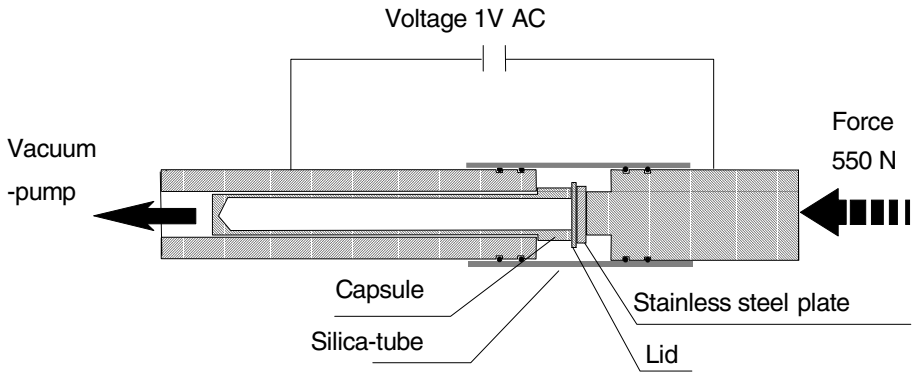

Figure 4.1: Principles of the welding apparatus for encapsulation of the samples (Øvrelid et al. 1997).

When the lid is welded onto the capsule collar, melting of the collar may occur. The melting will appear as cracks in the collar and gives a leaky capsule. To avoid this problem a stainless steel plate is placed outside the lid. Due to the relatively high

electrical resistance of stainless steel, it heats up, allowing the desired welding of lid and collar. The voltage and the spring pressure can be adjusted to avoid melting. If melting occurs the voltage must be reduced or the spring pressure increased.

TABLE 4.1: Materials and gases used in the experiments with their purity and supplier.

Material	Purity (%)	Supplier
Magnesium pieces (Mg1) used in samples starting with 2, 3, and 4.	99.99	Alfa Johnson Matthey GmbH, Zeppelin str 7, D-7615 Karlsruhe, Germany http://www.alfa.com/
Magnesium pieces (Mg2) used in samples starting with 9 and 13.	99.99	ChemPur, Feinchemikalien und Forschungsbedarf GmbH, Postfach 410450, D-76204 Karlsruhe, Germany http://www.chempur.de/
Aluminium	99.999	Vigeland Metal Refinery A/S, N-4700 Vennesla, Norway
Nickel powder Particle size < 10 µm	99.5	Merck KgaA, Frankfurter Str. 250, D-64293 Darmstadt, Germany http://www.merck.de/english/index.htm
Iron Powder Particle size 10 µm	99.5	Merck KgaA, 64271 Darmstadt, Germany http://www.merck.de/english/index.htm
Manganese pieces Irregular size	99.99	Alfa Johnson Matthey
ST 37 steel	99	E. A. Smith Stål og Metall AS, Nedre Ila 66, Postboks 3513, Hospitalsløkkan, N-7419, Trondheim, Norway
Hafnium wire 0.25 mm diameter	99.97	Alfa Johnson Matthey
Titanium foil 0.127 mm thick	99	Alfa Johnson Matthey
Tantalum foil 0.025 mm thick	99.997	Alfa Johnson Matthey

TABLE 4.1: Materials and gases used in the experiments with their purity and supplier.

Material	Purity (%)	Supplier
Zirconium foil 0.025 mm thick	99.99+	Alfa Johnson Matthey
Vanadium wire 0.127 mm diameter	99.8	Alfa Johnson Matthey
Molybdenum foil 0.25 mm thick	99.95	Alfa Johnson Matthey
SF_6	99.8	AGA AS, Gjerdrumsvei 8, 0409 Oslo, Noway http://www.aga.com/no
CO_2	99.9	AGA
Ar	99.9999	AGA

4.1.1 Furnace-temperature profile

A transparent cylindrical furnace (Gold furnace) delivered by Trans Temp Co (see Figure 4.2) was used for the treatment of the samples. The furnace consists of a resistance element with a quartz tube and an outer Pyrex tube covered by a gold layer. The gold layer acts as an insulator as it reflects back the heat from the element. The windings of the heat coil were wound closer at the end to compensate for heat end losses. This was not sufficient to obtain a flat temperature profile. Therefore extra insulation had to be inserted between the two outer tubes, giving a zone of 110 mm, where the temperature was constant within ±1°C. The samples were held in an inner quartz tube with diameter 50 mm in the experiments where four capsules were treated simultaneously. The length of the inner tube was 750 mm. The function of the inner tube was to give a relatively closed system, without too much free convection (chimney effect). This tube also ensured that the heating element was protected from magnesium vapour in case of leakage from the capsule. The capsules were protected against oxidation by flowing argon gas through the furnace. Argon gas entered the lower end and left the upper end of the furnace. The outlet is connected to a double bubble flask setup shown in Figure 5.1. Both ends were closed by silicon-rubber plugs. Through the upper plug, holes were made for the S-type thermocouple, a wire for hanging the sample holder and a tube for argon gas. In the bottom plug, only one

hole for argon gas was necessary. Heat shields were employed to prevent overheating of the silicon plugs.

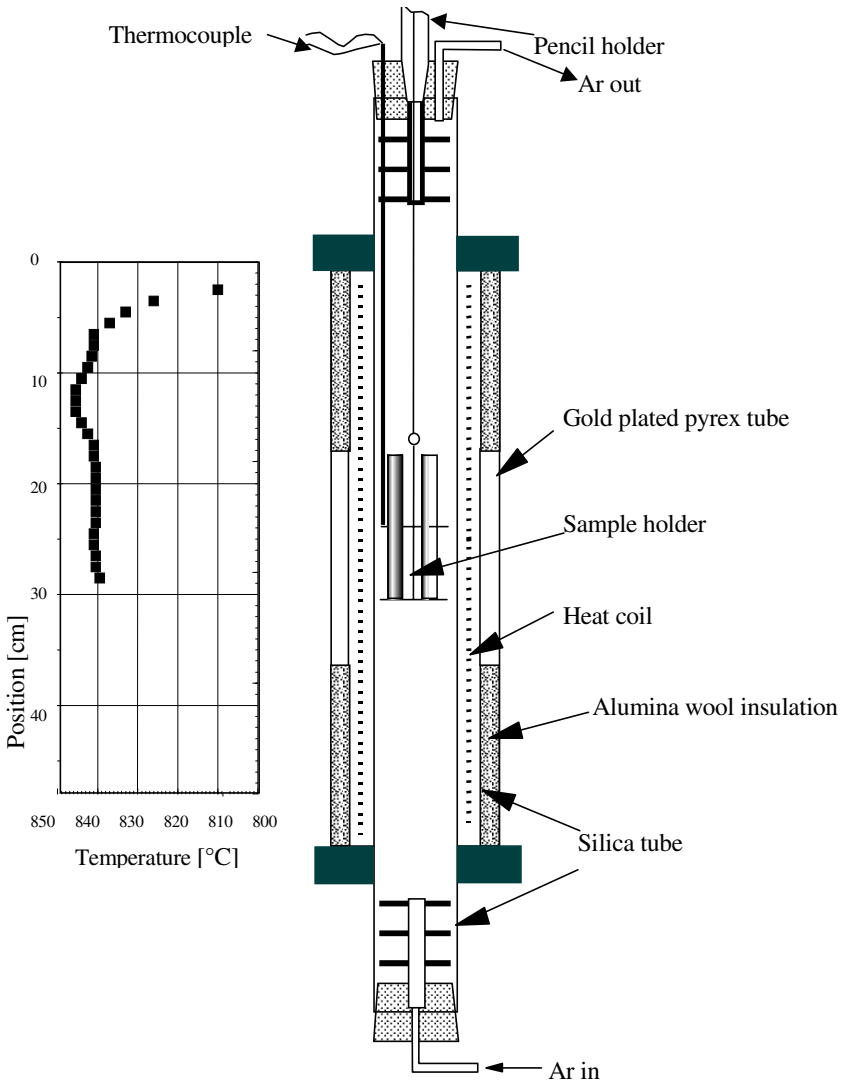

Figure 4.2: Schematic of the furnace used for treatment of the samples. The temperature profile in the furnace is also shown (Øvrelid et al. 1997).

The temperature controller was a Eurotherm Controls 903 and a Eurotherm Thyristor Unit Model 425A. A thermocouple of type K, placed between the inner tube and the heating coil, was employed to control the furnace. A thermocouple of type S was used to measure the temperature near the capsule. The placement of the S element is shown in Figure 4.2. The samples were placed in a sample holder with a capacity of

four capsules. This ensures that the four samples get exactly the same heat treatment. Rapid cooling is performed by dropping the sample holder with capsules into water. A snap release system was used to give reproducible quenching of the samples. A 1.5 mm steel wire connected to the sample holder was kept up by a pencil holder (1.5 mm leads) and released by pressing the top of the pencil holder.

4.1.2 Experimental procedure

The encapsulated samples were placed in the furnace as shown in Figure 4.2 and the furnace was heated to the specified temperature for different times. When the heat treatment was finished, the bottom silica plug was removed, and by pressing the button on the pencil holder, the samples were dropped into water. Samples for SEM-EDS (Scanning Electron Microscope-Energy Dispersive Spectrometer) or Microprobe and ICP-AES analysis were prepared.

4.1.3 Preparation of samples for ICP-AES analysis and SEM

Figure 4.3 shows how the sample was split up for SEM-EDS or Microprobe and ICP-AES analysis.

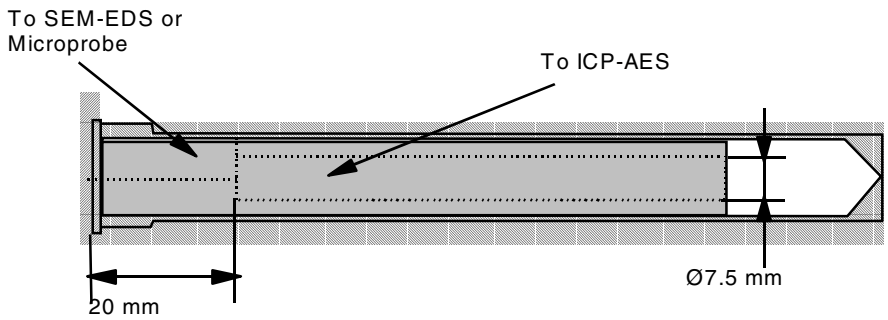

Figure 4.3: The sample split up for SEM-EDS and ICP-AES analysis.

First the sample was cut 20 mm from the bottom, then the 20 mm piece was cut in two along the centre axis. One of these pieces was prepared for SEM-EDS or Microprobe analysis. The reason for selecting the bottom area for SEM-EDS analysis is that if any intermetallic of nickel is formed with X, it is most likely to settle to the bottom. One of these pieces was moulded in plastic resin for SEM analysis. Different emery papers from 80 mesh (196 µm), 180 mesh (75 µm), 320 mesh (46 µm), 500 mesh (30 µm), 1200 mesh (15.2 µm), to 2400 (10 µm) were used to polish the samples. Final polishing was done using diamond paste of 6 µm, 3 µm, and 1 µm. The

samples were carefully washed in water and alcohol and the water was wiped up with tissue paper after each polishing stage so that diamond particles are not transferred from one cloth to another. Finally a carbon coating was applied to make the specimen conductive to carry away the heat that can readily build up in a specimen.

In SEM electrons are accelerated by applying an accelerating voltage (V). The diffraction contrast is better if the primary electrons energy is low. The accelerating voltage is customarily chosen to be 2-3 times greater than the excitation energy of the element analysed (Toya and Kato 1983, pp. 51). Spanning voltage at 15 kV gives best contrast in steel. Optimal spanning voltage for aluminium is 7 kV. We have used 20 kV in analysing the samples because we will be analysing elements (X) with high atomic weights. Other parameters used in SEM were:

Probe current (I) $= 6 \times 10^{-9}$ Amperes
Working distance (WD) = 39 mm

In the (largest) remaining sample a 7.5 mm hole was drilled in the centre axis giving chips for ICP-AES analysis. At least 0.5 gm of chips were needed for ICP-AES analysis.

Chapter 5

Apparatus and procedure for solubility experiments

Various solubility measurements were carried out for the systems, Mg-Al-Ni, Mg-Al-Ni-Fe, and Mg-Al-Mn-Ni in Al_2O_3 and MgO crucibles. The apparatus used and sampling procedure for solubility measurements will be described in this chapter.

5.1 Apparatus

The solubility measurements have been performed in a furnace (Figure 5.2) based on a "Superthal" heating element (a $MoSi_2$ spiral) as the heat source. Superthal is quite resistant towards air and Al_2O_3, which are the immediate surroundings of the heating element. The spiral is built into an insulating cylinder of stiff Al_2O_3 fibres, and covered with an outer cylindrical aluminium jacket and two end plates of brass. The whole system is cooled by circulating water. The $MoSi_2$ spiral is heated by electrical resistance, and is intended for a maximum electrical (AC) input of 66V/40A. The furnace can be used continuously for 3-4 days at temperatures up to 1550°C. In the present work the furnace was used in the temperature range of 650°C - 900°C for a maximum of 10 days without any problem. The controller thermocouple (type S – Pt10Rh) is not located in intimate contact with the spiral, but about 5 mm's into the insulation body. This location gives longer lifetime as the chance for direct contact of thermocouple with $MoSi_2$ or MoO_3 or SiO_2 (or vapours of these) is significantly reduced.

A vertical tube (vacuum-tight dense Al_2O_3) is located inside the $MoSi_2$ spiral. Cylindrical insulation (about 80 mm thick) is added on top and bottom of the original element. Each tube operates for months of regular (not continuous) use at one atmosphere absolute pressure before its replacement is necessary. The tube has a diameter in a range of 50-60 mm, and minimum length of 600 mm. Before assembling, the furnace

tube is cut to optimal length and washed inside and outside. The furnace is first heated to 400°C (in an open tube or under vacuum) to dry the system.

During experiments, vaporised materials condense on the tube, especially in the colder parts. Droplets of magnesium on the Al_2O_3 tube may produce oxidic (corrosive) liquids, because of a slow diffusion of O_2 and/or H_2O (from the atmosphere) through the tube walls (the hottest parts). Occasionally, all loose material should be removed from the tube interior and the radiation shields, especially the upper radiation shields, by brushing, sawing and/or treating with dilute nitric acid. This increases the lifetime of both the tube and the radiation shields, and also the quality of experimental results are typically improved. In a few cases cleaning with diluted acids have been employed, with the lower end of the tube plugged with a rubber stopper. The cleaning with acids was avoided whenever vacuum tests had indicated leaks that could be due to cracks in the tube itself. Thorough flushing with water, and drying should follow any acid cleaning.

The tube is fixed in position by attaching it to the upper (major) brass plate. On the lower end of the tube there is a spring that (during experimental runs) is compressed and then takes some of the tube weight off the upper attachment. The weight removal is just enough to ensure there is no stretching forces in the middle of the tube, which is the hottest and weakest part of the tube during the experiments. This prevents sagging of the alumina tube and reduces the risk for crack growth and tube rupture during experiments.

Each end of the tube is sealed with a water-cooled brass-end piece, involving O-ring seals on the outer surface of the tube. This joining has a number of desirable advantages. It ensures that

- Under optimal conditions the furnace may operate down to 10^{-3} mbar. The joint also endures pressure up to absolute four bar at room temperature.

- The joint endures a heavy and/or skew load, as well as accidental knocks on the end pieces.

- The joint may be dismantled for cleaning, repair or reconstruction.

The total inner furnace volume (inner volume of the tube plus end pieces) is about two litres. Due to the leak tight construction, the furnace can operate with a variety of gases and mixtures.

The gas inlets and outlets are located on the two end pieces of the furnace. A flowsheet for the gas and vacuum system is shown in Figure 5.1. Currently, only a single

gas outlet is in use at the lower end piece. This outlet is normally fully open during experiments, when gas is slowly flowing down through the furnace.

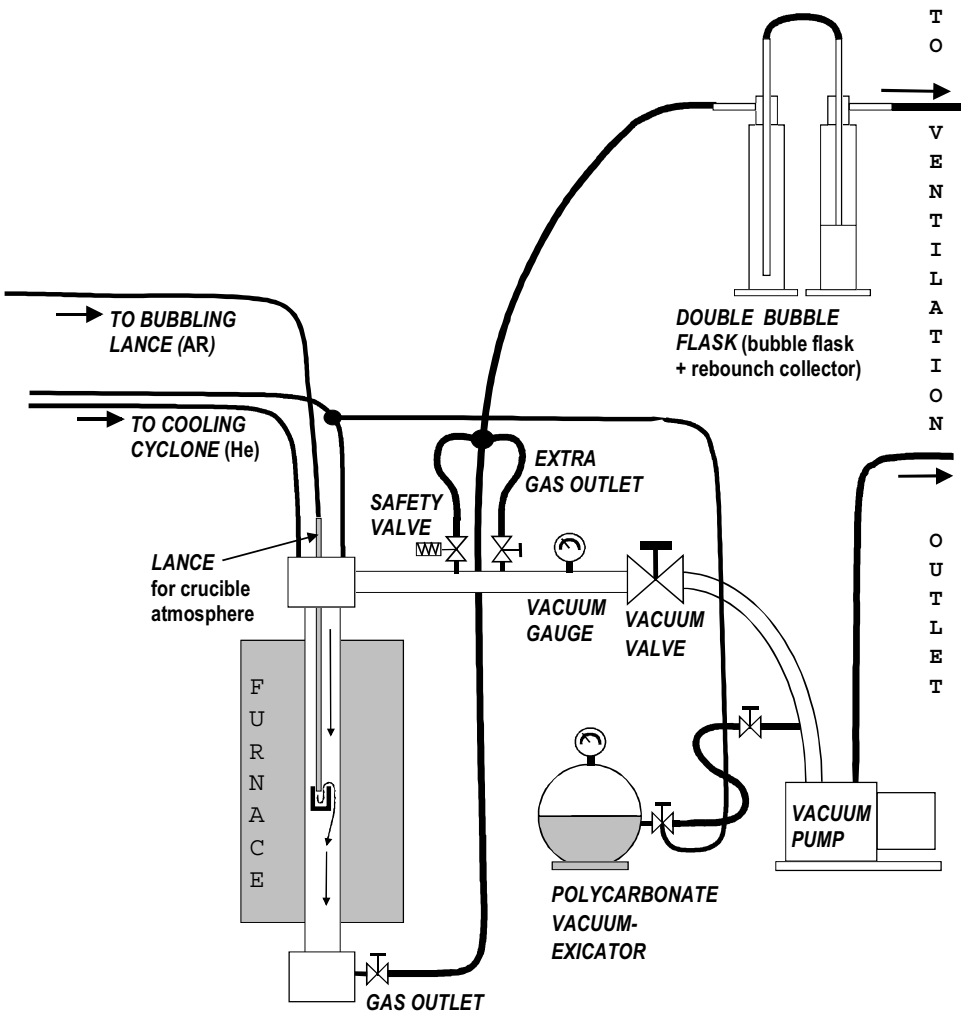

Figure 5.1: A flowsheet for the gas and vacuum system (Fenstad 2000).

The outlet is connected to a double bubble flask set-up that serves the following three purposes:

1. Rapid and approximate adjustment (and monitoring) of the gas (total) flow rate.

2. Fixes furnace pressure conveniently at 3 – 4 mbar above laboratory pressure (more precisely 3 – 4 mbar above the ventilation outlet pressure, which is typically within one mbar of the laboratory pressure).

3. Prevents accidental suction of bubbling liquid (water) into the furnace.

The vacuum connection consists of metal valves and tubes, sealed with O-ring joints. The other outlets are connected to the double bubble flasks with PVC hose (6x12 mm) and are supposed to always operate at 3 to 6 mbar above atmospheric pressure, which is easily fixed by adjusting the height of the water in the outer flask. In this way the possibility of any harm done to the furnace interior due to accidental leaks is minimised.

The valves used for gas flow control are on the gas inlet side. The inlets are connected to gas flasks with copper tubes for most of the length, only a few cm's are covered by reinforced PVC hose (6x12 mm) certified (TÜV geprüft) for maximum internal pressure 15 bar. These tube ways are never operated for pressures above 1.5 bar, and (after proper coupling) the PVC – copper joints have (if later untouched) never been observed to fail even though hose clamps are not used. A "Viton" hose has been found suitable for connecting the copper tubing to the lance, which may then be inserted into the furnace under fully inert conditions. The "Viton" material has been found to be fairly impermeable to air oxidisers (O_2, CO_2, H_2O) yet flexible enough to be suitable for this particular joint. Silicone hoses are avoided for use in these tube ways whenever possible because they are extremely permeable to these air oxidisers.

5.1.1 The furnace interior

A simple diagram of the furnace used for solubility measurements is shown in Figure 5.2. The furnace interior consists of an alumina tube supporter that keeps the crucible in position and is attached to the bottom end plate (or bottom lid) and stretches up into the middle of the furnace. The crucible is placed on an alumina cement platform that rests on the supporter. A ring of Al_2O_3 is placed between the crucible and the platform for adjusting the crucible to its optimal vertical position.

Flat circular radiation shields (discs) of alumina with holes in their centre are treaded onto the alumina supporter at the lower side of the furnace. On the upper side, iron radiation shields are hanging on two thin iron sticks. Two holes have been drilled into each shield to allow simultaneous melt sampling and temperature measurements. These upper shields will serve two functions; they will reduce upward radiation and reduce gas flows. These gas flows will otherwise heat the upper part of the furnace tube excessively, and may also lead excessive deposits of magnesium vapours.

The water cooling system consist of copper tubes (4 mm inner diameter) soldered to brass plates or the cylindrical aluminium jacket. These tubes are connected with PVC hoses (6 mm inner diameter). A continuous flow of water through these tubes keeps the furnace cool from outside.

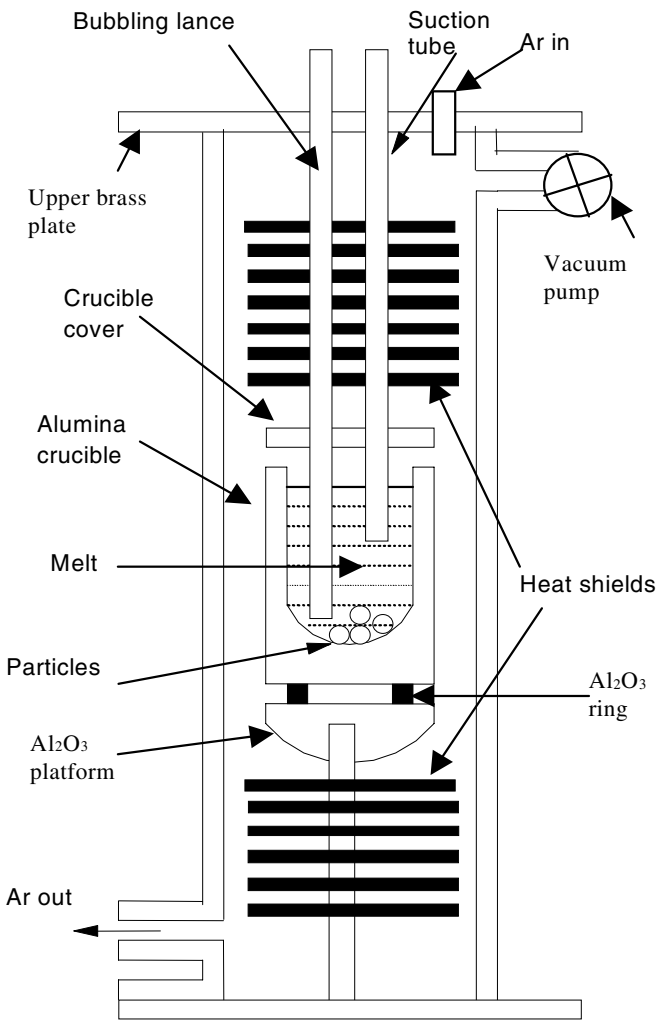

Figure 5.2: A diagram of the furnace used for solubility measurements (not to scale).

Temperature uniformity in the furnace was measured with and without magnesium melt in the crucible. Figure 5.3 shows the temperature profiles in the furnace. The highest temperature is 6 cm above the bottom of the crucible. Due to good thermal conductivity of magnesium the temperature in the melt is uniform compared to temperature without melt.

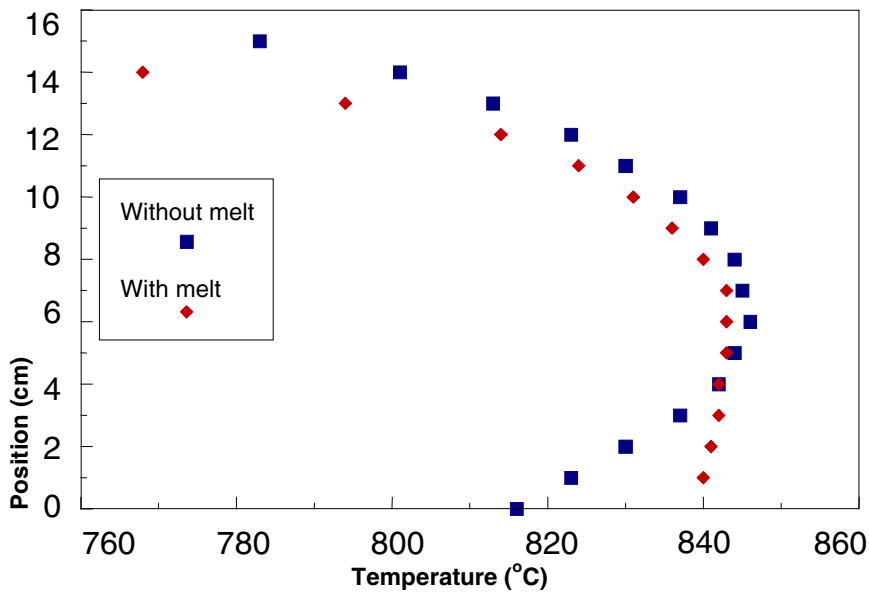

Figure 5.3: Temperature profiles in the furnace with and without melt in the crucible at 850°C. Position zero on y-axis gives the bottom of the crucible.

5.1.2 Materials

Materials used in solubility measurements and their supplier and purity are listed in Table 5.1. The primary materials are magnesium, aluminium, nickel, manganese and iron metal. Argon, helium, Al_2O_3, and MgO are the secondary materials, used for inert/structural purposes. Magnesium in an Al_2O_3 crucible was used to calibrate the thermocouples. The purity of the gases used is given in Table 5.2.

TABLE 5.1: Materials used in the experiments with their purity and supplier.

Materials	Purity (%)	Supplier
Magnesium pieces used in Mg-Al-Ni, and Mg-Al-Ni-Fe systems (Mg1)	99.99	Alfa Johnson Matthey GmbH, Zeppelin str 7, D-7615 Karlsruhe, Germany http://www.alfa.com/

TABLE 5.1: Materials used in the experiments with their purity and supplier.

Materials	Purity (%)	Supplier
Magnesium pieces used in Mg-Al-Ni-Mn system (Mg2)	99.99	ChemPur, Feinchemikalien und Forschungsbedarf GmbH, Postfach 410450, D-76204 Karlsruhe, Germany http://www.chempur.de/
Aluminium	99.999	Vigeland Metal Refinery A/S, N-4700 Vennesla, Norway
Nickel powder Particle size < 10 µm	99.5	Merck KgaA, 64271 Darmstadt, Germany http://www.merck.de/english/index.htm
Iron Powder Particle size 10 µm	99.5	Merck KgaA
Manganese pieces Irregular size	99.99	Alfa Johnson Matthey
AlNi intermetallic Powder Particle size < 44 µm	99.72	Alfa Johnson Matthey
Al_2O_3 tubes, Al_2O_3 crucibles	>99.5	Haldenwanger Berlin, Germany
MgO crucible	Dense	Polyceram Inc. P.O. box 6079, Station “A”, Montreal, Quebec, Canada, H3C 3A7

TABLE 5.2: Gases used in the experiments.

Gases	Purity (%)	Supplier
Argon	99.9999	AGA AS, Gjerdrumsvei 8, N-0409 Oslo, Norway http://www.aga.com/no
Helium	99.998	AGA

Chemical compositions of the materials used in solubility measurements are given in Appendix B.

5.2 Experimental and sampling procedure

Some of the experimental and theoretical techniques described in this Chapter are modifications of procedures from Fenstad (2000).

5.2.1 Crucible Positioning

A crucible containing predetermined alloy components is placed inside the furnace on a platform (see Figure 5.2). The crucible has a cover to minimise the amount of magnesium vapours coming out of the crucible. The crucible cover has two holes, one for measuring temperature or bubbling argon gas and the other for sampling. The crucible must be placed in the furnace carefully. It is important that the two holes on the crucible cover are in alignment with the two holes on the upper brass plate at the top of the furnace. This alignment makes the insertion of lances for bubbling and sampling easier. When metallic pieces of different sizes are charged in the crucible, the finest fraction is put in the bottom and the biggest metal pieces on top, to avoid crucible cracking due to the metal's high thermal expansion.

The horizontal positioning of the crucibles is also important. The crucible position can be adjusted using alumina rings. The height of the rings is adjusted so that the melt surface is at maximum temperature to avoid thermal convection. Thermal convection results in circulation of small particles in the melt and could result in incorrect chemical analysis.

After positioning the crucible, the upper iron shields were inserted before closing the top end of the furnace. It is important that the furnace tube radiation shields are clean. Furnace tube and radiation shields are cleaned (by scraping) to remove loose condensates and splat (from previous experiments) that might fall into the crucible or block the internal spaces. After closing the furnace it was tested for leaks using soap water. The leaks if detected were stopped by screwing the joints tightly. After closing all the valves the vacuum pump was started. The vacuum valves should be opened carefully as some of the constituents like iron and nickel were used in the powder form. Powder may blow up if a vacuum valves is opened quickly. A vacuum of one mbar was created and then the furnace was filled with argon gas grade 6.0 (99.9999) till one bar. This creation of vacuum and filling of argon gas was repeated two or three times to remove as much air as possible from the furnace. The temperature in the furnace rises to ~ 400°C in approximately one hour. During the whole

experimental run, argon gas is flushed downwards through the furnace at about 1-2 ml/s, so that most if not all condensates will settle somewhere below the crucible. With an effective furnace tube volume of about two litres, this means the tube is fully flushed about 2-4 times per hour. This flushing top gas enters the furnace through gas inlets (lance gas) and leaves the furnace through a valve at the bottom brass end-piece.

After completion of the experiments, the furnace was shut down and cooling of the furnace was usually done with full cooling water and no heat. Due to the highly effective insulation the cooling to room temperature takes about 8-10 hours. This insulation is necessary to get this compact and low effect furnace to the highest temperatures in a reasonable time and to avoid thermal cracking in the alumina tube. The top gas was running down the furnace tube at a low rate (0.5-1.5 ml/s) during cooling.

5.2.2 Preparations

In some cases it was found convenient to re-use melts and crucibles. Re-use of melts and crucibles will be mentioned where considered relevant. This chapter describes a number of additional efforts to obtain more controlled experimental conditions.

5.2.2.1 Calibration

In this chapter some calibration details are described and commented. The temperatures were measured by type N-type thermocouples (NiCrSi/NiSi, -250 to +1300°C). The thermocouples were calibrated using 99.99% pure magnesium supplied by Alfa Johnson Mathey. Figure 5.4 shows the calibration curves for the four thermocouples Th1, Th2, Th3, and Th4. These were placed inside the alumina tube, to protect it from the melts and metal vapours. It was found that the thermocouple sheath acts slightly as a cold finger in the present furnace, which have fairly steep thermal gradients. It was also observed that an immersion about 20 mm into liquid metal, about 2 – 5 mm above the bottom, was sufficient to remove the cold finger effect and reproduce established melting points. Thermocouples were calibrated under conditions nearly identical to the experiments.

The actual temperature reading was shown on a (PreciCal PN 6501 display) connected to the thermocouple. This display shows temperatures according to the ITS90 temperature scale. Temperature readings were given in one K steps, and normally recorded this way. But permanent fluctuations between two values often occurred and were recorded as an average value, more precisely a “0.5 K” – value.

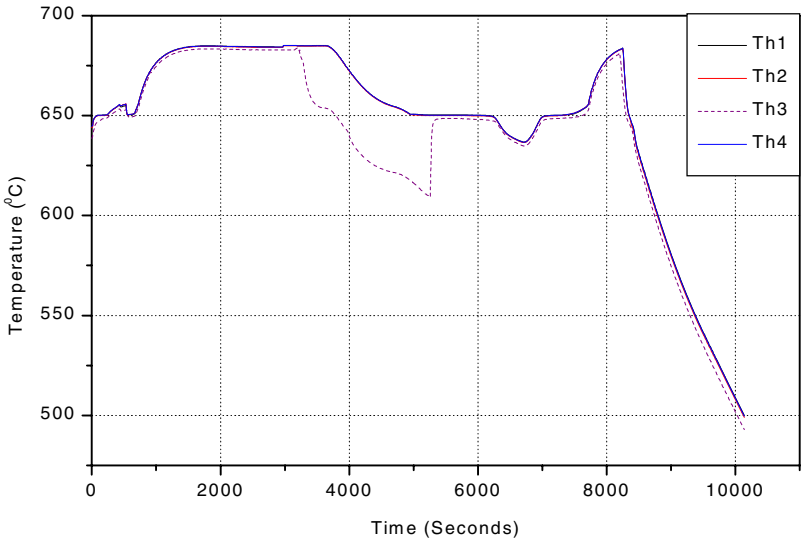

Figure 5.4: Calibration curves of N-type thermocouples used in solubility measurements.

Calibration of the thermocouples was performed by heating the pure magnesium (99.99%) to temperature 685°C and kept at that temperature for 35 minutes. Then the furnace was shut down and allowed to cool. At 650°C the thermocouple showed a halt in the temperature fall. After about 15 minutes the temperature again started to fall indicating that the whole melt was solidified. The furnace was again started and the thermocouple again showed a halt at 650°C until the whole metal melted. The thermocouple was removed from the melt at 685°C and allowed to cool in the air. During calibrations, by a procedure closely identical to the one used to determine liquidus and transformation temperatures, the established freezing point of 99.99% magnesium (650°C) was reproduced by thermocouples Th1, Th2, and Th4. Thus the safest assumption is that the thermocouples Th1, Th2, and Th4 are exact (±1°C) at the melting temperature of magnesium. Thermocouple Th3 gave deviation and therefore was not used in the solubility measurements.

5.2.3 Homogenisation – saturation

For solubility determinations, it is important to know approximately the time needed to equilibrate, saturate or homogenise the metallic solutions, solid or liquid. This may be done directly by performing several experiments of varying duration or by sampling a liquid solution at different time intervals until stable concentrations are

found. Finally, thermal cycling is a common choice, suitable for instance for solubility measurements: If the behaviour of a system is well known and controlled, so that only the desired equilibria are established and measured, then a sufficient criterion for equilibrium/saturation is that the same values are observed upon heating and cooling.

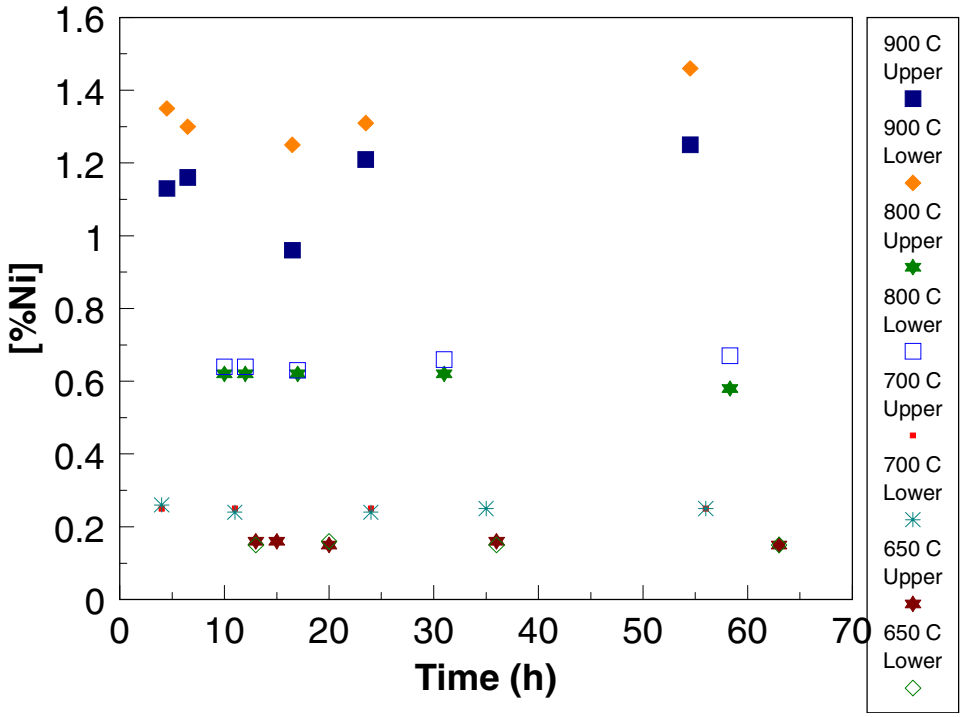

Figure 5.5: Solubility of nickel at various temperatures vs. settling time. The samples drawn out were divided into an upper and lower part.

For achieving equilibrium saturation, one method is to agitate the melt adequately for a long time at each temperature of interest and then allowing sufficient time to settle precipitates and undissolved solute particles. The other method is to heat the premixed components to a temperature 20-25°C above the highest temperature of interest, agitating the melt for a sufficient time so that the melt is saturated with solutes, and subsequently cooling the melt to lower temperatures. At each temperature, samples are taken after giving sufficient time for the settling of precipitated particles. The latter method has two advantages. One is that proper saturation is ensured at lower temperatures if the melt is saturated at the highest temperature. Second, the agitation for a long time is avoided at each temperature. For the molten alloys reported in this thesis, homogenisation was achieved by bubbling argon gas through the melts for 4-5 hours. Settling time was determined for the system Mg-Al-Ni. In the Mg-

10% Al alloy, five samples were taken after about 5, 10, 15, 30, and 50 hours of settling time at each temperature (900°C, 800°C, 700°C and 650°C). A plot of concentration of nickel versus settling time is shown in Figure 5.5. All the samples were divided into two equal parts and analysed by the ICP-AES method. Samples taken at 900°C and 800°C showed a difference in nickel content in the lower and upper part, and the nickel content was higher in the lower part indicating precipitation of nickel. The solubility of nickel was taken to be the average of the solubility in the upper and lower part. For temperatures 800°C and below twenty hours of settling time seems to be sufficient.

5.2.4 Sampling

Sampling of the melts form an essential part of the investigations reported in this thesis. Tube sampling was therefore the chosen method, and pieces would normally be analysed without intermediate treatment. It was also decided that the tube would be filled with inert gas prior to sampling, and that it is given a heat treatment by holding it just above the melt for some time, before it is dipped into the melt. This heat treatment will minimise segregation due to thermal gradients along the tube. Finally, the cooling should take place as quickly as possible and evenly along the sample rod length. Alumina was also found to have the best resistance against the combined thermal and mechanical stress during sampling and cooling.

Various cooling systems were developed during the study. The latest cooling systems gave faster and uniform cooling and were used in studying Mg-Al-Fe-Ni and Mg-Al-Mn-Ni systems. A copper cylinder cooler was used in the study of Mg-Al-Ni system. Fenstad (2000) has given a detailed description of various cooling systems. As these cooling systems were developed and used in this study so it is worth describing them here.

5.2.4.1 Procedure

1) During the experiments, a slow flow of pure argon gas (0.5 - 2 ml/s STP) flushes down the furnace tube, mainly to prevent build-up of condensates in the upper part of the furnace, which would disrupt sampling.

2) The argon flush is increased to about 10 ml/s (STP) immediately before the furnace top is opened for sampling and the sampling tube is put 40 – 50 mm's into the furnace. An "O" ring is located on the tube outside near the lower tip. This ring is now pressed towards the top opening to block this opening, the argon flush is then forced out through the tube itself, which is then filled with argon and air is removed. Sampling takes 4-8 minutes. During sampling the furnace atmosphere will therefore be stagnant, but flushing resumes when the furnace top is closed.

3) After 1-2 minutes a suction device is attached to the tube-top tip. This device is made from a plastic syringe and connected to the tube with a short piece of silicon hose. A spring is built into the syringe top (around the piston rod), to allow one-hand-operation ("squeeze-and-release") of the suction device.

4) The tube is now lowered into the furnace, slowly. This should take at least two minutes regardless of furnace temperature. When the tube tip is just above the melt surface, it should be held there for another minute to attain melt temperature. In this way the tube will be less vulnerable to thermal shocks, and segregation of melt components is avoided due to immediate precipitation. A sample length of about 40-80 mm is advisable depending on the tube material. A typical sample corresponds to (0.4 – 0.6 ml) syringe volume.

5) When using the He-cyclone, the He gas is turned on during the one minute thermal equilibration period. The cooling rate is not very sensitive to the gas flow rate, and a gas velocity of 50 – 200 ml/s is likely to be satisfactory.

6) In the present work, samples were taken 3-5 mm above the bottom of the crucible. The syringe is squeezed about 0.5 ml either before or after the tube has been immersed into the melt. Then the syringe is released to suck the sample, and after full release the tube is immediately and quickly raised into its optimal position within the quencher (copper cylinder or brass cyclone, see Figure 5.6 and Figure 5.7). After 1-2 minutes of cooling the He gas may be switched off for He-cyclone.

7 Two to three minutes after sampling, the tube can be taken out and further cooled in laboratory air without harming the sample. The furnace is closed and the Ar flush is reduced to it's original (lower) level.

Often the tip must be crushed to obtain the sample rod, and even when the rod is easily knocked out or pushed out, the tube tip will still be gradually weakened by the repeated thermal shocks during cooling. Typically one long tube may be used to draw 3 – 5 samples.

8 At each temperature two samples were taken. One sample was taken from the top of the melt and the other sample was taken from the bottom of the melt after 20 hours. The samples taken from the top of the melt were analysed by ICP-AES for chemical composition determination. The samples from the bottom were analysed quantitatively by SEM or Microprobe to identify the precipitated phases.

5.2.4.2 Quenching

It was desired to perform sampling and quenching rapidly and under inert conditions. Inertness was effected by

1) Flushing the tube with Ar gas from the furnace before putting it into the furnace

2) Taking the tube in and out of the furnace with an outward Ar flow of about 10 ml/s

3) Quenching the tube with the sample in the Ar flow (10-20 ml/s), in a copper cylinder (water cooled) located at the top of the furnace. See Figure 5.6.

The copper cylinder is narrow to get a maximum heat transfer between the copper and the sampling tube, both by direct contact and via the Ar flow, which have a fairly high velocity. The three steps discussed above were combined into a sampling procedure that gave rod samples. Samples in the Mg-Al-Ni system were taken by the copper cylinder technique. A disadvantage with the copper cylinder technique is the narrowness of the cylinder. If a melt droplet or anything else adheres to the sampling tube, it may be impossible to take it out of the furnace. Also, the sampling tubes are more likely to break or loose the sample when the cylinder passage is narrow. In a typical experiment, the risk of such events were minimised by using thin sampling tubes.

Later experiments were performed with a vertical column of pressurised air jets, located on top of the furnace, immediately above the copper cylinder, and directed towards the sampling tube (Figure 5.6). The vertical column consisted of 8 jets, diameters 0.7-1 mm. The airflow was 500-1000 ml/s (STP), giving maximum (average) jet velocities up to 250 m/s in the jet holes (Fenstad 2000). Gas velocities at the sampling tube are probably significantly lower, since the jet holes were 30 mm from the tube. This air cooling covers about 70-80 mm of the tube length. Usually, the copper cylinder and the air cooler were used simultaneously, and together they covered about 140 mm of the tube length.

The air jets obviously gave additional (and quicker) cooling, but the upper parts of the sample would be quenched strongly asymmetrically (one-sided). However the samples were rotated to achieve uniform cooling. Because of exposure to air, the air jets gave less inert conditions. Also, the procedure was found cumbersome and typically the tube sometimes slipped out of the air-jet zone and cooling efficiency then dropped dramatically.

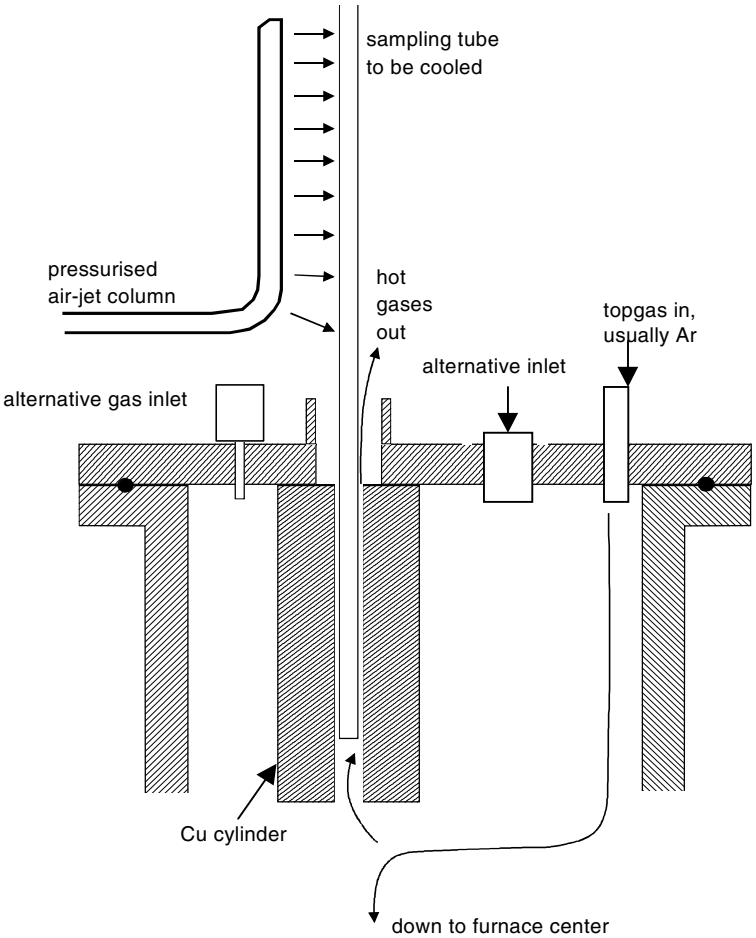

Figure 5.6: Upper part of the furnace with copper cylinder (Fenstad 2000).

Improved quenching – helium cyclone: The natural development was to incorporate the jets into the copper cylinder, to obtain an increased number of jets which would give rapid and uniform cooling. The improved quencher (cyclone) is given in Figure 5.7.

For practical reasons these cyclones were made of brass, which is easier to machine and have nearly the same heat conductivity as copper. The most efficient cooling gas is helium, it has the highest heat conductivity of all inert gases, but other inert gases may be sufficient for less demanding purposes. The gas enters the cylinder in a tangential way, to produce a circular flow (cyclone) in the internal space inside the cylinder. This serves to distribute the pressure evenly across the internal space. The gas

leaves this space through 128 jets ordered in 8 columns à 16 jets, and hits the sampling tube to maximise heat transfer (cooling). The gas then leaves the furnace, just as in the case of the original copper cylinder, effectively preventing outside air from entering the furnace interior.

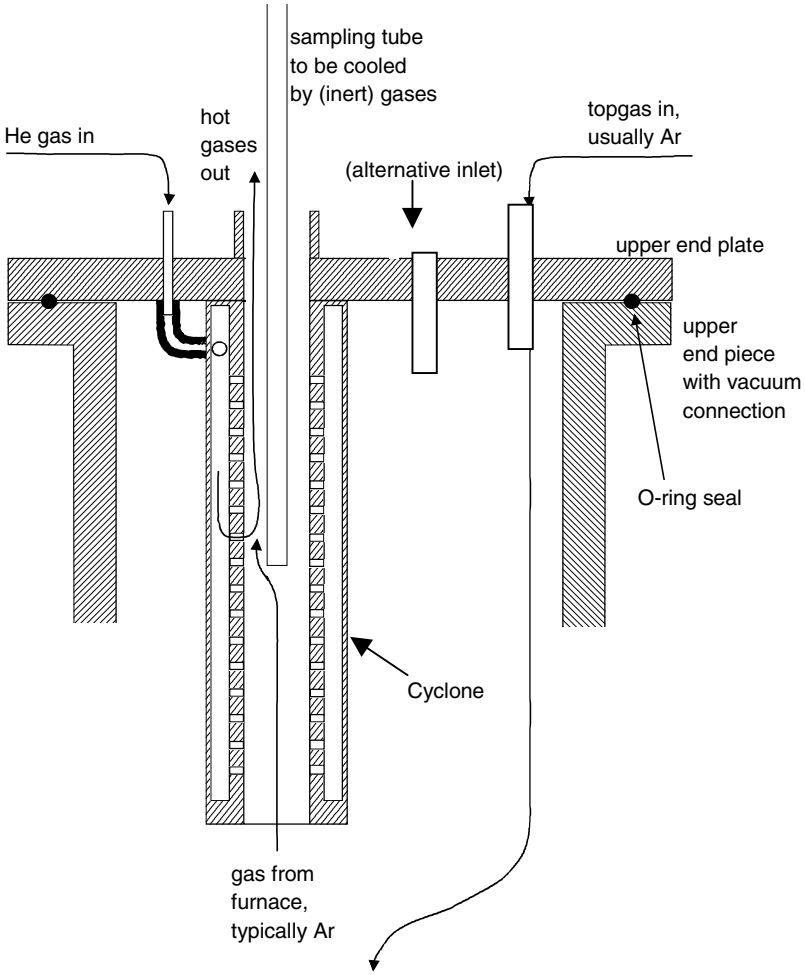

Figure 5.7: Brass cyclone mounted on the upper part of the furnace (Fenstad 2000).

The cyclone is preferable for two reasons:

1) Direct helium jets from the cyclone give higher heat transfer and the efficiency increases with increasing gas velocity. Therefore the cyclone center-hole may be quite wide, and sampling tubes of different sizes may therefore be chosen for differ-

ent purposes. Also, it is easy to take out the sampling tube even if melt droplets adhere to the end of the tube.

2) The jets will automatically press the sampling tube towards the centre of the cylinder hole that is the best possible position within the quencher. Therefore there will be uniform quenching around the tube circumference. There is no chance that the tube may slip out of the jet zone.

A potential problem is cleaning. This quencher may be clogged by particles (unlike the simpler copper cylinder, which also is more easily cleaned). It is important that the helium cooling gas system does not contain particles (chemicals for gas drying etc.) that could clog some of the jet holes, so that uneven quenching could result. If they enter the cyclone, such particles could be difficult to remove or even to detect. Also, the inner holes of the cyclone may gradually be contaminated with dust or condensates from the furnace. Occasional cleaning is most safely done by mechanical removal (scraping the inside) when a vigorous gas flow passes through the cyclone, any dust particles in the "inner" cyclone space are blown out.

The helium gas flow during sampling is typically 100-500 ml/s (STP), and the quenching may take 1-2 minute. For a typical 50-litre/200 atm. gas cylinder the pressure will drop by (for instance) 1-2 atmosphere for each sampling, allowing 100-200 samples quenched from a single cylinder.

5.2.4.3 Cooling rates / quenching tests

An important part of a sampling process is the cooling of the sample, but often the numeric value of the cooling rate need not be precisely known. When it is established that the samples are indeed homogenous and pure, then the sample cooling is (by definition) fast enough.

Ideally (when investigating the cooling rates of tube samples) the temperature should be measured directly on actual magnesium samples, to obtain conditions (closely) identical to the actual sampling. Such measurements are not easy to perform because of possible reactions of molten magnesium with the thermocouple. Fenstad (2000) simulates sample cooling by using a Pt/Pt10Rh thermocouple in a three mm alumina (twin bore) tube as the "sample", and using a 4x7 mm alumina sheath as the "sampling tube". This gives roughly the correct masses, and is expected to represent a fairly realistic simulation. In particular, results obtained in relative tests (comparing rates for different equipment and techniques) should be quite reliable. Future improvements or new quenching techniques may readily be compared with the results presented in this Chapter.

The cooling rates of samples in alumina tubes were measured for a number of different conditions, mainly from 900°C. The most important results are shown in Figure 5.8. The numbers in brackets are the gas velocities in millilitres/second (STP). The temperature of liquid N_2 was –196°C, while all the other quenching media were kept at 20°C. Note that for the liquid quenchers, the time needed to draw the tube with thermocouple ("sample") out of the furnace (about one second) have been excluded in the time count.

It may seem unexpected that the cooling efficiency of liquid N_2 is less than (vigorous) air jet, and well below both water and helium gas. This is explained by the fact that the sample (here: thermocouple) will be surrounded by large bubbles of N_2 gas that prevents direct contact with the liquid.

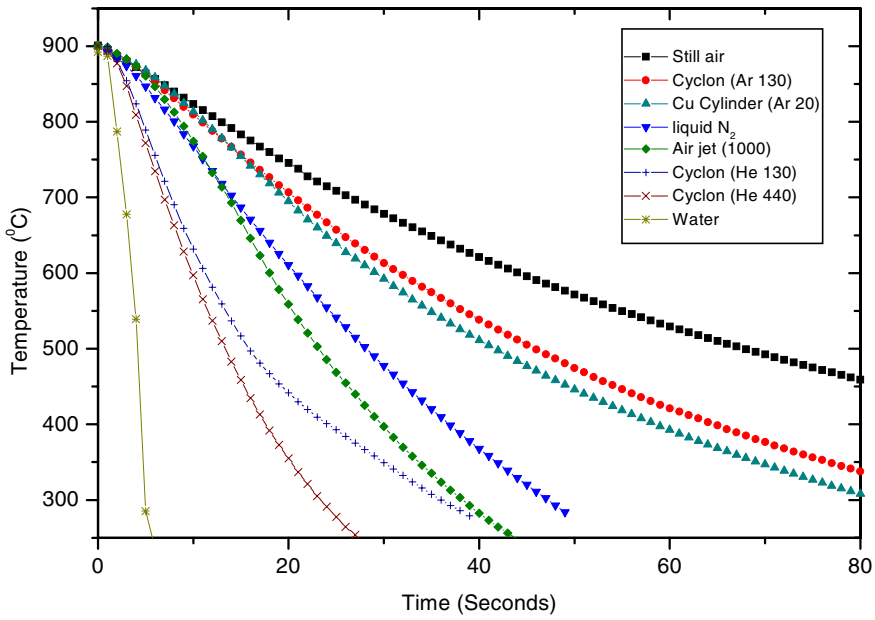

Figure 5.8: A comparison of various cooling media for tube sampler.

The copper cylinder (with argon gas) and the brass cyclone (with argon gas) have roughly equivalent cooling effect when using argon gas. These are about one and a half times as fast as cooling in still air from 900°C to 500°C. Both PAJ (Pressurised Air Jets with 500 – 1000 ml/s) and liquid nitrogen are about three and two and a half

times faster than still air. Cyclone at higher He flow (440 ml/s) has a cooling effect of about five times than still air and approximately twice the liquid nitrogen. Table 5.3 shows the absolute cooling rates of various mediums and their relative cooling effect with respect to still air. The main conclusion is that even moderate helium flows gives more rapid cooling than most alternatives.

TABLE 5.3: Cooling rates of different media and their comparison with still air for tube sampler.

Medium	Cooling rate (°C/s) from 900-500°C	Factor compared to still air
Water	90.9	15.2
Cyclone (He 440)	29.4	5.2
Cyclone (He 130)	25.0	4.4
Air Jet	17.2	3.0
Liquid nitrogen	14.1	2.5
Cu Cylinder (Ar 20)	9.5	1.7
Cyclone (Ar 130)	8.5	1.5
Still air	5.7	1

Chapter 6

Mg-Al-Ni system in Al_2O_3 crucible

In this chapter the solubility of nickel in molten Mg-Al alloys is determined in the temperature range 650-900°C and aluminium range 1-10 wt.%. Equilibrium phases at different temperatures and different compositions are also determined using a scanning electron microscope.

One hundred gram of magnesium was melted in an alumina crucible and 10%, 5% and 1% of aluminium was added in the form of Al-Ni-alloys. Difficulties were faced in adding nickel to the Mg-Al alloys so an Al-Ni alloy of 20 wt.% nickel and 80 wt.% aluminium was prepared from pure aluminium and nickel powder. The content of Al-Ni alloy was selected in such a way that about 5% of nickel was added to the Mg-10%Al melt so that the melt was saturated with nickel. In some cases extra nickel powder was also added so that there is an excess of nickel in the melt. The purity and the supplier of the materials used in the solubility experiments is given in Appendix B. The alloy was heated to 900°C and argon gas was bubbled through the melt using an Al_2O_3 lance for approximately four hours to ensure full saturation by thorough mixing of the melt. After stopping bubbling, one sample from the top and one sample from the bottom of the melt was taken after 20 hours of settling time at 900°C. The 20 hours of settling time was found to be sufficient for settling of precipitated or undissolved particles (Chapter 5, Figure 5.5). The temperature was subsequently reduced to 800°C, 700°C and 650°C and samples were taken from the top and the bottom of the melt after 20 hours of settling time at each temperature. The same procedure was employed for Mg-5%Al and Mg-1%Al alloys.

The samples from the top of the melt were analysed by ICP-AES to determine the chemical composition of the melt. Solubilities of nickel in magnesium alloys at different temperatures with different aluminium contents are given in Table 6.1. The samples from the bottom of the melt were analysed quantitatively with SEM-EDS

(Scanning Electron Microscope Energy Dispersive Spectrometer) to determine the composition of the precipitated phases.

TABLE 6.1: Composition of the samples analysed by ICP-AES. The melts were given a settling time of about 20 hours. The remainder is magnesium.

Sample no.	Temperature (^{o}C)	[wt.% Al]	[wt.% Ni]
515A	900	9.35	1.36
525A	800	8.90	0.63
535A	700	8.80	0.15
545A	653	8.80	0.15
513B	896	3.60	1.50
523B	800	3.30	0.62
533B	686	3.20	0.26
543B	651	3.00	0.17
513C	896	1.10	2.70
523C	800	0.63	1.70
533C	686	0.33	1.20
543C	651	0.26	0.98

An experiment was also conducted in MgO crucible. In this experiment AlNi intermetallic (stoichiometric) particles were added to pure magnesium. The sampling procedure is same as described earlier. The results obtained are given in Table 6.2.

TABLE 6.2: Composition of the samples (using MgO crucible) analysed by ICP-AES. The melt was given a settling time of about 20 hours. The remainder is Mg.

Sample no.	Temperature (^{o}C)	[wt.% Al]	[wt.% Ni]
71B	853	1.14	2.65
72B	804	0.88	1.99
73B	746	0.59	1.49
74B	712	0.52	1.26
75B	670	0.47	1.11

6.1 Results and discussion

Analysis of specimens taken from the melt after 20 hours of settling time is given in Table 6.1 and Table 6.2. It is seen that the solubility of nickel decreases with increasing aluminium content and decreasing temperature. Figure 6.1 shows the natural logarithm of the product of the solubility of aluminium and nickel in Mg-Al alloys as a function of inverse temperature using data from Table 6.1 and Table 6.2.

Lines fitted to a model of the type

$$\ln[\%\mathrm{Al}][\%\mathrm{Ni}] = A + B/T \tag{6.1}$$

are also indicated.

Here T is the absolute temperature and A and B are parameters. A and B for the three different concentration ranges studied are listed in Table 6.3 together with the R^2 indicating the fit to the model.

The straight lines (6.1) were fitted to the data using a computer program (Origin Version 5).

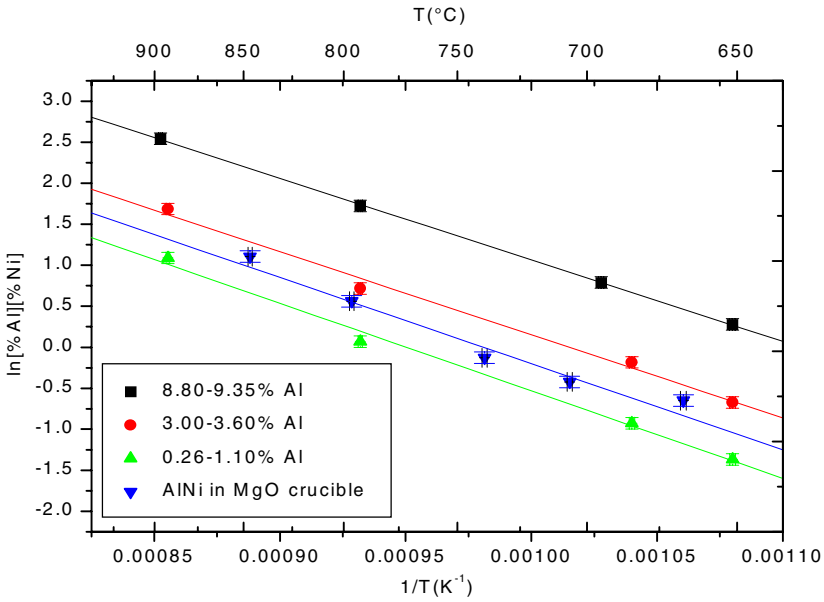

Figure 6.1: Relation between the natural logarithm of the solubility product of Al and Ni and the inverse of the temperature for each of the three series. The data for AlNi (stoichiometric) in MgO crucible is also given. Note that the inside ticks on the top axis correspond to the outside ticks and labels on the bottom axis and vice versa.

TABLE 6.3: The parameters *A* and *B* with errors for different Al contents in Mg alloys.

[%Al]	*A*	*B*	*R*-squared
0.26-1.10	10.1±0.6	-10500±600	0.994
3.00-3.60	10.3±0.6	-10000±600	0.992
8.80-9.35	11.0±0.1	-9900±100	1.000
AlNi in MgO	10.3±1.1	-10500±1100	0.968

Figure 6.2 shows isotherms for the Mg-Al-Ni system at 650, 700, 800 and 900°C, respectively. The isotherms in Figure 6.2 are drawn using equation (6.1) and one more point from the binary Mg-Ni phase diagram (Nayeb-Hashemi and Clark 1988,

pp. 219-225). Equation (6.1) is used to find the nickel solubility at temperatures 650, 700, 800, and 900°C. The ternary phase diagram is plotted using the Sigma Plot program (Appendix E) (SigmaPlot 1997). It is assumed that the nickel content obeys an approximate relation [%Ni] = a exp(b/T + c) where a, b and c are determined from a least squares fit. It is clear from Figure 6.2 that the solubility of nickel increases with increasing temperature and the solubility decreases with increasing aluminium content.

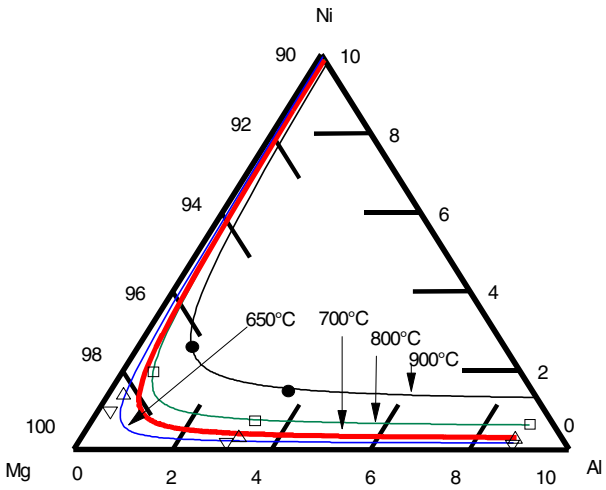

Figure 6.2: Isotherms in the Mg-Al-Ni system in the Mg-rich corner.

6.2 SEM-EDS analysis

After a sufficient settling time (20 hours), samples from the bottom of the crucible were taken at each temperature to identify the precipitated phases. The following phases were identified in equilibrium with the melt.

6.2.1 AlNi phase

These particles were found in different shapes and sizes. Figure 6.3 shows the AlNi phase in round form and having sizes up to 100 µm. Figure 6.4 shows the AlNi phase in different forms and having sizes 30-40 µm. All these different shaped particles have nearly 45 at.% Ni. These particles were present in a melt with composition Mg-9.35% Al-1.36% Ni sampled at 900°C.

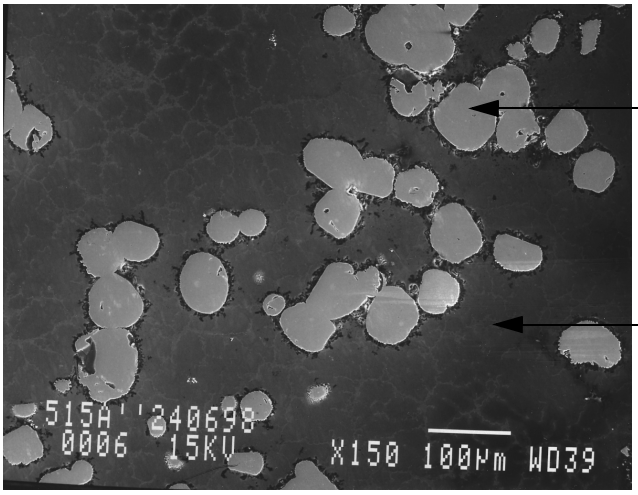

Figure 6.3: AlNi particles of round shape identified in the sample taken at 900°C and 9.35% Al content (X150).

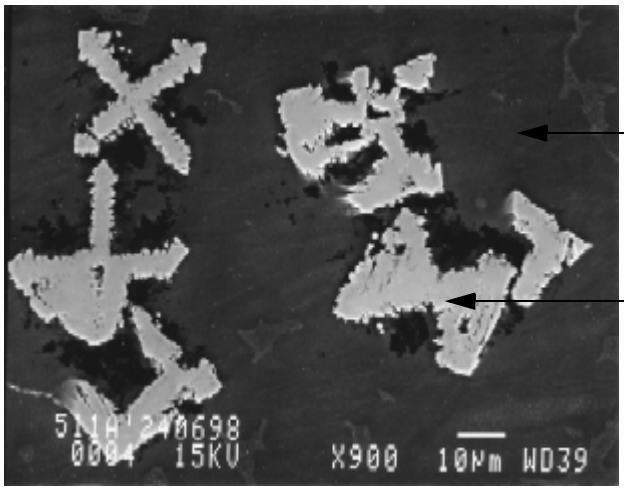

Figure 6.4: AlNi particles with different shapes identified in the sample taken at 900°C and 9.35% Al content(X900).

6.2.2 Al_3Ni_2 Phase

These particles are also found in different shapes and sizes. Figure 6.5 and Figure 6.6 show the different shapes of Al_3Ni_2 phase containing about 37 at.% Ni. These parti-

cles were present in a melt with composition Mg-9.35% Al-1.36% Ni sampled at 900°C.

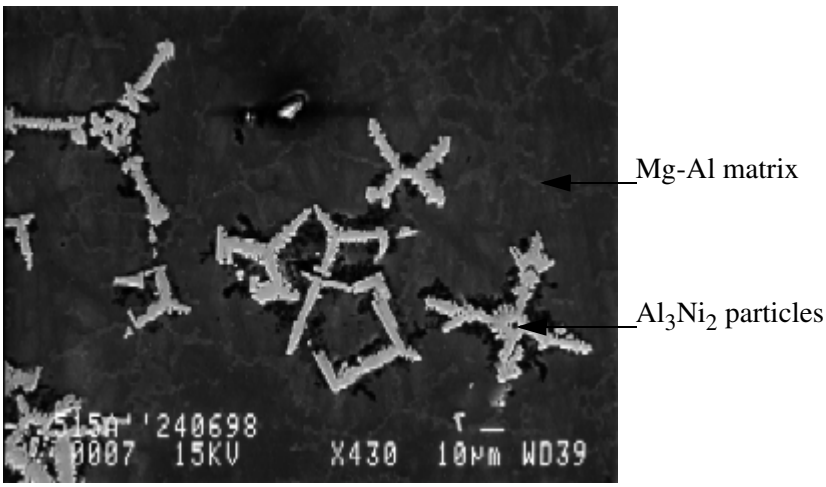

Figure 6.5: Al_3Ni_2 particles identified in the sample taken at 900°C and 9.35% Al content(X430).

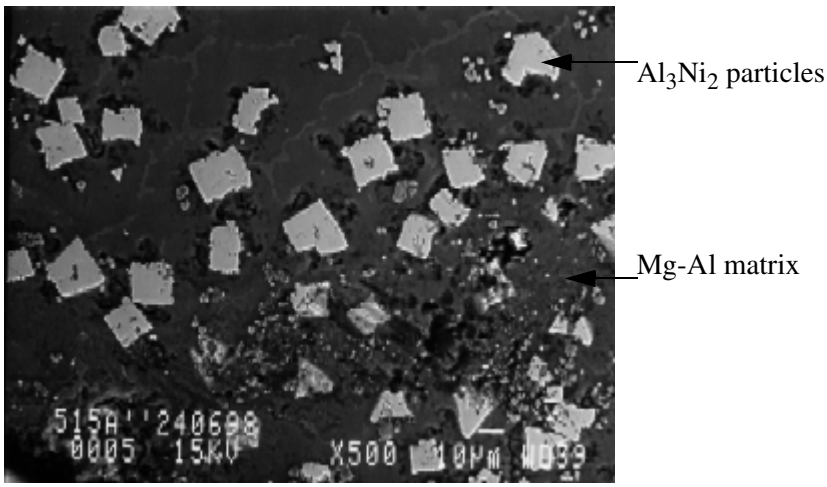

Figure 6.6: Al_3Ni_2 particles identified in the sample taken at 900°C and 9.35% Al content(X500).

Various phases identified in the melts of different composition and at different temperatures are given in Table 6.4. The compositions of the phases in the melts are compared with the compositions of the phases in the Al-Ni phase diagram (Figure 6.7) in Table 6.5.

TABLE 6.4: Phases containing Al and Ni at various temperatures and compositions identified using SEM.

Sample no.	Temperature (^oC)	[wt.% Al]	[wt.% Ni]	Phases
515A	900	9.35	1.36	Al_3Ni_2, AlNi
525A	800	8.90	0.63	Al_3Ni_2, AlNi
535A	700	8.80	0.15	Al_3Ni_2
545A	653	8.80	0.15	Al_3Ni_2
513B	896	3.60	1.50	AlNi
523B	800	3.30	0.62	AlNi
533B	686	3.20	0.26	Al_3Ni_2, AlNi
543B	651	3.00	0.17	AlNi
513C	896	1.10	2.70	AlNi
523C	800	0.63	1.70	AlNi
533C	686	0.33	1.20	AlNi
543C	651	0.26	0.98	AlNi

TABLE 6.5: A comparison of the compositions of the observed solid phases with the composition of phases in Figure 6.7.

Phase	Measured (at% Ni) content	at% Ni given by AlNi phase diagram (Figure 6.7)
AlNi	44-45	~42-62
Al_3Ni_2	~37	~37-42

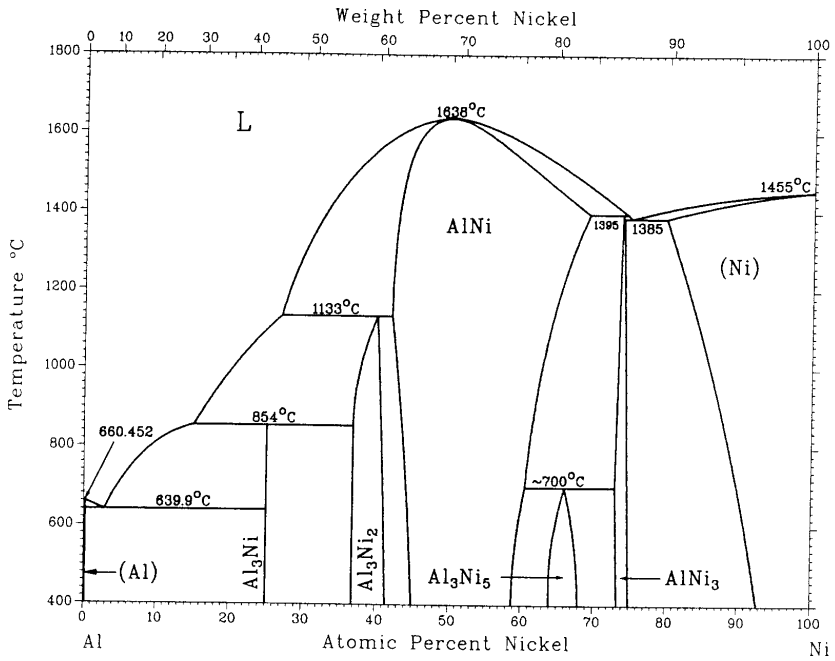

Figure 6.7: Al-Ni phase diagram (Massalski 1990, p. 183).

6.3 Thermodynamics

The nickel activity data in the Mg-Ni system has been taken from Feufel (1993, p. 133). At 1023 K the activity values are given in Table 6.6.

TABLE 6.6: Activity values of nickel in Mg-Ni system at 1023K (Feufel 1993).

X(Ni)	a(Ni)	γ_{Ni}
0.1	0.008	0.08
0.2	0.024	0.12
0.3	0.062	0.21
0.4	0.128	0.32
0.5	0.23	0.46

TABLE 6.6: Activity values of nickel in Mg-Ni system at 1023K (Feufel 1993).

X(Ni)	a(Ni)	γ_{Ni}
0.6	0.39	0.65
0.7	0.581	0.83
0.8	0.76	0.95
0.9	0.899	0.99
1	1	1

Wagnerian formalism for the activity coefficient is given by:

$$\ln\gamma_i = \ln\gamma_i^0 + \sum_{j=2}^{n} \varepsilon_i^j x_j + \sum_{j=2}^{n}\sum_{k=2}^{n} \rho_i^{j,k} x_j x_k \tag{6.2}$$

where $\ln\gamma_i^0$ is the Raoultian activity coefficient if there had been no interaction between the solute components. For a binary Mg-Ni system, ε_i^j will be ε_{Ni}^{Ni} which is called self interaction coefficient. The data for $\ln\gamma_{Ni}$ from Table 6.6 is plotted versus mole fraction of nickel in Figure 6.8. Fitting equation (6.2) to the data given in Table 6.6 and extrapolating will give the value $\ln\gamma_{Ni}^0$ for $X_{Ni} = 0$, and self interaction coefficient ε_{Ni}^{Ni}. At 1023K the values for $\ln\gamma_{Ni}^0$ and ε_{Ni}^{Ni} are -3.24 and 6.67, respectively. If the Mg-Ni system is assumed to behave as a regular solution, the value $\ln\gamma_i^0$ at 1000K may be calculated using (Gaskell 1995, p. 251):

$$\frac{\ln\gamma_i^0(T_1)}{\ln\gamma_i^0(T_2)} = \frac{T_2}{T_1} \tag{6.3}$$

$\ln\gamma_{Ni}^0$ at 1000K is found to be -3.31.

We also have the following relation:

$$RT\ln\gamma_i = \Delta\overline{G}_i^{xs} \tag{6.4}$$

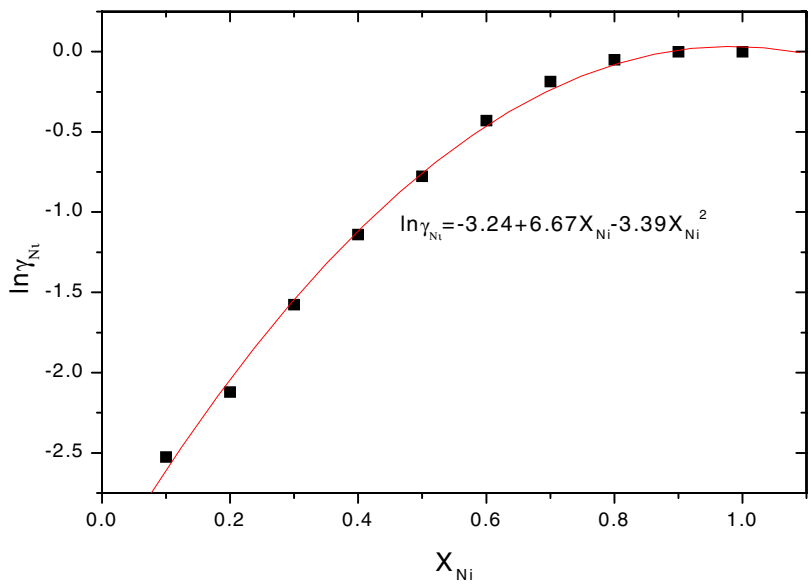

Figure 6.8: Plot of log of activity coefficient (Table 6.6, data from Feufel 1993) of nickel in molten magnesium versus mole fraction nickel.

At 1000K, we get using equation (6.3) $\Delta\overline{G}^{\circ}_{\mathrm{Ni}}(X_{\mathrm{Ni}})$ = -27500 Jmol^{-1}

and $\Delta\overline{H}^{\circ}_{\mathrm{Ni}}$ = -61000 ± 3000 Jmol^{-1} in molten magnesium (Feufel 1993, p. 32).

Then for the dissolution of nickel in molten magnesium assuming that Mg-Ni behaves regularly:

$$\Delta\overline{G}^{\circ}_{\mathrm{Ni}}(X_{\mathrm{Ni}}) = -61000 + 33.5T \tag{6.5}$$

$$\Delta\overline{G}^{\circ}_{\mathrm{Ni}}(X_{\mathrm{Ni}}) = -41936 \text{ at 1000K (Kubachewski et al. 1993, p. 340)} \tag{6.6}$$

$\Delta\overline{G}^{\circ}_{\mathrm{Ni}}$ given by equation (6.6) is more negative from equation (6.5). The reason may be that the value given by Kubachewski et al. (1993) is extrapolated from only one value.

If the reference state is 1 wt.%

$$\Delta\overline{G}^{\circ}_{\mathrm{Ni}}(\%\mathrm{Ni}) = \Delta\overline{G}^{\circ}_{\mathrm{Ni}}(X_{\mathrm{Ni}}) + RT\ln\left(\frac{M_{\mathrm{Mg}}}{100M_{\mathrm{Ni}}}\right) \tag{6.7}$$

or

$$\Delta\overline{G}^{\circ}_{\mathrm{Ni}}(\%\mathrm{Ni}) = -61000 - 12.10T \tag{6.8}$$

The Gibbs energy for the reaction Ni(s) = Ni(l) is 17500 - 10.1T (Engh 1992, p. 419, FACT-Win 3.05).

For Ni(s) = <u>Ni</u> (Mg)

$$\Delta\overline{G}^{\circ}_{\mathrm{Ni}}(X_{\mathrm{Ni}}) = -43500 + 23.40T \tag{6.9}$$

and

$$\Delta\overline{G}^{\circ}_{\mathrm{Ni}}(\%\mathrm{Ni}) = -43500 - 22.20T \tag{6.10}$$

At $X_{\mathrm{Ni}} = 0.1$, the calculated $\Delta\overline{G}^{\circ}_{\mathrm{Ni}}$ is:

for Ni(l) = <u>Ni</u> (Mg) $\Delta\overline{G}^{\circ}_{\mathrm{Ni}}(X_{\mathrm{Ni}}) = -48700 + 27.30T$

and for Ni(s) = <u>Ni</u> (Mg) $\Delta\overline{G}^{\circ}_{\mathrm{Ni}}(X_{\mathrm{Ni}}) = -31200 + 17.20T$

Aluminium can be used to precipitate nickel as follows,

$$\underline{\mathrm{Al}} + \underline{\mathrm{Ni}} = \mathrm{AlNi} \tag{6.11}$$

and AlNi being heavier than magnesium will settle due to gravity. For instance at 700°C and 8.8% aluminium the nickel content in the melt comes down to 0.15%.

The Gibbs energy for the formation of AlNi in magnesium from dissolved aluminium (<u>Al</u>) and dissolved (<u>Ni</u>) is calculated in Table 6.7.

TABLE 6.7: Standard Gibbs energy for the reactions.

Reaction	$\Delta G°(\%)$
Ni(s) = <u>Ni</u>	-43500 - 22.2T from equation (6.10)
Al(l) = <u>Al</u>	-9866 - 35.3T (Kubachewski et al. 1993)
AlNi(s) = Al(l) + Ni(s)	133377 - 20.4T (Wang and Engell 1992)

Using data in Table 6.7, for $\underline{\text{Al}} + \underline{\text{Ni}} = \text{AlNi}$

$$\Delta G°(\%) = -80000 + 77.9T \tag{6.12}$$

6.3.1 Experimental results

We will assume that the phase in equilibrium with the melt in our composition and temperature range is AlNi (See Table 6.4).

$$\text{AlNi} = \underline{\text{Al}} + \underline{\text{Ni}} \tag{6.13}$$

$$-RT\ln\text{K}_{\text{AlNi}} = -RT\ln\frac{a_{\text{Al}} \times a_{\text{Ni}}}{a_{\text{AlNi}}} = \Delta G° = \Delta H° - T\Delta S° \tag{6.14}$$

Where K_{AlNi} is the equilibrium constant and a_{Al} and a_{Ni} are the activities of aluminium and nickel in magnesium.

It is assumed that $a_{\text{AlNi}} = 1$

Activity of a component i in a solution is given by:

$$a_i = f_i[\%i] \tag{6.15}$$

Where f_i is the activity coefficient of component i expressed in wt.% and is given by (Engh 1992, p. 59):

$$\log f_i = e_i^j[\%j] + e_i^i[\%i] \tag{6.16}$$

Using equations (6.14), (6.15), and (6.16) and rearranging we get

$$\ln[\%\mathrm{Al}][\%\mathrm{Ni}] = \left(\frac{\Delta S^\circ}{R} - \frac{\Delta H^\circ}{RT}\right) - 2.3[\%\mathrm{Ni}]\left(e_{\mathrm{Ni}}^{\mathrm{Ni}} + e_{\mathrm{Al}}^{\mathrm{Ni}}\right) - 2.3[\%\mathrm{Al}]\left(e_{\mathrm{Al}}^{\mathrm{Al}} + e_{\mathrm{Ni}}^{\mathrm{Al}}\right) \quad (6.17)$$

Eliminating $e_{\mathrm{Ni}}^{\mathrm{Al}}$ from equation (6.17) using a relation given by Lupis and Elliot (1966):

$$e_{\mathrm{Ni}}^{\mathrm{Al}} = e_{\mathrm{Al}}^{\mathrm{Ni}}\left(\frac{M_{\mathrm{Ni}}}{M_{\mathrm{Al}}}\right) + \frac{1}{230}\left(1 - \frac{M_{\mathrm{Ni}}}{M_{\mathrm{Al}}}\right) \quad (6.18)$$

we get

$$\ln[\%\mathrm{Al}][\%\mathrm{Ni}] = \left(\frac{\Delta S^\circ}{R} - \frac{\Delta H^\circ}{RT}\right) - 2.3[\%\mathrm{Ni}]\left(e_{\mathrm{Ni}}^{\mathrm{Ni}} + e_{\mathrm{Al}}^{\mathrm{Ni}}\right) - 2.3[\%\mathrm{Al}]\left(e_{\mathrm{Al}}^{\mathrm{Al}} + 2.18 e_{\mathrm{Al}}^{\mathrm{Ni}} - 0.005\right) \quad (6.19)$$

Using the data in Table 6.2 and Table 6.4 and values for $e_{\mathrm{Ni}}^{\mathrm{Ni}}$ and $e_{\mathrm{Al}}^{\mathrm{Al}}$ from Table 3.3 in equation 6.19 and solving by the least squares method (Appendix C) gives:

$\Delta H^\circ = 77100$ J/mol

$\Delta S^\circ = 73.2$ J/molK

$e_{\mathrm{Al}}^{\mathrm{Ni}} = -0.032$

Thus the experimental Gibbs energy for the precipitation of AlNi in magnesium is:

$$\Delta G^\circ(\%) = -77100 + 73.2T \quad (6.20)$$

Farner (2000, p. 158) has described a simplified method for the estimate of the standard deviations in the parameters by Bootstrapping (Appendix C). The parameters obtained by fitting and bootstrapping are given in Table 6.8.

TABLE 6.8: The parameters obtained by fitting and bootstrapping.

Parameters	Fitting	Bootstrap
ΔH° J/mol	77100	76900±3000
ΔS° J/molK	73.2	73.0±3.0
$e_{\mathrm{Al}}^{\mathrm{Ni}}$	-0.032	-0.033±0.004
$e_{\mathrm{Ni}}^{\mathrm{Al}}$	-0.075	-0.075±0.009

Standard deviation of $e_{\mathrm{Al}}^{\mathrm{Ni}}$ is calculated using equation (6.21).

If Z is a known function of A, and the standard deviation in A be ΔA. Then the standard deviation ΔZ in Z is given by (Squires 1989, p. 35)

$$(\Delta Z)^2 = \left(\frac{\partial Z}{\partial A}\right)^2 (\Delta A)^2 \tag{6.21}$$

Equation (6.18) is used to calculate $e_{\mathrm{Ni}}^{\mathrm{Al}}$ and the standard deviation in $e_{\mathrm{Ni}}^{\mathrm{Al}}$, using the value $e_{\mathrm{Al}}^{\mathrm{Ni}}$. The second part on the right hand side of equation (6.18) is not taken into account for calculating standard deviation in $e_{\mathrm{Ni}}^{\mathrm{Al}}$.

In Figure 6.9 the estimated values of solubility product of aluminium and nickel from equation (6.17) are compared with the experimental values from Table 6.2 and Table 6.4. All the data in Table 6.4 is used, also from the experiments where only Al_3Ni_2 particles were identified.

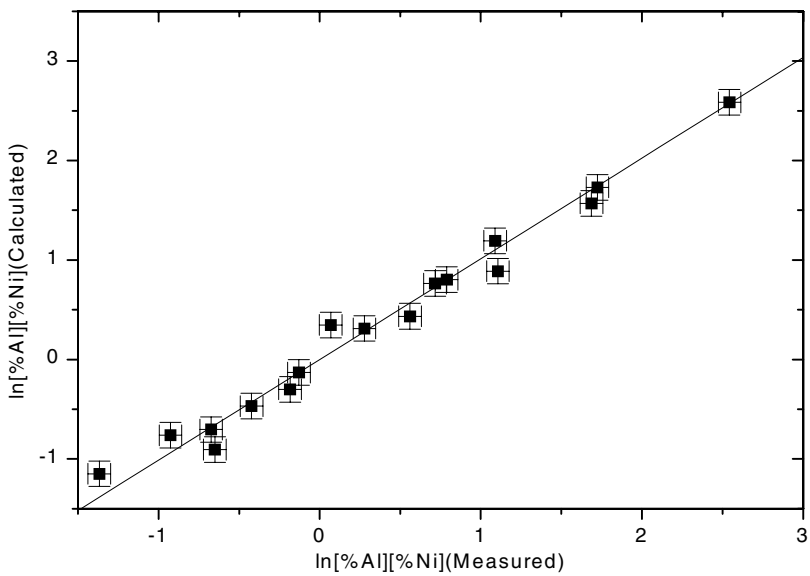

Figure 6.9: Calculated versus measured solubility product of Al and Ni.

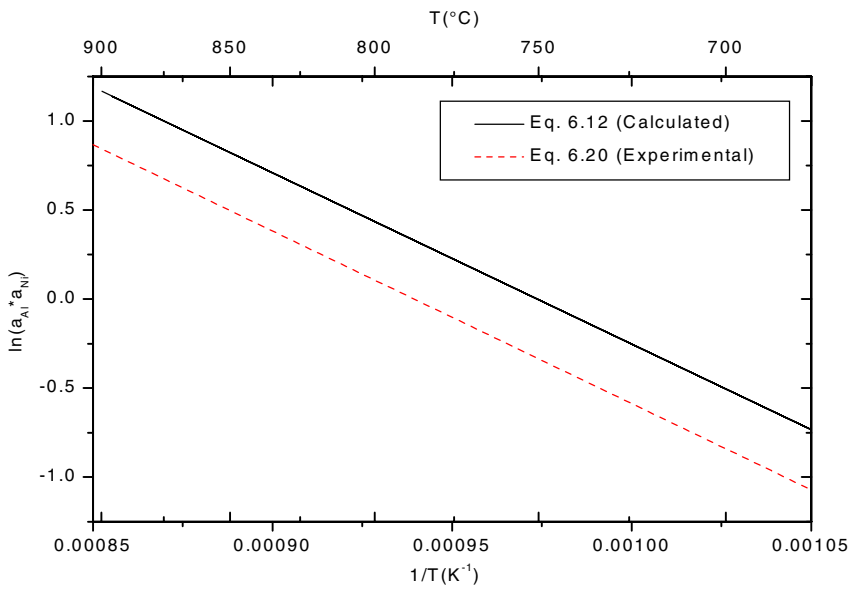

Figure 6.10: Comparison of calculated (equation 6.12) and experimental (equation 6.20) activity product of Al and Ni in magnesium. Note that the inside ticks on the top axis correspond to the outside ticks and labels on the bottom axis and vice versa.

The calculated activity product of aluminium and nickel in magnesium (equations (6.12)) is compared with the experimental activity product of aluminium and nickel in magnesium (equation (6.20)) in Figure 6.10.

6.4 Conclusions

The solubility of nickel in liquid Mg-Al alloys has been measured in the temperature range 650-900°C and for 1-10% aluminium content in the alloys. Compared to pure magnesium the solubility in magnesium-aluminium alloys shows a marked reduction. Addition of only 1 wt.% aluminium reduces nickel solubility from about 37.5 wt.% to about 0.52 wt.% at 700°C whereas at 5 wt.% aluminium the solubility further reduces to 0.22 wt.%.

Linear relationships between the logarithm of solubility of aluminium and nickel, as a function of the inverse of the absolute temperature fit the experimental data well. SEM analysis os samples taken at various temperatures and compositions shows that the precipitated phases in equilibrium with the melt are AlNi and Al_3Ni_2 with the latter becoming more dominant as the aluminium concentration increases.

Thermodynamic data obtained by fitting and "bootstrapping" for the precipitation of AlNi from dissolved aluminium and nickel in magnesium are:

Parameters	Fitting	Bootstrap
ΔH° J/mol	-77100	-76900±3000
ΔS° J/molK	-73.2	-73.0±3.0
$e_{\mathrm{Al}}^{\mathrm{Ni}}$	-0.032	-0.033±0.004
$e_{\mathrm{Ni}}^{\mathrm{Al}}$	-0.075	-0.075±0.009

The values for ΔH° and ΔS° in equation 6.12 are calculated using $\Delta\overline{G}_{\mathrm{Ni}}^{\circ}$ is calculated from the data by Feufel (1993). $\Delta\overline{G}_{\mathrm{Ni}}^{\circ}$ is different from the value given by Kubachewski et al. (1993).

Standard Gibbs energy for solution of 1 mass% nickel in liquid magnesium calculated from the data by Feufel (1993) is:

$$\mathrm{Ni(s)} = \underline{\mathrm{Ni}} \qquad \Delta\overline{G}^{\circ}(\%) = -43500 - 22.2T$$

Standard Gibbs energy for solution of 1 mass% nickel in liquid magnesium calculated from Kubachewski et al. (1993) is more negative and is:

$$\mathrm{Ni(s)} = \underline{\mathrm{Ni}} \qquad \Delta\overline{G}^{\circ}(\%) = -25375 - 55T$$

Chapter 7

Mg-Ni-Fe-X system in iron capsule

In this chapter removal of dissolved nickel from magnesium is studied using an element X. The aim is to review which elements or compounds could be added to molten magnesium to remove nickel. Also removal of iron is studied. Here X can be one of the elements; hafnium, manganese, molybdenum, tantalum, titanium, vanadium or zirconium. These elements were chosen based on a preliminary study by Simensen and Kolby (1995). The criteria for selecting these elements are that:

-The element should have low solubility in molten magnesium at low temperature (700°C)

-The element should form intermetallic phases with nickel

-The element and the intermetallic phases formed should have an electrochemical potential close to that of magnesium in order to avoid pitting corrosion.

7.1 Experimental

Experimental set-up and procedure is given in Chapter 4. Nickel was added to pure magnesium in an amount of 200 ppm. Samples contaminated with nickel were treated at different temperatures and times in contact with an element X. After the capsule treatment the samples were quenched in water. The details of sample split-up and preparation for SEM and ICP-AES analysis are given in Chapter 4. The standard deviation in the temperatures is different because of use of extra insulation in the latter experiments.

7.1.1 Samples treated with hafnium thread

Two samples were treated at 796°C and 661°C for 48 hours and 30 hours using hafnium thread. ICP-AES analysis gave the following results (Table 7.1).

TABLE 7.1: The magnesium samples treated with Hf thread. The remainder in the samples is Mg.

Sample no.	Temperature (°C)	Holding time (hours)	Nickel (ppm)	Iron (ppm)	X (Hf) (ppm)
261	796±0.5	30	210	1150	3600
235	661±1	48	188	282	< 5

On analysing the samples with SEM, we found that there was no formation of intermetallic particles of nickel and hafnium. Figure 7.1 shows white circles of hafnium thread in magnesium matrix in sample no. 261.

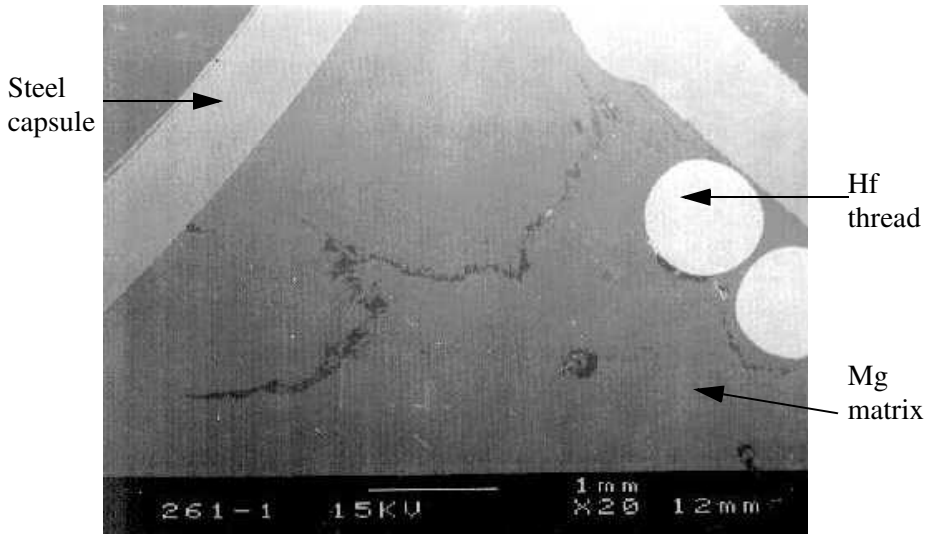

Figure 7.1: Sample 261, treated with hafnium thread (X20).

The results indicate that hafnium dissolve very little in the magnesium and cannot be used to remove nickel from magnesium.

7.1.2 Samples treated with manganese pieces

Two samples were treated using manganese pieces. ICP-AES analysis results are given in Table 7.2.

TABLE 7.2: The magnesium samples treated with Mn pieces.

Sample no.	Temperature (°C)	Holding time (hours)	Nickel (ppm)	Iron (ppm)	X (Mn) (ppm)
236	661±1	48	169	745	-
263	796±0.5	30	201	23000	93000

7.1.2.1 Sample 236

Figure 7.2 shows manganese pieces at the bottom of the sample. In this sample at temperature 661°C no intermetallic particles of Fe-Mn is identified.

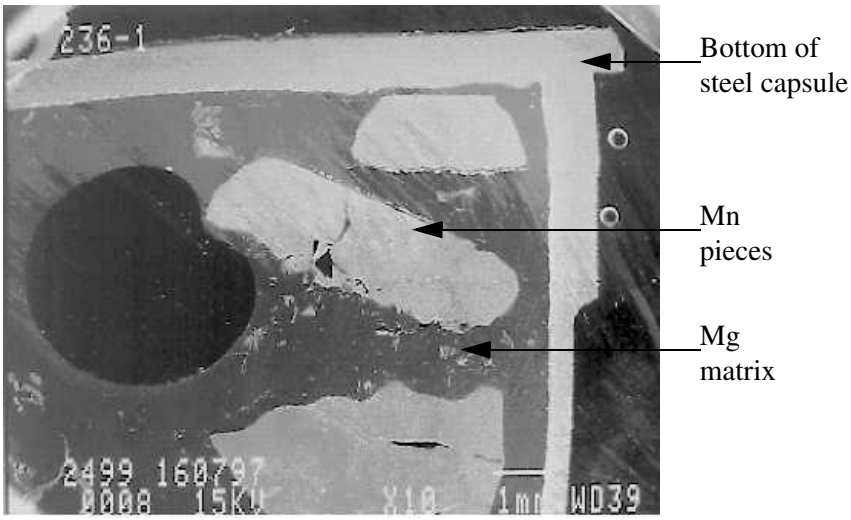

Figure 7.2: Mn pieces at the bottom of sample 236 (X10).

7.1.2.2 Sample 263

At temperature 796°C there is a formation of Fe-Mn intermetallic particles. The particles identified in the magnesium matrix are shown in Figure 7.3. These particles

have an irregular shape and the size of particles is 30-40 μm. The composition of these particles is 20 wt.% Fe and 80 wt.% Mn. The phase corresponding to this composition is γ(Fe,Mn); in this phase manganese is present from 0-100% by weight (Massalski 1990, pp. 1724-1726).

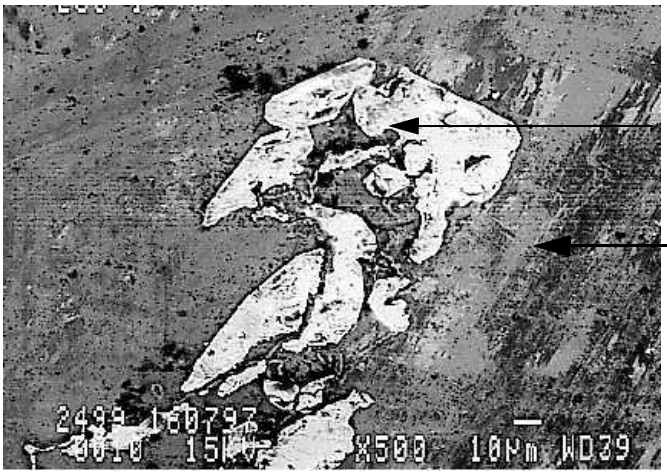

Figure 7.3: γ(Fe,Mn) particles in Sample 263 (X500).

An intermetallic layer is formed near the walls of the steel container. In Figure 7.4 the phase near the wall has 34 wt.% Fe and 66 wt.% Mn and this composition also correspond to γ(Fe,Mn) phase. Some of the analysis shows presence of 0.3-0.7 wt.% Ni in γ(Fe,Mn) phase.

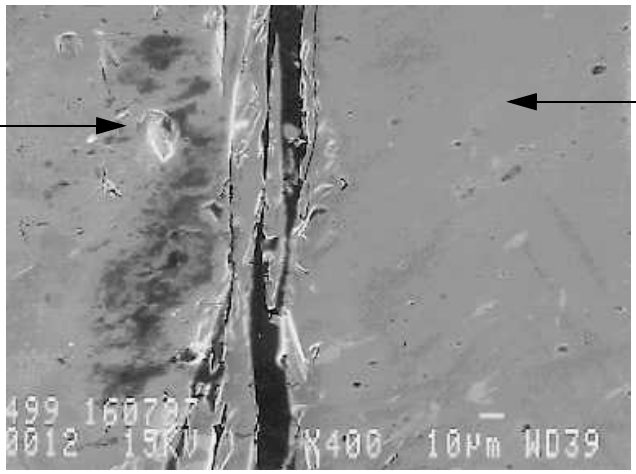

Figure 7.4: Diffusion of Mn in steel capsule in Sample 263 (X400).

7.1.3 Samples treated with molybdenum foil

Two samples were treated with molybdenum foil at 775°C and 659.5°C for 48 hours. ICP-AES analysis gave the following results.

TABLE 7.3: The magnesium samples treated with Mo foil in capsule experiments.

Sample no.	Temperature (°C)	Holding time (hours)	Nickel (ppm)	Iron (ppm)	X (Mo) (ppm)
232	775±5	48	200	470	5
246	659.5±0.5	48	142	86	1300

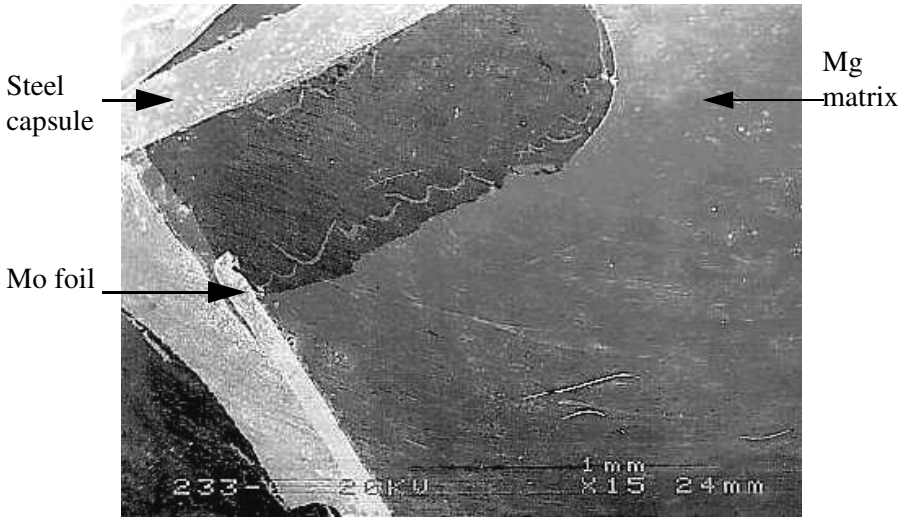

Figure 7.5: Sample 232, treated with molybdenum foil (X15).

Results from ICP-AES (Table 7.3) agree with SEM analysis of the samples. Figure 7.5 shows the bottom of sample 232. The matrix is 99 at.% magnesium. The thin white layer near the wall of the iron capsule is the molybdenum foil. Quantitative analysis of this layer gave its composition to be 99 at.% molybdenum. The higher content of iron in sample 232 than in sample 246 is due to fact that the former was held at a higher temperature. The high values of molybdenum in the bulk magnesium from sample number 246 can be due to contamination by molybdenum foil while drilling out the chips for analysis. We are interested in the presence of intermetallic particles with molybdenum and/or iron containing nickel. On analysing these two

samples such particles were not identified. On this basis it was decided not to carry out any further studies using molybdenum.

7.1.4 Samples treated with tantalum foil

Three different samples were treated using tantalum foil in capsule experiments. The contents of iron, nickel and tantalum after the treatment are given in Table 7.4.
.

TABLE 7.4: The magnesium samples treated with Ta foil

Sample no.	Temperature (°C)	Holding time (hours)	Nickel (ppm)	Iron (ppm)	X (Ta) (ppm)
231	775±5	48	-	-	-
264	796±0.5	30	210	810	<5
245	659.5±0.5	48	153	262	<5

Three different points were analysed by SEM in the matrix of sample no. 231. The composition of the matrix at three different points was about 100 at.% magnesium. No iron or tantalum was indicated in the magnesium matrix. Results from ICP-AES gave no values of iron or tantalum. No results could be drawn from sample no. 231.

7.1.4.1 Sample 264

Figure 7.6 shows a very thin layer of tantalum foil near the capsule wall. It seems that tantalum did not react with magnesium. On analysing different points in the magnesium matrix some particles containing approx. 92 at.% tantalum and 5-7 at.% magnesium were identified. The presence of magnesium in these particles may be caused by the noise in the analysis due to matrix effects. No intermetallic particles of nickel with tantalum were observed.

From sample nos. 231 and 264 and ICP-AES results of sample 245 we can conclude that under the given conditions of temperature and time, tantalum cannot be used for removing nickel from magnesium because of its low solubility in magnesium and there is no formation of Ta-Ni particles.

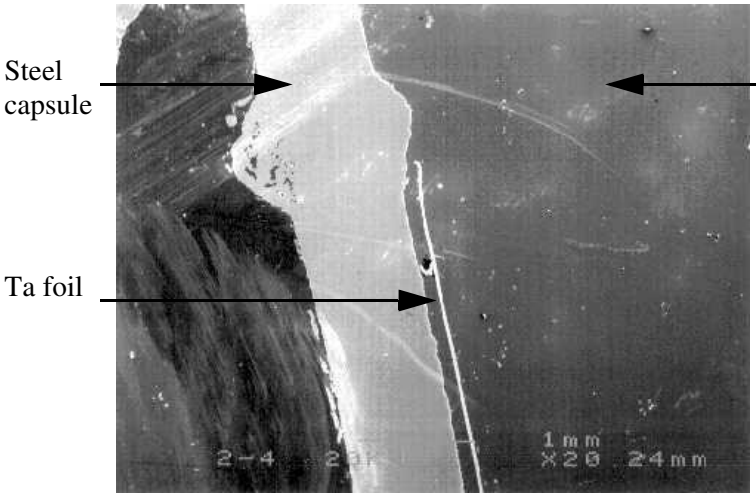

Figure 7.6: Sample 264, treated with tantalum foil (X20).

7.1.5 Samples treated with titanium foil

Two samples were treated with titanium foil. ICP-AES analysis gave the following results (Table 7.5).

TABLE 7.5: The magnesium samples treated with Ti foil

Sample no.	Temperature (°C)	Holding time (hours)	Nickel (ppm)	Iron (ppm)	X (Ti) (ppm)
244	659.5±0.5	48	144	235	55000
241	775±5	48	96	14300	3300

7.1.5.1 Sample 244

Figure 7.7 shows that titanium foil has reacted with magnesium to some extent. Particles with a square shape near the titanium foil contain about 50 at.% Ti and 50 at.% Fe and this composition corresponds to the TiFe phase (Massalski 1990, pp. 1783-1786).

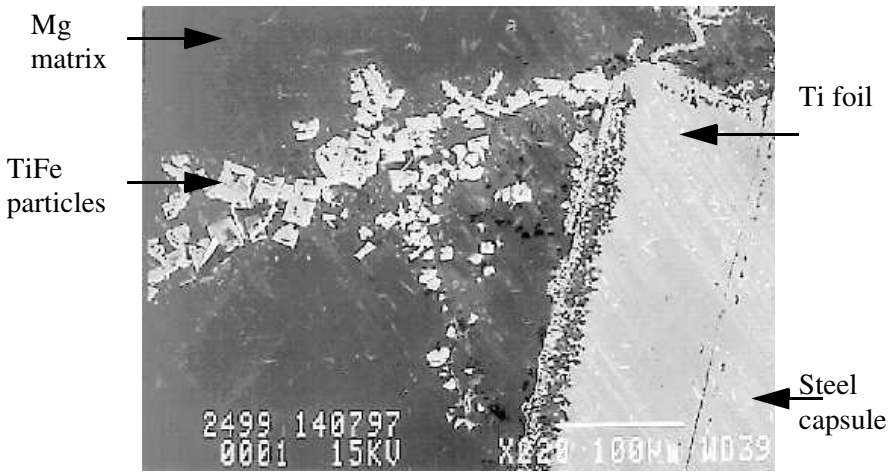

Figure 7.7: Ti-Fe particles near the capsule wall in Sample 244 (X220).

Figure 7.8 shows particles that have no definite shape and have composition about 31 at.% Ti and 62 at.% Fe and this corresponds to the Ti Fe_2 phase (Massalski 1990, pp. 1783-1786).

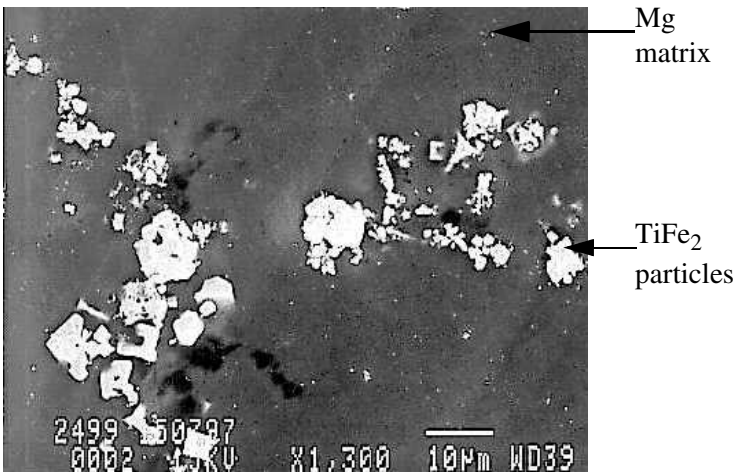

Figure 7.8: $TiFe_2$ particles in Sample 244 (X1300).

7.1.5.2 Sample 241

Figure 7.9 shows a part of titanium foil that is partially dissolved. Iron has diffused into the foil up to 50 at.% and the elongated particles that project from the foil have

composition 46 at.% Ti and 43 at.% Fe and this composition corresponds to the TiFe phase.

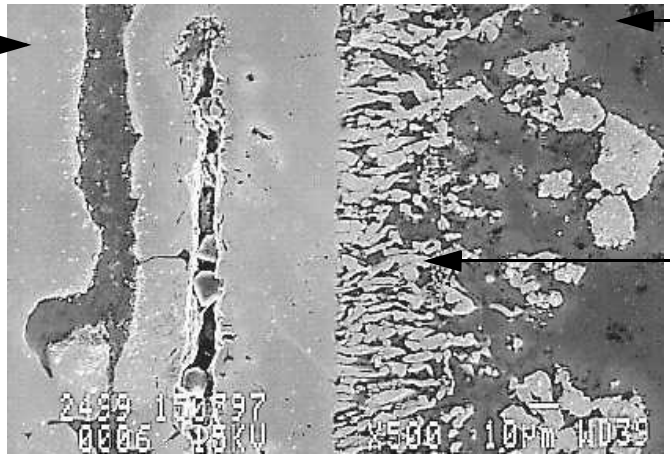

Figure 7.9: Ti-Fe particles near the wall in Sample 244 (X500).

Figure 7.10 shows particles of size about 30 µm which are present at the bottom of the sample. The composition of these particles is 29 at.% Ti and 59 at.% Fe and this composition corresponds to the $TiFe_2$ phase. Some of the TiFe and $TiFe_2$ particles contain 0.4-0.8 at.% Ni. The results indicate that titanium can be used to remove iron and small amounts of nickel. This is in agreement with the previous work (Emley and Fox 1945).

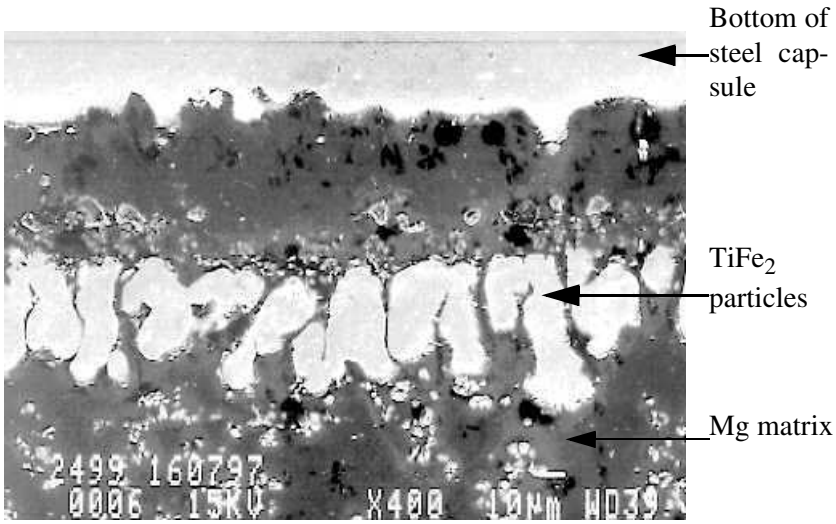

Figure 7.10: $TiFe_2$ particles at the bottom in Sample 241 (X400).

7.1.6 Samples treated with vanadium thread

Two samples were treated with vanadium thread. ICP- AES gave the following results (Table 7.6).

TABLE 7.6: Magnesium samples treated with V thread.

Sample no.	Temperature (°C)	Holding time (hours)	Nickel (ppm)	Iron (ppm)	X (V) (ppm)
262	796±0.5	30	204	790	8
234	661±1	48	178	250	5

7.1.6.1 Sample 262

At 796°C only 8 ppm of vanadium is dissolved in magnesium. White circles in Figure 7.11 are vanadium threads in the magnesium matrix.

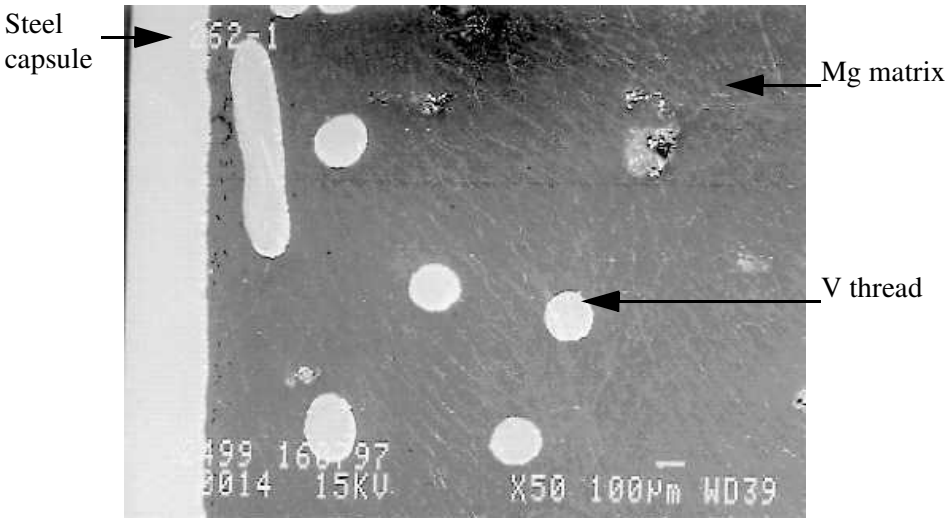

Figure 7.11: Cross section of V threads in Mg matrix in Sample 262 (X100).

Back-scatter image of these vanadium threads shows that there is solid state diffusion of iron in vanadium. This is shown in Figure 7.12. Four different phases are identified and these have the following compositions:

The outermost layer has 87 at.% Fe, 3 at.% Mg and 11 at.% V. The presence of magnesium can be due to the matrix.

The second outermost layer has 67 at.% Fe and 32 at.% V.

The third layer: In this layer iron is 3.5 at.% and vanadium is 96 at.%.

The (fourth) innermost layer is 100 at.% V.

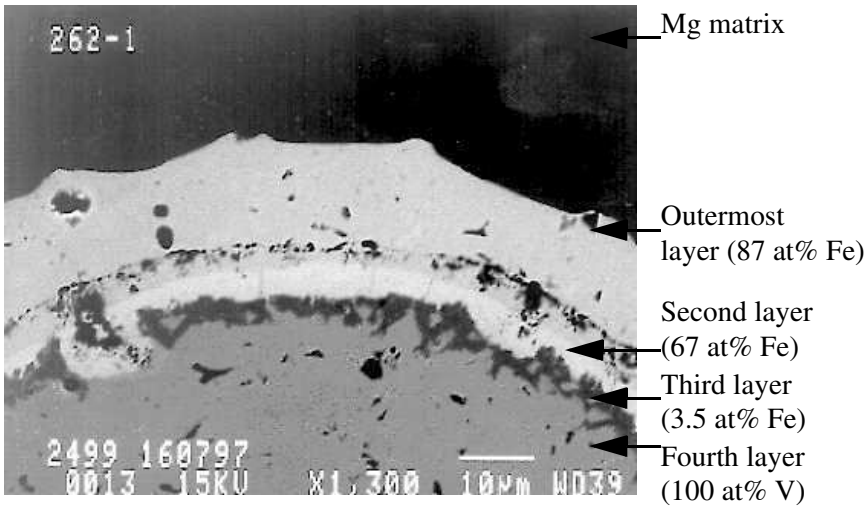

Figure 7.12: Diffusion of Fe in V in Sample 262 (X1300).

From the binary phase diagram of Fe-V we find the formation of (αFe, V) in which the composition of vanadium varies from 0 to 100% by weight (Massalski 1990, pp. 1787-1791).

7.1.6.2 Sample 234

The vanadium particles are shown in Figure 7.11. The composition of the particles is similar to the particles in sample 262.

No phase containing nickel was identified.

7.1.7 Samples treated with zirconium foil

Three samples were treated with zirconium foil in iron capsule. ICP-AES analysis gave the following results (Table 7.7).

TABLE 7.7: The magnesium samples treated with Zr foil.

Sample no.	Temperature (°C)	Holding time (hours)	Nickel (ppm)	Iron (ppm)	X (Zr) (ppm)
243-A	775±5	48	<50	435	12000
243	659.5±0.5	48	<50	103	11000
233	661±1	48	<50	18	15000

7.1.7.1 Sample 243-A

SEM-EDS and microprobe analysis of this sample show that the zirconium dissolves in magnesium. Zirconium and iron form various intermetallic phases (Figure 7.13) also containing nickel and magnesium of different compositions.

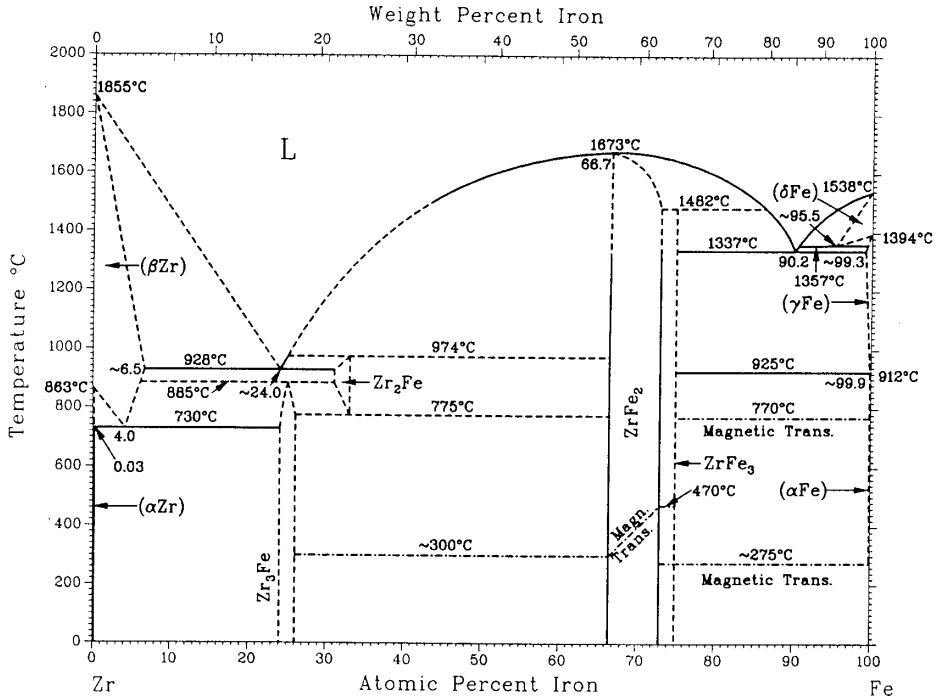

Figure 7.13: Fe-Zr phase diagram (Massalski 1990, p.1799).

The compositions of the magnesium matrix at three different points were above 99 at.% magnesium. Typical composition of nickel-containing particles was 68 at.% zirconium, 18 at.% magnesium, 14 at.% iron and 0.5 at.% nickel. According to Simensen and Horst (1996) it can be assumed that the intermetallic phases in this system do not contain magnesium. The various amounts of magnesium in the particles is believed to be due to the magnesium matrix, since the measuring volume contains both particle and matrix.

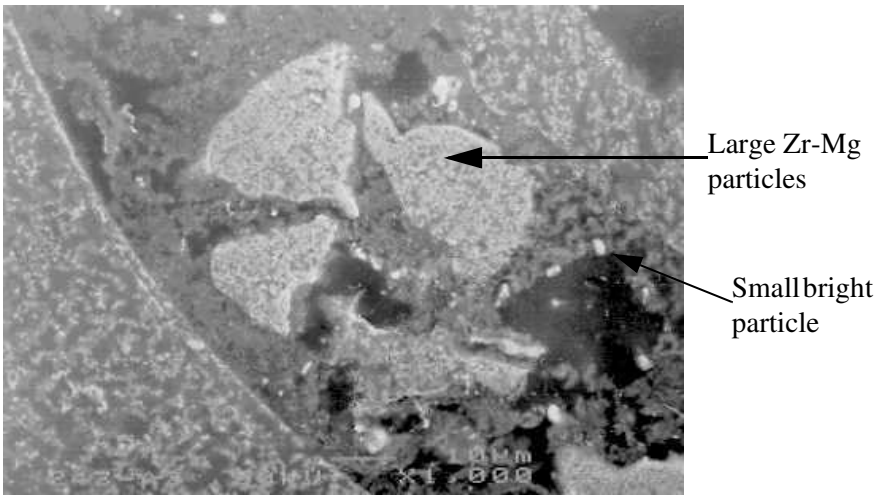

Figure 7.14: Sample 243-A, treated with zirconium foil (X1000).

The larger particles in Figure 7.14, which are brighter than the background, are Zr-Mg particles with 44 at.% Zr and 56 at.% Mg. The small brighter particles which contain nickel contains 62 at.% Mg and 37 at.% Zr.

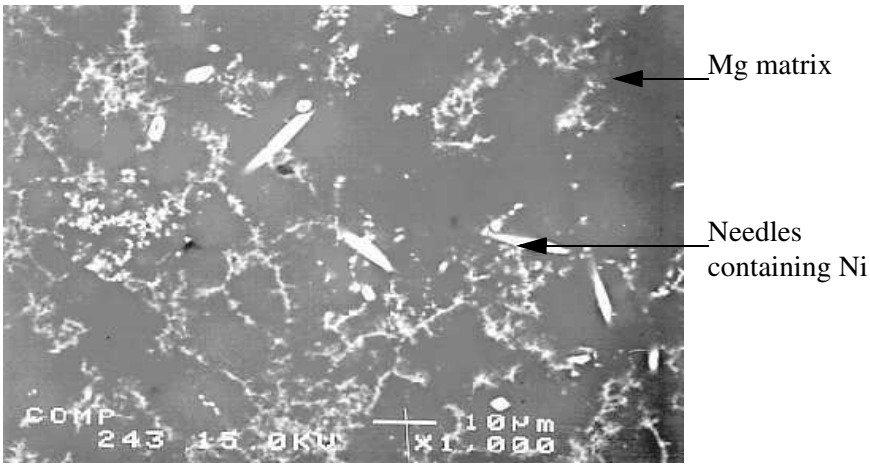

Figure 7.15: Sample 243, treated with zirconium foil (X1000).

7.1.7.2 Sample 243

Intermetallic particles of iron and zirconium also containing nickel were identified in sample 243. The size of the particles is 10-15 µm. These particles look like bright needles (Figure 7.15). Composition of the needles is 3 at.% Ni, 17 at.% Fe, 24 at.% Mg and 56 at.% Zr. The composition of the needles corresponds to the $Zr_3(Fe,Ni)$ phase (Figure 7.13). This indicates that nickel can be removed from magnesium by zirconium and iron.

7.1.7.3 Sample 233

The best results were obtained in sample 233. The zirconium foil was nearly dissolved in the magnesium matrix. Figure 7.16 shows the remaining parts of the zirconium foil after the treatment.

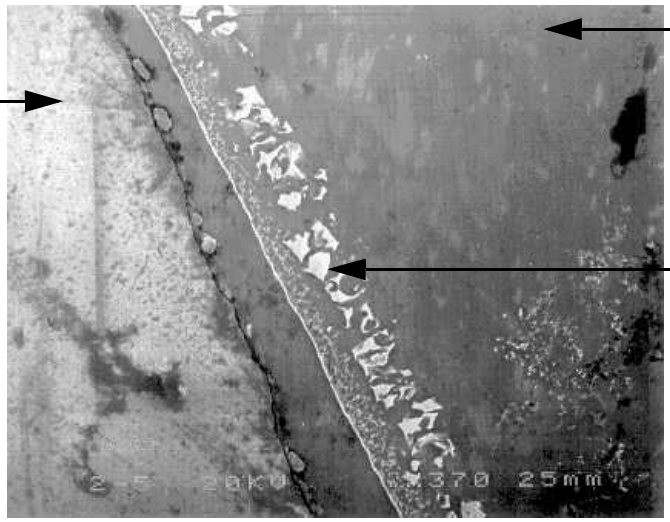

Figure 7.16: Remaining parts of Zr foil in sample 233 (X370).

The white bright particles in Figure 7.16 is the remaining part of the zirconium foil. These are situated where the foil was placed originally near the wall of the steel capsule. Zirconium also reacts with dissolved iron and magnesium and these particles are not as bright as pure zirconium. Since these particles are heavier than the matrix they tend to settle to the bottom. Figure 7.17 shows the Fe-Zr particles at the bottom of sample 233. The composition of these particles is 60 at.% Fe, 5 at.% Mg and 34 at.% Zr.

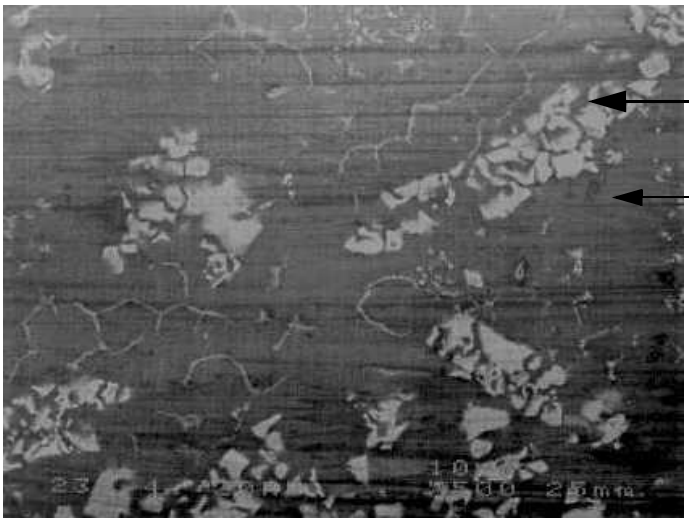

Figure 7.17: Fe-Zr particles near the bottom of the sample 233 (X500).

Figure 7.18 shows a dendrite structure near the wall of the iron capsule. The composition of most of the plates near the dendrite structure is 2 at.% Ni, 29 at.% Fe and 64 at.% Zr. This composition corresponds to Zr_2(Fe, Ni) (Figure 7.13). Some of these plates are 20 μm long and 5 μm thick.

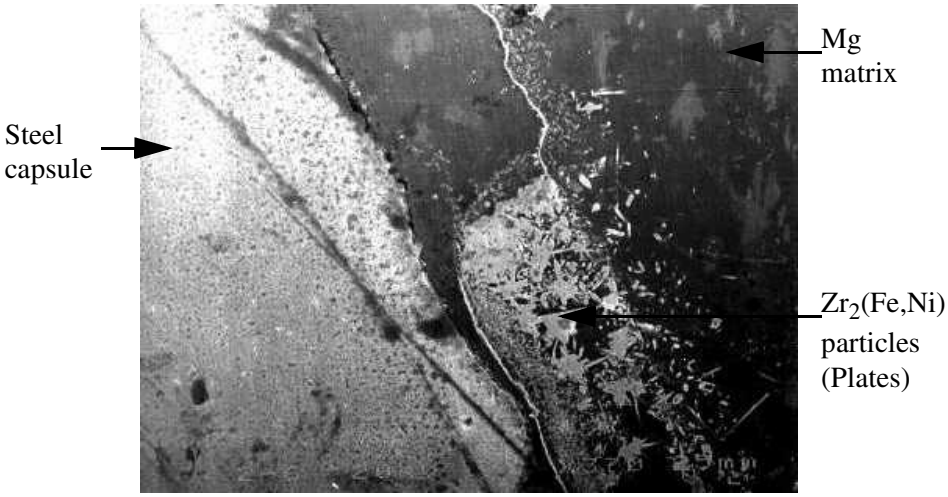

Figure 7.18: Dendrite structure near the wall of iron capsule in Sample 233 (X370).

Needles are very thin and sharper at the ends than the plates, and the composition of these needles is different from the thicker plates. The composition of needles is 2 at.% Ni, 49 at.% Zr, 14 at.% Fe and 35 at.% Mg. Needles are shown in Figure 7.19. The phase corresponding to the needles is Zr_3(Fe,Ni). The specks in Figure 7.19 have a different composition compared to the needles and plates. The composition of a speck is 16 at.% Fe, 1.5 at.% Ni, 78 at.% Zr and 6 at.% Mg and it corresponds Zr_4(Fe, Ni) phase (Figure 7.13). In conclusion nickel can be removed from magnesium by zirconium and iron.

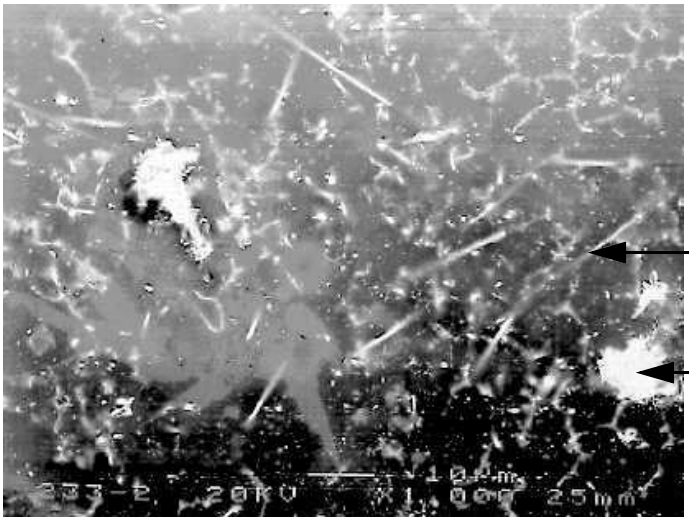

Figure 7.19: Specks and thin needles in Sample 233 (X1000).

7.2 Summary of results and conclusions

In an iron capsule the possibility of removing dissolved nickel from (pure) magnesium has been studied by precipitating with another element X. Element X in this study was Zr, Mo, Mn, V, Hf, Ti or Ta. X was always present as separate phase (in excess). ICP-AES and SEM analysis of samples treated with molybdenum, tantalum, and hafnium did not show any removal of nickel.

Manganese form γ(Fe,Mn) phase containing small amounts of nickel. The results with vanadium indicate that vanadium can remove iron even though the solubility of vanadium in magnesium is low.

The ICP-AES analysis results show the reduction of nickel from 200 ppm to less than 50 ppm in the case of zirconium. SEM analysis of samples treated with zirco-

nium indicated the presence of various Zr-Fe phases also containing nickel. Titanium also reduced the nickel content to some extent.

Compositions of the phases formed are determined by quantitative analysis in SEM and are compared with phase diagrams. From the SEM analysis it is found that zirconium and titanium dissolve in magnesium and form various intermetallic phases with iron. Microprobe investigations confirmed the formation of Fe-Zr particles also containing nickel. These particles contain different amounts of nickel depending on the phase. Three different phases were observed having different shapes and compositions (Table 7.8).

TABLE 7.8: Composition of phases corresponding to different shapes in samples treated with Zr.

Shape	Plate	Needle	Speck
at.% Ni	2.36	2.08	1.40
at.% Fe	28.69	14.12	15.80
at.%Zr	64.31	48.83	78.08
Phase	Zr_2(Fe,Ni)	Zr_3(Fe,Ni)	Zr_4(Fe,Ni)

In summary, zirconium and titanium remove nickel from magnesium by forming various intermetallic phases with iron also containing nickel. The various phases identified are Zr_2(Fe,Ni), Zr_3(Fe,Ni), Zr_4(Fe,Ni), Ti(Fe,Ni) and Ti(Fe,Ni)$_2$.

Chapter 8

Mg-Al-Ni-Fe system in Al_2O_3 crucible

In this chapter the solubilities of nickel and iron have been measured in molten Mg-Al alloy in the composition range 1-10 wt.%Al and temperature range 650-900°C. Precipitated phases at various temperatures and compositions are also identified using microprobe.

8.1 Experimental setup

The furnace, materials and sampling procedure are described in Chapter 5. The method for cooling the samples was improved in this experiment. Earlier a jet of air outside the furnace was used to cool the samples. In this experiment a new cooling device (He cyclone) is developed which cools the sample inside the furnace using helium gas. The cooling device is shown in Figure 5.7. Since the cooling device is placed inside the furnace near the upper lock, it takes less time when the samples start to solidify. Therefore the chances are better for preserving the shape and composition of the particles using this new cooling system. Iron powder was used to study the mutual solubility of nickel and iron. The amount of iron and nickel was added such that there is an excess of these elements in the melt at 900°C. The start composition of all the three series is given in Table D.1 (Appendix D). The supplier and purity of materials used is given in Chapter 5 (Table 5.1).

8.2 Results

At each temperature and composition two samples were taken after approximately 12 hours and 20 hours of settling time. The samples were analysed by ICP-AES technique to determine the chemical composition of the melt. The relative errors in the ICP-AES analysis reported for aluminium and nickel is 5% and for iron is 10%. The mutual sol-

ubility of iron and nickel for various aluminium contents and at various temperatures are given in Table 8.1. When the temperature was fluctuating between two values, the mean value of the temperatures is taken.

TABLE 8.1: ICP-AES analysis of samples at various compositions and temperatures. The remainder is magnesium.

Sample No.	Temperature (^{o}C)	Settling time (Hours)	wt.%Al	wt.%Ni	ppm Fe
612A	900	22	8.64	1.28	284
622A	791.5	22	9.01	0.65	51
632A	702	20.5	8.70	0.29	31
642A	644.5	22	8.67	0.16	34
612B	900	22	5.43	1.17	100
622B	796	24	5.38	0.66	30
632B	705	22.5	5.14	0.31	< 20
642B	648.5	22.75	4.93	0.16	< 20
612C	900	24	2.28	2.51	250
622C	800	29	1.67	1.44	60
632C	697.5	23	0.70	0.70	< 20

It is seen from Table 8.1 that the solubility of both nickel and iron decreases with decreasing temperature and with an increasing aluminium content.

8.3 Microprobe results

The precipitated phases containing iron and nickel, being heavier than the magnesium melt, will settle to the bottom. After approximately 20 hours of settling time (Chapter 5, Figure 5.5) one sample from the bottom was taken to identify the precipitated phases using microprobe. The particles identified at various temperatures and aluminium contents are given in Table 8.2. Concentrations in melt [%] are given in wt.% and concentrations in particles (%) are in at.%.

TABLE 8.2: Composition of the particles in (at.%) identified in samples taken at various temperatures and Al contents in melt. ([%Al] is the Al content in wt.% in the melt. See Table 8.1 for [%Ni] and [%Fe] in the melt)

Sample No.	Temp. (^oC)	[%Al]	(%Al)	(%Ni)	(%Fe)	Phase/Remark
612A	900	8.64	~55	~42	~1-3.5	Al(Ni,Fe)/Figure 8.1
622A	791.5	9.01	~56	~42	~0.5-0.7	Al(Ni,Fe)
632A	702	8.70	~56	~40	~0.6-0.9	Al(Ni,Fe)-$Al_3(Ni,Fe)_2$/ 2-3 μm particles
642A	644.5	8.67				small particles
612B	900	5.43	~53	~41-44	~0.5-0.9	Al(Ni,Fe)/Figure 8.2, Figure 8.3
622B	796	5.38	~54	~44-45	~0.2-0.9	Al(Ni,Fe)/Figure 8.4
632B	705	5.14	~50-52	~36-38	~0.1	Al(Ni,Fe)/4-5 μm particles
642B	648.5	4.93				1 μm particles/difficult to analyse.
612C	900	2.28	~50	~47	~0.2-1.0	Al(Ni,Fe)
622C	800	1.67	~50	~47	~0.2-0.7	Al(Ni,Fe)/Figure 8.5
632C	697.5	0.70				No particle identified.

Particles identified in the sample taken at 900°C and 8.64 wt.% Al in the melt are shown in Figure 8.1. The particles contain approximately 55 at.% Al and 43-45.5 at.% (Fe + Ni) (Table 8.2). This composition corresponds to Al(Ni,Fe) phase (see Figure 6.7). The size of the particles is approximately 10-15 μm.

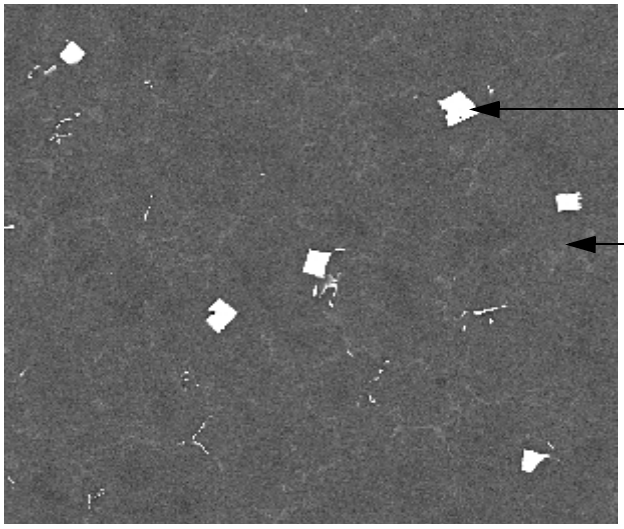

Figure 8.1: Al(Ni,Fe) particles identified for experiment at 900°C and 8.64 wt.%Al in the melt (X400).

The particles identified in the sample taken at 900°C and 5.43 wt.%Al in the melt are shown in Figure 8.2 and Figure 8.3. These particles contain approximately 53-56 at.%Al and approximately 43-44 at.%(Ni+Fe). This composition corresponds to the Al(Ni,Fe) phase (see Figure 6.7). The size of the particles in Figure 8.2 is approximately 20μm and the size of the particles in Figure 8.3 is below 10 μm.

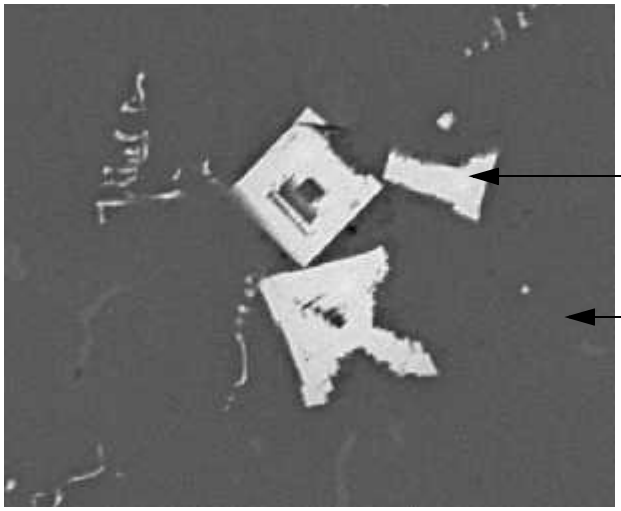

Figure 8.2: Al(Ni,Fe) particles identified for experiment at 900°C and 5.43 wt.%Al in the melt (X1300).

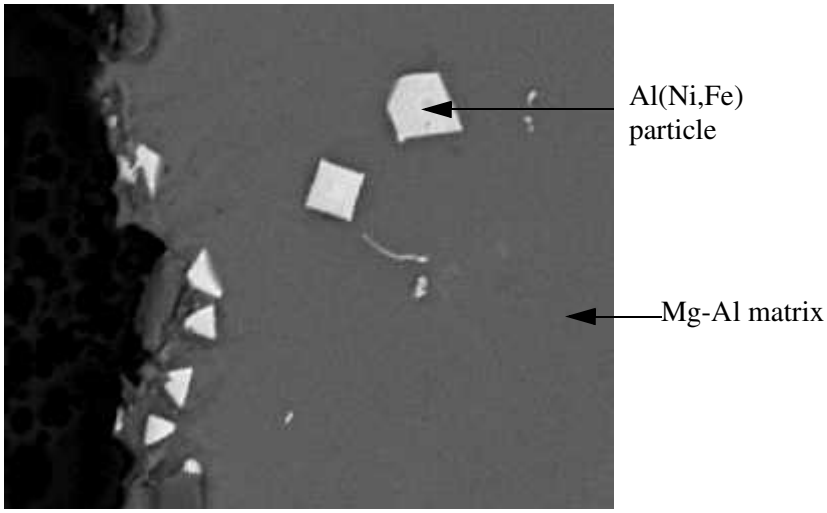

Figure 8.3: Al(Ni,Fe) particles identified for experiment at 900°C and 5.43 wt.%Al in the melt (X1300).

Particles identified in the sample taken at 796°C and 5.38 wt.%Al in the melt are shown in Figure 8.4. The composition of the particles is approximately 54-56 at.%Al and 39-41 at.% (Fe + Ni). This composition corresponds to the Al(Ni,Fe) phase. The size of the particles is approximately 10 μm.

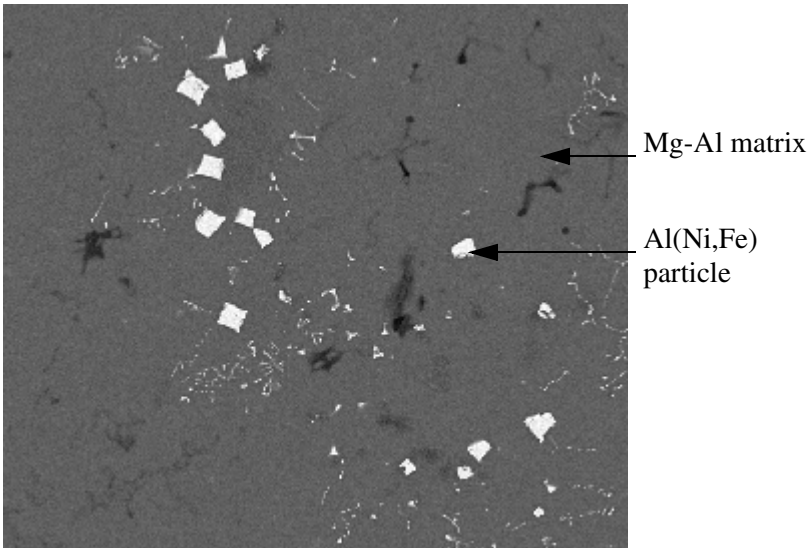

Figure 8.4: Al(Ni,Fe) particles identified in Mg-alloy melt at 796°C and 5.38wt.%Al content (X400).

Particles identified in the sample taken at 800°C and 1.67 wt.%Al in the melt are shown in Figure 8.5. The composition of the particles is approximately 49-51 at.%Al and 47 at.%(Ni + Fe). This composition corresponds to Al(Ni,Fe) phase. The size of the particles is approximately 10-15 μm.

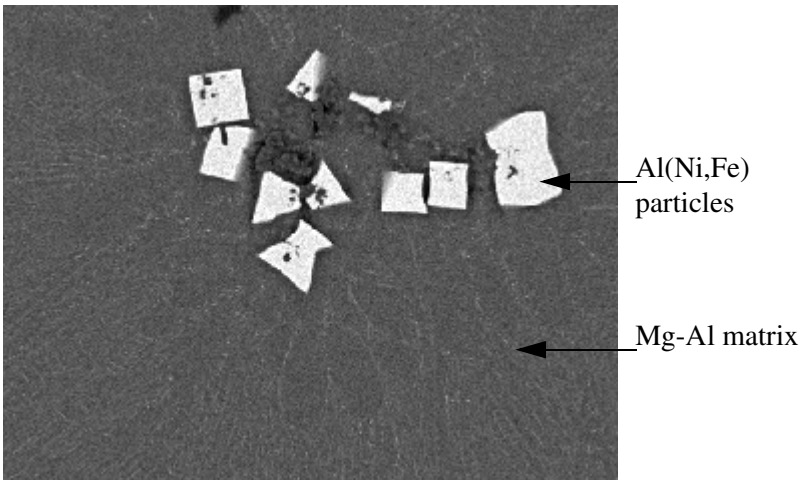

Figure 8.5: Al(Ni,Fe) particles identified in Mg-alloy melt at 800°C and 1.67 wt.%Al content.

It is seen from the microprobe results that for aluminium contents varying from 0.7-8.7% in the melt, the contents of nickel and aluminium in the particles are close to AlNi phase.

8.4 Thermodynamics

The dissolution reaction for the phase Al(Ni,Fe) in molten magnesium alloy is assumed to be given by the "line compound" $AlNi_{\alpha}Fe_{(1-\alpha)}$ where α is a constant to be determined. Also $(1-\alpha)$ is close to one (see Table 8.2).

$$\mathrm{Al(Ni_{\alpha}, Fe_{(1-\alpha)})} = \underline{\mathrm{Al}} + \alpha\underline{\mathrm{Ni}} + (1-\alpha)\underline{\mathrm{Fe}} \tag{8.1}$$

$$-RT\ln K_{\mathrm{Al(Ni_{\alpha}, Fe_{(1-\alpha)})}} = -RT\ln\frac{a_{\mathrm{Al}} \times a_{\mathrm{Ni}}^{\alpha} \times a_{\mathrm{Fe}}^{(1-\alpha)}}{a_{\mathrm{Al(Ni_{\alpha}, Fe_{(1-\alpha)})}}} = \Delta G^{\circ} \tag{8.2}$$

We will make the following assumptions:

1. $a_{\mathrm{Al(Ni_{\alpha},\,Fe_{(1-\alpha)})}} = 1$ for the "line compound" $\mathrm{AlNi_{\alpha}Fe_{(1-\alpha)}}$.

2. Iron in pure magnesium should obey Henry's law (Schneider and Stendel 1960). Table 8.1 indicates that the iron content in the melt is low enough to assume that iron obeys Henry's law in our system. Therefor the activity of iron in equation (8.2) will be taken equal to its concentration.

3. The interaction between the solute atoms nickel and iron is neglected ($e_{\mathrm{Ni}}^{\mathrm{Fe}} = 0$ and $e_{\mathrm{Fe}}^{\mathrm{Ni}} = 0$).

4. The interaction coefficients $e_{\mathrm{Ni}}^{\mathrm{Al}}$, $e_{\mathrm{Al}}^{\mathrm{Ni}}$, and $e_{\mathrm{Al}}^{\mathrm{Fe}}$ are assumed to be constant in our temperature range.

Activity of a component *i* is given by:

$$a_i = f_i[\%i]. \tag{8.3}$$

Activity coefficient *f* for aluminium, nickel, and iron will be given by:

$$\log f_{\mathrm{Al}} = e_{\mathrm{Al}}^{\mathrm{Al}}[\%\mathrm{Al}] + e_{\mathrm{Al}}^{\mathrm{Ni}}[\%\mathrm{Ni}] + e_{\mathrm{Al}}^{\mathrm{Fe}}[\%\mathrm{Fe}] \tag{8.4}$$

Using assumption 3

$$\log f_{\mathrm{Ni}} = e_{\mathrm{Ni}}^{\mathrm{Ni}}[\%\mathrm{Ni}] + e_{\mathrm{Ni}}^{\mathrm{Al}}[\%\mathrm{Al}] \tag{8.5}$$

From assumption 1

$$f_{\mathrm{Fe}} = 1 \tag{8.6}$$

Using equations (8.3), (8.4), (8.5), and (8.6) in equation (8.2) and rearranging, we get:

$$\ln[\%\mathrm{Al}][\%\mathrm{Ni}]^{\alpha}[\%\mathrm{Fe}]^{(1-\alpha)} = \left(\frac{\Delta S^{\circ}}{R} - \frac{\Delta H^{\circ}}{RT}\right) \tag{8.7}$$

$$-2.3\left\{e_{\mathrm{Al}}^{\mathrm{Al}}[\%\mathrm{Al}] + e_{\mathrm{Al}}^{\mathrm{Ni}}[\%\mathrm{Ni}] + e_{\mathrm{Al}}^{\mathrm{Fe}}[\%\mathrm{Fe}] + \alpha(e_{\mathrm{Ni}}^{\mathrm{Al}}[\%\mathrm{Al}] + e_{\mathrm{Ni}}^{\mathrm{Ni}}[\%\mathrm{Ni}])\right\}$$

Using data in Table 8.1 and the values e_{Al}^{Al}, e_{Ni}^{Ni}, e_{Ni}^{Al}, and e_{Al}^{Ni} from the Mg-Al-Ni system and solving the equation (8.7) using the least squares method, the following values are obtained (Appendix D):

ΔH° = 75300 J/mol

ΔS° = 69.3 J/molK

e_{Al}^{Fe} = 0.85, and α = 0.89

e_{Fe}^{Al} = 1.75 is calculated using equation (6.18) replacing nickel with iron.

An estimate of the standard deviation for each parameters is obtained by "Bootstrapping" (Appendix C). For the Bootstrap calculation, α is set to 0.89 before determining ΔH°, ΔS°, and e_{Al}^{Fe}. The parameters obtained by fitting and Bootstrapping for the precipitation of stoichiometric $Al(Ni_{0.89},Fe_{0.11})$ phase in magnesium alloy melt are given in Table 8.3.

TABLE 8.3: The parameters obtained by fitting and bootstrapping.

Parameters	Fitting	Bootstrap
ΔH°	-75300	-79200±6900
ΔS°	-69.3	-77.1±8.0
e_{Al}^{Fe}	0.85	4.11±4.61
e_{Fe}^{Al}	1.75	8.50±9.54

Since the estimated standard deviations in e_{Al}^{Fe} and e_{Fe}^{Al} are so large for the Bootstrap method, we have recalculated ΔH° and ΔS° by fitting and Bootstrapping taking e_{Al}^{Fe} = 0. The parameters thus obtained are given in Table 8.4.

TABLE 8.4: The parameters obtained by fitting and Bootsrapping for $e_{\mathrm{Al}}^{\mathrm{Fe}} = 0$

Parameters	Fitting	Bootstrap
$\Delta H°$	-75300	-74100±3900
$\Delta S°$	-69.3	-68.0±3.8

Thus for $\mathrm{Al(Ni_{0.89},Fe_{0.11})}$ = <u>Al</u> + 0.89<u>Ni</u> + 0.11<u>Fe</u>, Gibbs energy will be given by:

$$\Delta G°(\%) = 75300 - 69.3\mathrm{T} \tag{8.8}$$

For AlNi = <u>Al</u> + <u>Ni</u> (see equation 6.20)

$$\Delta G°(\%) = 77100 - 73.2\mathrm{T} \tag{8.9}$$

Activity product from equations (8.8) and (8.9) are plotted in Figure 8.6. The logarithm of calculated activity product of aluminium, nickel, and iron for the data in Table 8.1 against temperature is also plotted.

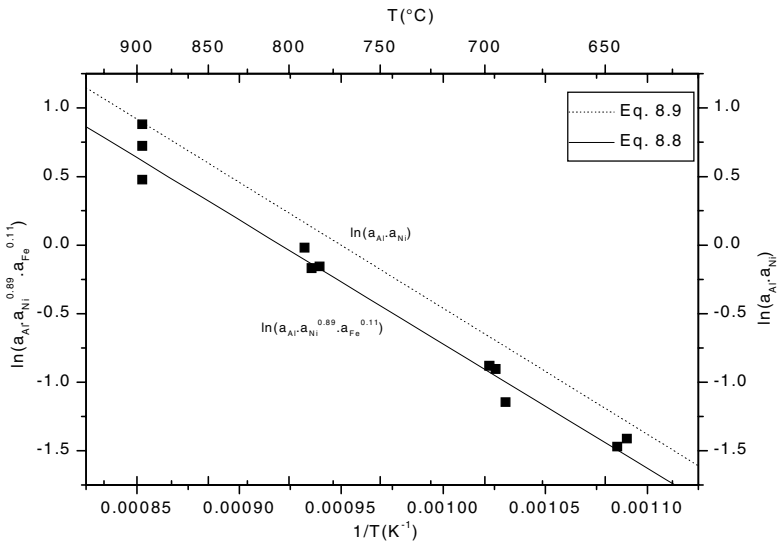

Figure 8.6: Activity products from equations (8.8) and (8.9) are compared. The points are the logarithm of calculated activity product of Al, Ni, and Fe at various temperatures for the data in Table 8.1. Note that the inside ticks on the top axis correspond to the outside ticks and labels on the bottom axis and vice versa.

The values for $\Delta H°$ and $\Delta S°$ in equation (8.9) for the formation of AlNi are close to the $\Delta H°$ and $\Delta S°$ in equation (8.8) for the formation of $Al(Ni_{0.89,}Fe_{0.11})$ indicating that iron has little or no effect on the solubility of nickel in Mg-Al alloys.

8.5 Conclusions

The solubilities of iron and nickel in Mg-Al alloys have been measured in the temperature range 650-900°C and 0.70-9.01 wt.%Al content in the alloys. For Mg-Al alloys saturated with iron and nickel, microprobe analysis of the samples shows that the composition of the precipitated phase contains small amounts of iron but is close to the AlNi composition. The iron content in the particles is below 3.5 at.%. The nickel content in the melt remains below 2.5 wt.% and the iron content below 284 ppm by mass.

The thermodynamic data obtained by fitting and bootstrapping for the precipitation of stoichiometric $Al(Ni_{0.89,}Fe_{0.11})$ phase in magnesium alloy melt are:

Parameters	Fitting	Bootstrap
$\Delta H°$ J/mol	-75300	-74100±3900
$\Delta S°$ J/molK	-69.3	-68.0±3.8
e_{Al}^{Fe}	0	0
e_{Fe}^{Al}	0	0

For $Al(Ni_{0.89,}Fe_{0.11})$ = $\underline{Al}$ + 0.89$\underline{Ni}$ + 0.11$\underline{Fe}$ in Mg-Al melt, Gibbs energy will be given by:

$\Delta G°(\%)$ = 75300 - 69.3T

and for AlNi = $\underline{Al}$ + $\underline{Ni}$ in Mg-Al melt (see equation 6.20)

$\Delta G°(\%)$ = 77100 - 73.2T

$\Delta G^{\circ}(\%)$ for the formation of AlNi is close to $\Delta G^{\circ}(\%)$ for the formation of $Al(Ni_{0.89,}Fe_{0.11})$ indicating that iron has little or no effect on the solubility of nickel in Mg-Al alloys.

Chapter 9

Mg-Al-Ni-Mn system in Al_2O_3 crucible

The effect of manganese on nickel solubility has not yet been determined. In this chapter the mutual solubilities of nickel and manganese in magnesium-aluminium alloys have been studied in the temperature range 650-900°C and aluminium content 1-10wt.%. Precipitated phases at various temperatures and compositions are also identified using a microprobe.

A laboratory scale furnace described in Chapter 5 has been used to study the mutual solubilities of nickel and manganese in magnesium-aluminium alloys. An alumina crucible containing predetermined contents of magnesium, aluminium, nickel, and manganese was heated to 915°C in an inert atmosphere. The melt was bubbled with argon gas for approximately four hours. The amount of manganese and iron was added such that there is an excess of these elements in the melt at 900°C. The geometry and purity of the elements used are given in Table 5.1. The temperature was lowered to 900°C and the melt was held for 20 hours (see Figure 5.5) to settle down any precipitated phase and undissolved nickel or manganese. After the settling time one sample was taken from the top of the melt and analysed by ICP-AES technique to determine the composition of the melt, and one sample was taken from the bottom of the crucible to identify the precipitated phases using microprobe. The temperature of the furnace was dropped gradually to 850, 800, 750, 700, and 660°C and at each temperature two samples were taken after 20 hours. The same procedure was employed for three different magnesium-aluminium alloys. The three different alloys studied are Mg-10% Al, Mg-5% Al, and Mg-1% Al.

9.1 Results

The results of samples analysed by ICP-AES are given in Table 9.1. When temperature fluctuates between two values then mean of two values is taken.

TABLE 9.1: Composition of the samples analysed by ICP-AES. The melts were given a settling time of about 20 hours. The remainder is magnesium.

Sample no.	Temperature (°C)	[%Al]	[%Ni]	[%Mn]
1012A	898	1.37	2.13	3.14
1022A	850	1.28	2.12	2.85
1032A	799	0.37	0.85	0.89
1042A	751	0.81	1.45	1.72
1052A	701	0.89	1.62	1.89
1062A	668	0.38	0.88	0.92
1012B	890	4.54	1.25	2.44
1022B	840	4.05	0.86	1.80
1032B	792	3.68	0.61	1.26
1042B	744	3.32	0.40	0.87
1052B	695	3.09	0.26	0.58
1062B	662	2.91	0.18	0.41
1012C	899	10.6	1.52	1.19
1022C	845	10.7	1.05	1.18
1032C	800	10.3	0.70	0.99
1042C	751.5	10.1	0.48	0.70
1052C	702.5	10.0	0.36	0.47
1062C	664	10.0	0.27	0.33

9.2 Microprobe results

While cooling the melt particles containing nickel and manganese will settle to the bottom of the crucible. Composition of the particles identified in samples taken at various temperatures and aluminium content is presented in Table 9.2. The composition is compared with Figure 9.1 to identify the phase. Compositions in the melt will be given by [mass%] and in particles by (atomic%).

TABLE 9.2: Composition of the phases identified using microprobe (see Table 9.1 for the melt composition).

Temp. (°C)	[wt%Al]	(at%Al)	(at%Ni)	(at%Mn)	Phase/Remark
898	1.37	~36	~19	~43	(βMn,Ni)/Figure 9.2
850	1.28	~38	~20	~41	(βMn,Ni)
799	0.37	~39	~21	~39	(βMn,Ni)
751	0.81	~44	~31	~24	(βMn,Ni)+$Al_8(Mn,Ni)_5$/ Figure 9.3
701	0.89	~48	~47	~3	$Al_8(Mn,Ni)_5$/Al(Ni,Mn)/ 1μm particles
668	0.38	~48	~44	~6	$Al_8(Mn,Ni)_5$/Figure 9.4
890	4.54	~47	~15	~36	$Al_8(Mn,Ni)_5$/Figure 9.5
840	4.05	~46	~15	~37	(βMn,Ni)+$Al_8(Mn,Ni)_5$/ Figure 9.6
792	3.68	~48	~14	~36	$Al_8(Mn,Ni)_5$/Figure 9.7
744	3.32	~45	~12	~32	$Al_8(Mn,Ni)_5$
695	3.09	~47	~13	~35	$Al_8(Mn,Ni)_5$
662	2.91	~49	~13	~34	$Al_8(Mn,Ni)_5$
899	10.6	~52	~21	~25	$Al_8(Mn,Ni)_5$
845	10.7	~53	~21	~23	$Al_8(Mn,Ni)_5$/Figure 9.8

TABLE 9.2: Composition of the phases identified using microprobe (see Table 9.1 for the melt composition).

Temp. (°C)	[wt%Al]	(at%Al)	(at%Ni)	(at%Mn)	Phase/Remark
800	10.3	~53	~33	~14	$Al_8(Mn,Ni)_5$
751.5	10.1	~53	~18	~27	$Al_8(Mn,Ni)_5$/Figure 9.9
702.5	10.0	~59	~37	~4	$Al_8(Mn,Ni)_5$
664	10.0	~55	~40	~5	$Al_8(Mn,Ni)_5$

Al-Mn phase diagram is shown in Figure 9.1. We notice that Al_8Mn_5 is a stable phase with manganese composition varying from 37 at.% to 51 at.% at 800°C.

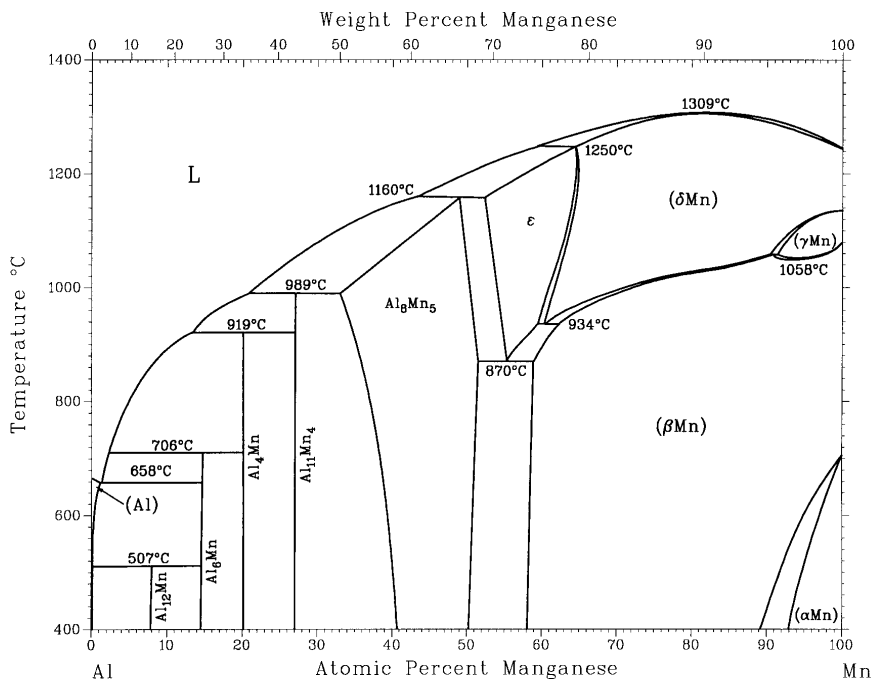

Figure 9.1: Al-Mn phase diagram (Massalski 1996).

At 898°C and 1.37wt.% Al, particles in equilibrium with the melt are shown in Figure 9.2. The composition of the particles (see Table 9.2) corresponds to (βMn,Ni) phase (Figure 9.1). The size of the particles is approximately 7-10μm.

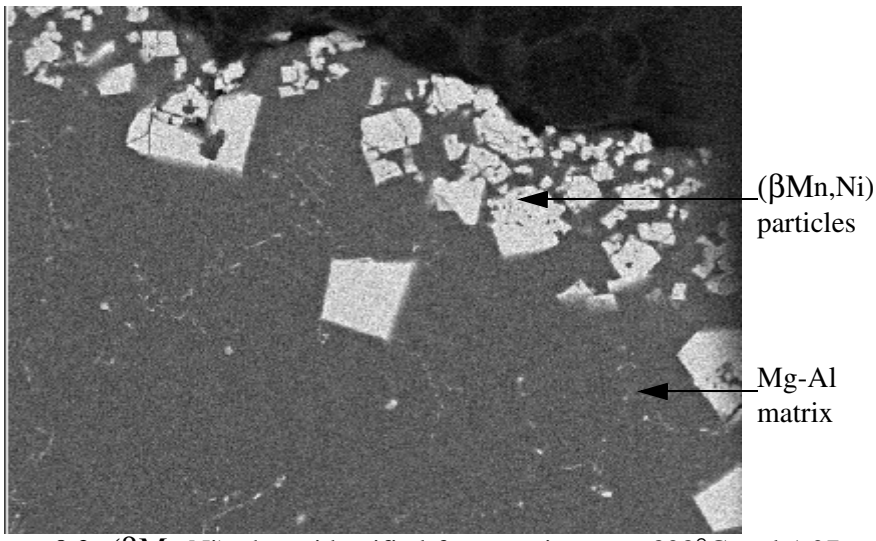

Figure 9.2: (βMn,Ni) phase identified for experiment at 898°C and 1.37wt.% Al (X1500).

As the temperature was dropped there was an increase in the aluminium content in the (βMn,Ni) phase (see Table 9.2). At 751°C and 0.81 wt.% Al, particles identified in the melt are shown in Figure 9.3. The composition of the particles (see Table 9.2) correspond to (βMn,Ni) + $Al_8(Mn,Ni)_5$ phase (Figure 9.1). The size of the particle in Figure 9.3 is approximately 10μm.

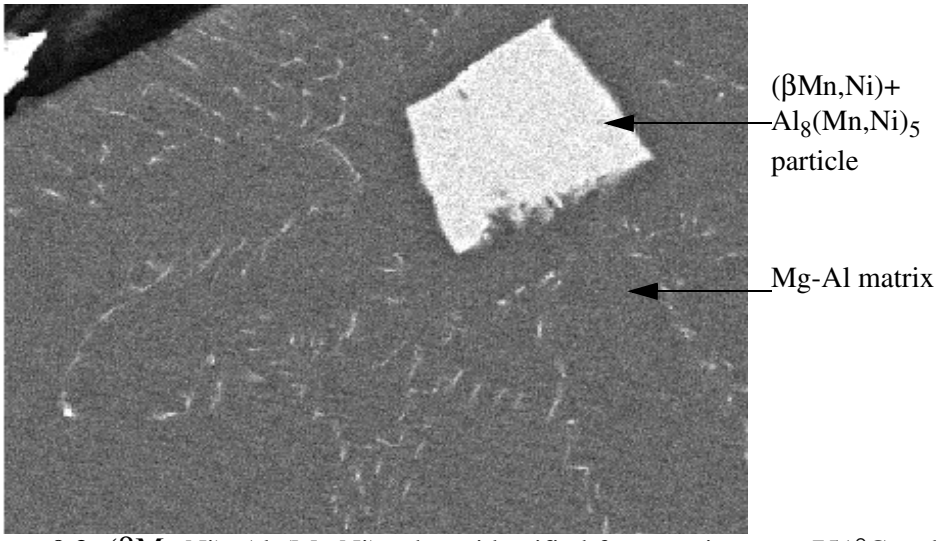

Figure 9.3: (βMn,Ni)+$Al_8(Mn,Ni)_5$ phase identified for experiment at 751°C and 0.81wt.% Al (X2000).

As we further decrease the temperature, the composition of the particles (see Table 9.2) identified in sample taken at 668°C and 0.38wt.% aluminium content corresponds to $Al_8(Mn,Ni)_5$ (Figure 9.1). The content of nickel in these particles is high e.g. the nickel content in the particles identified in the sample taken at 668°C and 0.38wt.% aluminium is approximately 44at.% (Figure 9.4). The particles size is approximately 50μm.

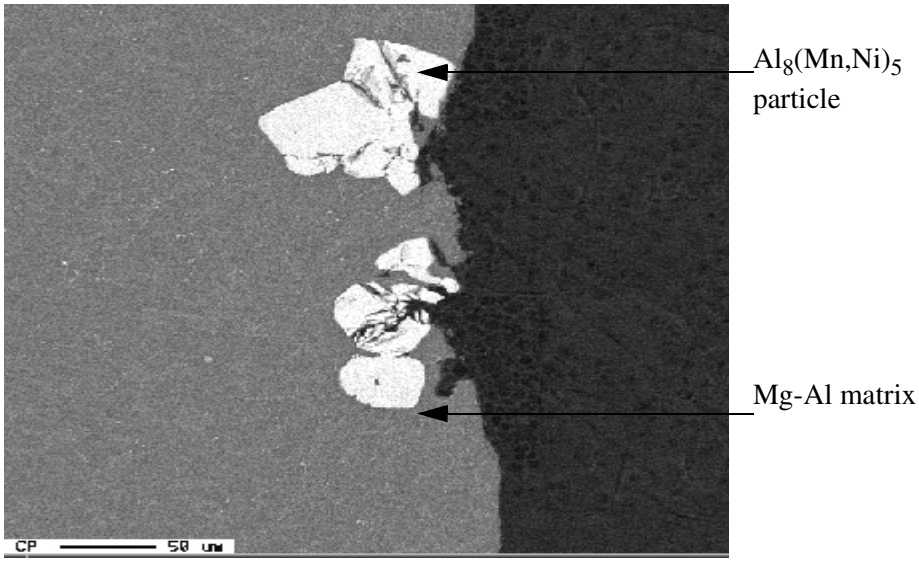

Figure 9.4: $Al_8(Mn,Ni)_5$ particles identified for experiment at 668°C and 0.38wt.% Al (X230).

Particles identified in the sample taken at 701°C and 0.89 wt.% aluminium in the melt were about 1μm and difficult to analyse.

In the other two series, where the aluminium start content was about 5wt.% and 10wt.%, respectively, the precipitated phase in equilibrium with the melt was $Al_8(Mn,Ni)_5$. Figure 9.5 shows the particles identified in the sample taken at 890°C and 4.54 wt.% aluminium content. The composition of these particles (see Table 9.2) corresponds to $Al_8(Mn,Ni)_5$ and the particles are about 20μm long and 5μm wide.

Table 9.2 shows that at 840°C and 4.05 wt.% aluminium content, the phase identified is (βMn,Ni) + $Al_8(Mn,Ni)_5$ (Figure 9.6). If we carefully look at the composition of this phase in Table 9.2 we find that the composition is close to the phase boundary of $Al_8(Mn,Ni)_5$. The morphology and size of particles in Figure 9.6 are similar to

particles in Figure 9.7 that correspond to $Al_8(Mn,Ni)_5$ phase. Particles in Figure 9.7 were identified in the sample taken at 792°C and 3.68 wt.% aluminium in the melt. Based on the above two reasons we will assume that the phase in equilibrium at 840°C and 4.05 wt.% aluminium content is $Al_8(Mn,Ni)_5$ and not (βMn,Ni) + $Al_8(Mn,Ni)_5$.

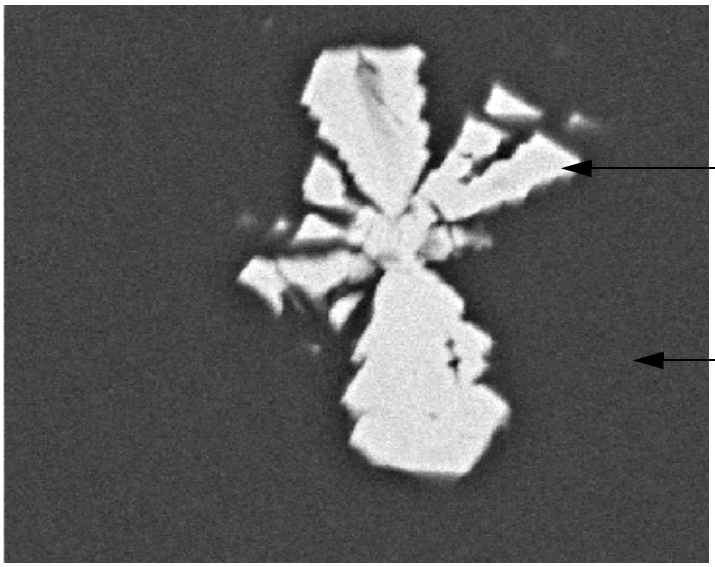

Figure 9.5: $Al_8(Mn,Ni)_5$ phase identified for experiment at 890°C and 4.54 wt.% Al (X2700).

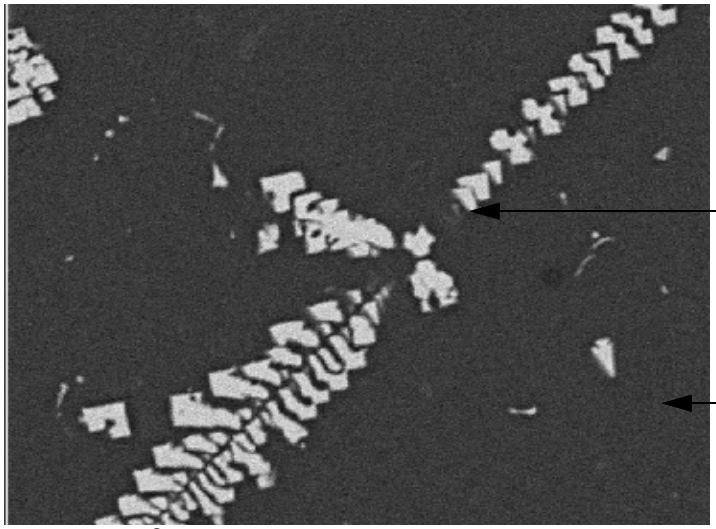

Figure 9.6: (βMn,Ni)+$Al_8(Mn,Ni)_5$ particles identified for experiment at 840°C and 4.05 wt.% Al (X1000).

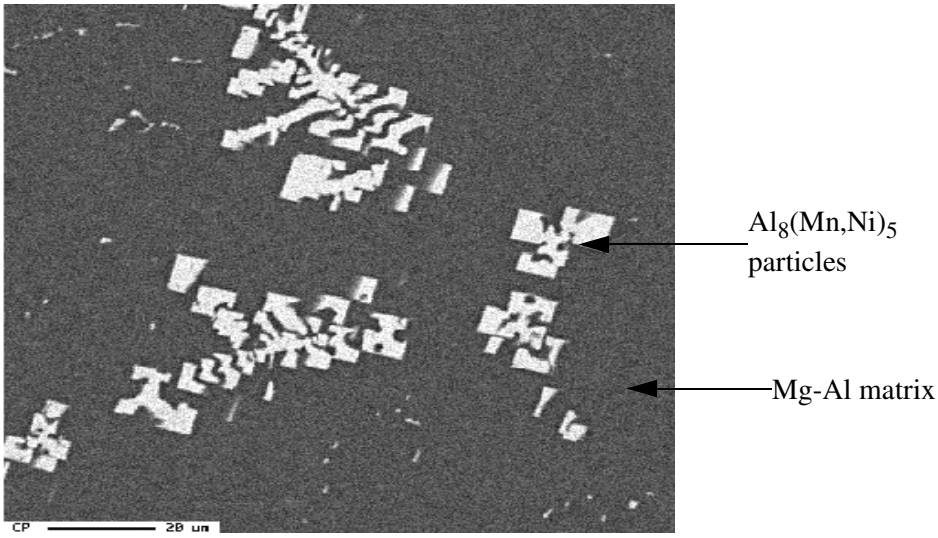

Figure 9.7: $Al_8(Mn,Ni)_5$ particles identified for experiment at 792°C and 3.68 wt.% Al (X800).

For aluminium contents higher than 10 wt.% the phase in equilibrium with the melt is $Al_8(Mn,Ni)_5$ at all temperatures. Figure 9.8 shows the particles (see Table 9.2) identified in the sample taken at 845°C and 10.7 wt.% aluminium in the melt. The composition of the particles correspond to $Al_8(Mn,Ni)_5$ (see Table 9.2) and the size of the particles is about 10µm.

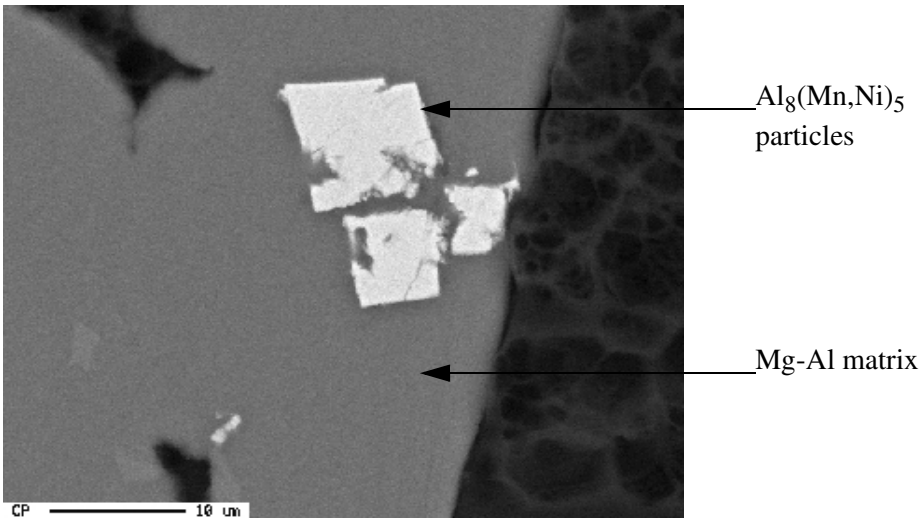

Figure 9.8: $Al_8(Mn,Ni)_5$ particles identified for experiment at 845°C and 10.7 wt.% Al (X2000).

The particles identified in the sample taken at 751.5°C and 10.1 wt.% aluminium in the melt are shown in Figure 9.9. The composition the particles (see Table 9.2) correspond to $Al_8(Mn,Ni)_5$. The size of the particles is approximately 5µm.

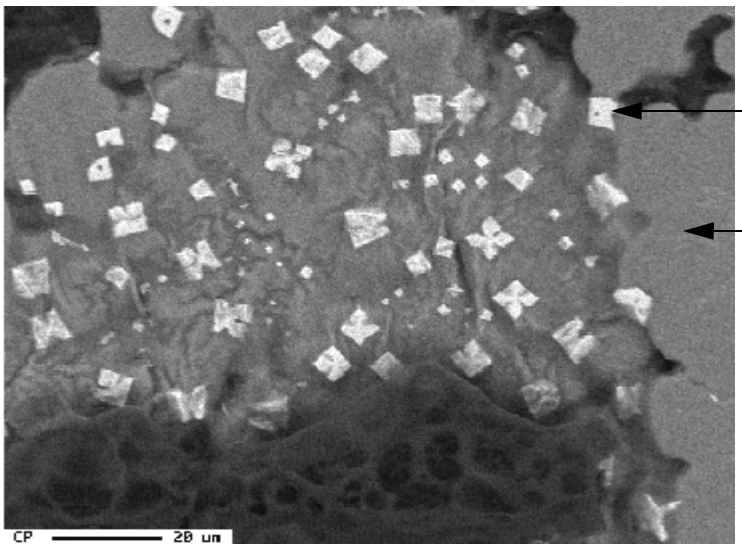

$Al_8(Mn,Ni)_5$ particles

Mg-Al matrix

Figure 9.9: $Al_8(Mn,Ni)_5$ particles identified for experiment at 751.5°C and 10.1 wt.% Al (X750).

9.3 Discussion

On cooling a melt from a higher temperature one may from the solubility data for a line compound determine the ratio of the components in the precipitated phases. The elements will disappear from the melt in a proportion that corresponds to the elements in the precipitated phases. From the slope of the solubility data of various components, composition of the precipitated phases may be determined.

Figure 9.10 gives the solubilities of aluminium and manganese in at.% (calculated from Table 9.1) for various aluminium contents in Mg-Al alloys. It is seen that the lines have a near constant slope, indicating that we have 'line compounds'. The circled points in the following figures are not included for the calculation of slope.

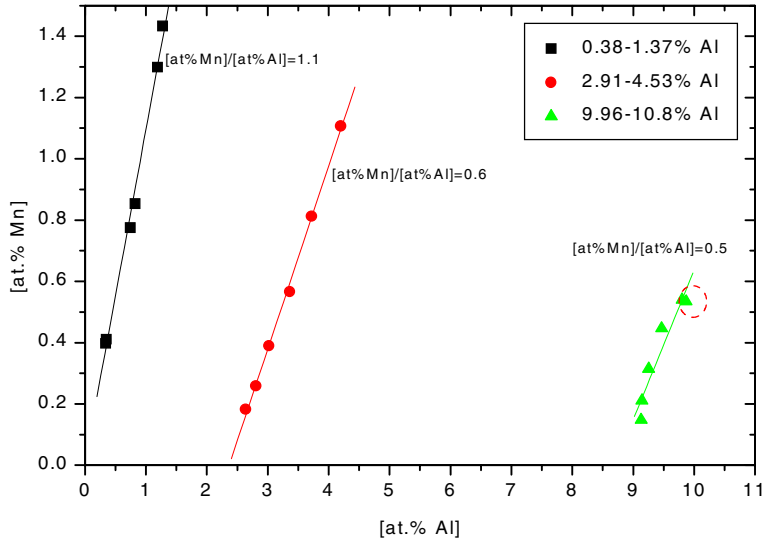

Figure 9.10: Solubilities of Al and Mn in at% for different Mg-Al alloys.

Figure 9.11 gives solubilities of aluminium and nickel in at.% and Figure 9.12 gives the solubilities of manganese and nickel in at.% (calculated from Table 9.1) for various aluminium contents in Mg-Al alloys.

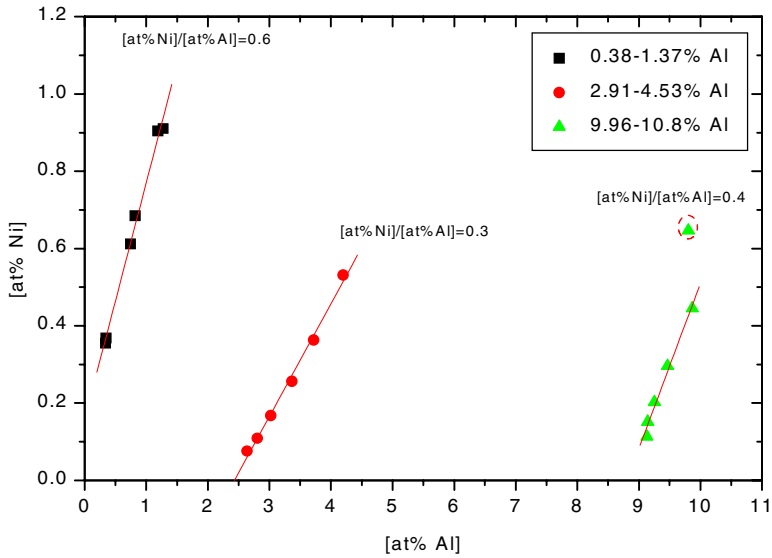

Figure 9.11: Solubilities of Al and Ni in at% for different Mg-Al alloys.

It is seen for instance for low aluminium that at the start of cooling from 898°C the equilibrium nickel content was about 2.13 wt.% (0.91 at.%) and that at 668°C the nickel content was reduced to 0.88 wt.% (0.37 at.%) (Table 9.1).

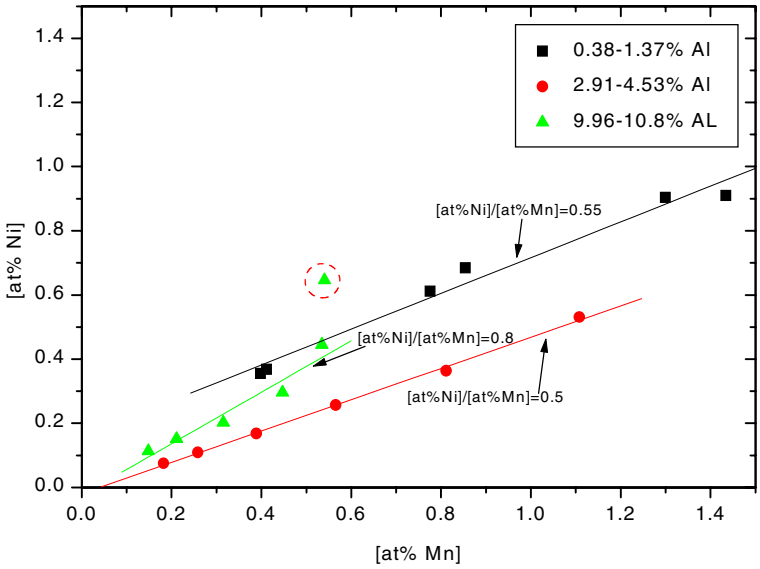

Figure 9.12: Solubilities of Mn and Ni in at% for different Mg-Al alloys.

From Figure 9.10, Figure 9.11, and Figure 9.12 the ratio between Al, Mn, and Ni in the precipitated phases for various aluminium contents is determined from the slopes of the solubility data. The three figures indicate that there are three "line compounds" (Table 9.3) for three Mg-Al alloys.

TABLE 9.3: Ratio between the various components for different Al content in Mg-Al alloys. Estimated "line compounds" are also given.

	(0.38-1.37)% Al	(2.91-4.53)% Al	(9.96-10.8)% Al
Mn/Al ratio	1.1	0.6	0.5
Ni/Al ratio	0.6	0.3	0.4
Ni/Mn ratio	0.55	0.5	0.8
"Line compound"	$AlMn_{1.1}Ni_{0.55}$	$AlMn_{0.6}Ni_{0.3}$	$AlMn_{0.5}Ni_{0.4}$

Dissolution of a $AlMn_{\alpha}Ni_{\beta}$ line compound will be given by:

$$AlMn_{\alpha}Ni_{\beta} = \underline{Al} + \alpha\underline{Mn} + \beta\underline{Ni} \tag{9.1}$$

At equilibrium:

$$-RTK_{AlMn_{\alpha}Ni_{\beta}} = -RT\left(\frac{a_{Al} \times a_{Mn}^{\alpha} \times a_{Ni}^{\beta}}{a_{AlMn_{\alpha}Ni_{\beta}}}\right) = \Delta G^{\circ} \tag{9.2}$$

Using the definition of activity of a component i (equation 6.15), equation 9.2 will be simplified to:

$$R\ln[\%Al][\%Mn]^{\alpha}[\%Ni]^{\beta} = A + \frac{B}{T} \tag{9.3}$$

Where A and B incorporate ΔS° and ΔH° as well activity coefficients f_{Al}, f_{Mn}, and f_{Ni}. The activity of $AlMn_{\alpha}Ni_{\beta}$ line compound is taken to be one. The logarithm of solubility product of data in Table 9.1 is presented in Figure 9.13 as a function of the inverse temperature according to equation 9.3, together with the fitted lines.

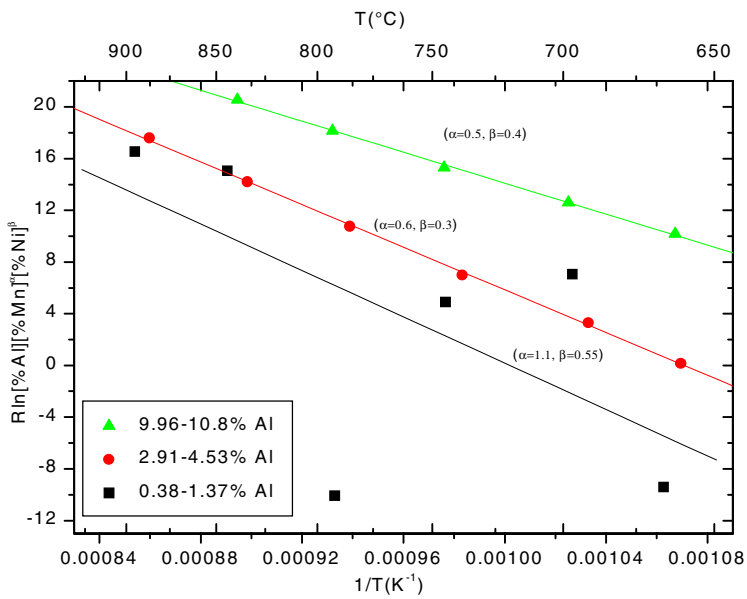

Figure 9.13: The solubility product of the phases given in Table 9.3 versus inverse of temperature in kelvin for various aluminium contents. Note that the inside ticks on the top axis correspond to the outside ticks and labels on the bottom axis and vice versa.

TABLE 9.4: The parameters obtained by fitting straight lines to the experimental solubility data presented in Figure 9.13 (see also Table 9.3).

Alloy	$-B = \Delta H°$	$A = \Delta S°$	R^2
Mg-(0.38-1.37)% Al	89700±56500	89.9±54.3	0.3860
Mg-(2.91-4.53)% Al	82500±1000	88.3±1.0	0.9994
Mg-(9.96-10.8)% Al	59900±1200	74.0±1.2	0.9988

Using the values $\Delta H°$ and $\Delta S°$ from Table 9.4, the nickel content in the melt has been calculated using equation 9.3. Figure 9.14 shows the estimated nickel content and measured nickel content in the melt for medium and high aluminium contents. The nickel values for low aluminium contents are not compared because of large errors in $\Delta H°$ and $\Delta S°$.

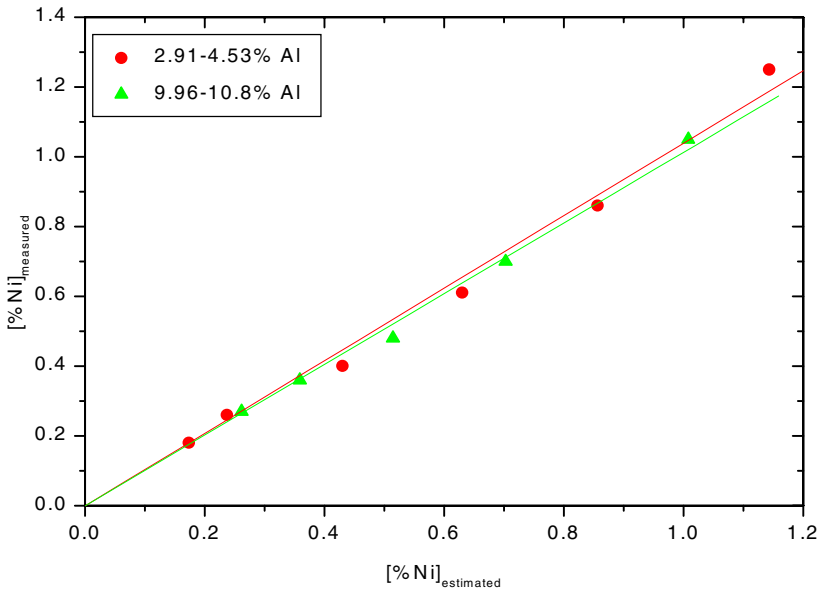

Figure 9.14: Estimated versus measured Ni contents in the melt.

The Gibbs energy of formation of the line compounds given in Table 9.3 will be calculated using the data given in Table 3.1. The calculation for $AlMn_{0.5}Ni_{0.4}$ line com-

pound is given in detail. Similarly the values for $AlMn_{0.6}Ni_{0.3}$ and $AlMn_{1.1}Ni_{0.55}$ have been calculated.

For high aluminium content in Mg-Al alloys.

$\underline{Al} + 0.5\underline{Mn} + 0.4\underline{Ni} = AlMn_{0.5}Ni_{0.4}(s)$	-59900 + 74.0T	(Table 9.4)
$Al(l) = \underline{Al}$	-9866 - 35.3T	(Table 3.1)
$0.5Mn(s) = 0.5\underline{Mn}$	20070 - 24.6T	(Table 3.1)
$0.4Ni(s) = 0.4\underline{Ni}$	-17400 - 8.9T	(Table 3.1)

$$Al(l) + 0.5Mn(s) + 0.4Ni(s) = AlMn_{0.5}Ni_{0.4}(s) \quad -67096 + 5.2T \tag{9.4}$$

For medium aluminium content in Mg-Al alloys

$$Al(l) + 0.6Mn(s) + 0.3Ni(s) = AlMn_{0.6}Ni_{0.3}(s) \quad -81332 + 16.8T \tag{9.5}$$

For low aluminium content in Mg-Al alloys

$$Al(l) + 1.1Mn(s) + 0.55Ni(s) = AlMn_{1.1}Ni_{0.55}(s) \quad -79337 - 11.7T \tag{9.6}$$

In the following the effect of manganese on the solubility of nickel in Mg-Al alloys is discussed.

The solubility of nickel in Mg-Al alloys is estimated using equation (6.1). The parameters *A* and *B* for medium (3.00-3.60%Al) and high (8.80-9.35%Al) aluminium content are taken from Table 6.3. The solubility of nickel in Mg-Al alloys in the presence manganese is estimated using equation 9.3, and the ΔH° and ΔS° for low and high aluminium are taken from Table 9.4.

Figure 9.15 shows a comparison of nickel solubility in Mg-Al alloys with and without manganese. The solubility of nickel in Mg-Al alloys is same as in Mg-Al-Mn alloys for medium aluminium contents. The solubility of nickel in Mg-Al alloys at high aluminium content is increased by manganese addition.

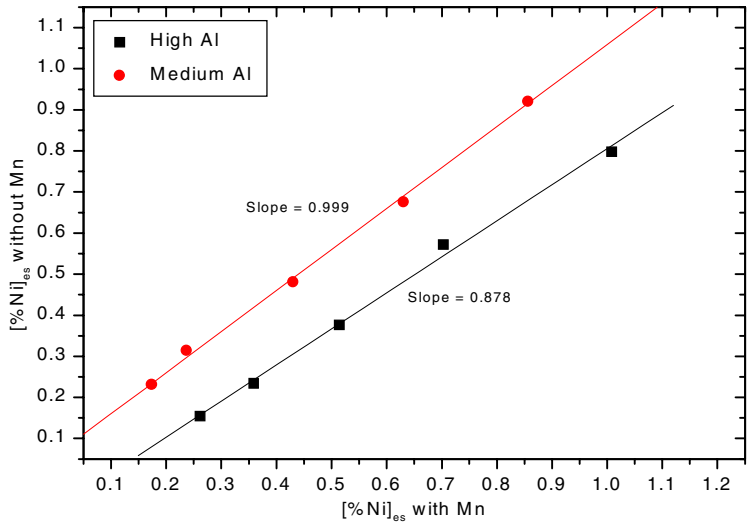

Figure 9.15: Comparison of the Ni solubility in Mg-Al alloys with and without Mn.

9.4 Conclusions

The solubilities of manganese and nickel in Mg-Al alloys has been measured in the temperature range 650-900°C and aluminium content 1-10wt.%. The amount of manganese and nickel was added such that there was an excess of these elements at 900°C. Gibbs energy of formation of the 'line compounds' determined using the solubility data at various aluminium contents in Mg-Al alloys is:

For 9.96-10.8% Al

$Al(l) + 0.5Mn(s) + 0.4Ni(s) = AlMn_{0.5}Ni_{0.4}(s)$, $\Delta G^\circ = -67096 + 5.2T$

For 2.91-4.53% Al

$Al(l) + 0.6Mn(s) + 0.3Ni(s) = AlMn_{0.6}Ni_{0.3}(s)$, $\Delta G^\circ = -81332 + 16.8T$

For 0.38-1.37% Al

$Al(l) + 1.1Mn(s) + 0.55Ni(s) = AlMn_{1.1}Ni_{0.55}(s)$, $\Delta G^\circ = -79337 - 11.7T$

The solubility of nickel is higher in Mg-Al alloys saturated with manganese as compared to pure Mg-Al alloys at high aluminium content.

Chapter 10

Mg-Al-Ni-Fe-X system in iron capsule

Compared to Chapter 7, the system is expanded to include aluminium. Thus the possibility of precipitating nickel in magnesium-aluminium alloys by using an element X is studied. Here again X is one of the elements; Zr, Mo, Mn, V, Hf, Ti or Ta as proposed by Simensen and Kolby (1995). Two more elements, Cr and RE (Rare earth), have been added to the above element list to remove nickel from molten Mg-Al alloys. The criteria for selecting the element X are mentioned in Chapter 7. Also some samples are treated in iron capsules without an addition of element X.

10.1 Experimental set-up and procedure

High purity magnesium (99.99%) granules and high purity aluminium (99.999%) were used to make a Mg-5%Al master alloy. Pure nickel powder (99.5%) with particle size less than 10 microns was added to the above master alloy. The supplier of the materials used is given in Chapter 4 (Table 4.1) and the chemical compositions are given in Appendix A.

The elements magnesium, aluminium and nickel were mixed to obtain a master alloy with a final composition of Mg-5%Al-200ppm Ni. The mixture was melted at 750°C in an iron (ST37) crucible. Three separate mixtures were made in separate crucibles under the same conditions and cast separately in copper moulds to get cylindrical samples. Detailed descriptions of melting and casting are given in Chapter 4.

One sample from each casting was analysed by ICP-AES (Inductively Coupled Plasma- Atomic Emission Spectroscopy) in order to determine the start concentration of nickel. The results are shown in Table 10.1.

TABLE 10.1: ICP-AES analysis of three different master alloys.

	Aluminium [wt.%]	Iron (ppm)	Nickel (ppm)
Casting 1	4.7	75	64
Casting 2	5.4	71	97
Casting 3	4.8	79	65

The nickel contents in the above samples were considered to be low as it was attempted to add approximately 200 ppm nickel, and therefore new samples were made with higher nickel content. The materials and the procedure used for sample preparation are as described earlier. This time nickel powder corresponding to 400 ppm was added to the Mg-5%Al master alloy. The ICP-AES analysis of four different samples from the same master alloy is given in Table 10.2.

TABLE 10.2: ICP-AES analysis of samples from a master alloy with higher Ni content prepared at 750°C.

Sample (casting 4)	Aluminium [wt.%]	Iron [wt.%]	Nickel (ppm)
1	5.17	1.48	360
2	5.05	0.11	330
3	5.12	0.31	350
4	5.18	0.039	340

Solubility of iron in pure magnesium is below 0.05 wt.% at 750°C (Nayeb-Hashemi and Clark 1988, pp. 118-121). So sample number 1 and sample numbers 2 and 3 are probably contaminated with iron. The average start nickel content for casting 4 is 345 ppm.

Cylindrical samples from casting 2, 3 and 4 were machined so that they fit into iron capsules along with element X. The figures of capsule and the welding apparatus and the welding encapsulation procedure are given in detail in Chapter 4. The geometries

and the masses of elements X added to the master alloys (Table 10.1 and Table 10.2) are given in Table 10.3.

TABLE 10.3: The shape and the masses of elements X added with the master alloys in iron capsules for removal of nickel.

Sample No.	Element X	Mass X (g)	Mass Mg (g)
410	None	-	8.15
418	Cr pieces	1.05	8.70
251	Hf thread	0.24	6.43
261	Hf thread	0.49	6.60
361	Hf thread	0.49	7.42
312	Mn pieces	1.20	7.35
222	Mn pieces	0.88	7.86
252	Mn pieces	2.08	8.45
422	Mn pieces	0.97	9.09
422’	Mn pieces	0.90	9.15
313	Mo foil	3.44	7.81
233	Mo foil	3.89	6.92
243	Mo foil	3.18	6.33
419	RE pieces	1.07	8.38
314	Ta foil	0.67	8.15
224	Ta foil	0.79	7.65
254	Ta foil	0.84	8.49
424	Ta foil	1.11	8.92
345	Ti foil	0.97	8.36
225	Ti foil	0.85	7.26
235	Ti foil	0.83	8.01

TABLE 10.3: The shape and the masses of elements X added with the master alloys in iron capsules for removal of nickel.

Sample No.	Element X	Mass X (g)	Mass Mg (g)
425	Ti foil	0.33	8.75
316	V thread	0.10	8.30
236	V thread	0.07	8.62
246	V thread	0.09	8.58
416	V thread	0.12	8.61
347	Zr foil	0.26	8.42
227	Zr foil	0.28	8.66
237	Zr foil	0.29	8.63

The encapsulated samples were heat-treated in a transparent cylindrical furnace (Figure 4.2) in an argon atmosphere. The samples were treated at 670°C and 800°C, and kept at the specific temperature for 48 hours or 100 hours. The samples were water-quenched to preserve the conditions at the treatment temperatures.

All the samples from casting 2 and 3 after heat treatment were analysed using X-ray diffraction. Samples, which showed a considerable reduction of nickel content, were subsequently analysed using ICP-AES technique for higher accuracy. The samples from casting 4 were analysed by ICP-AES after treatment.

10.2 Results

ICP-AES analysis results will be used for plotting graphs, but X-ray analysis results will be used where ICP-AES analysis results are not available. X-ray analysis and ICP-AES analysis of sample 243 give diverging values for the nickel content. The X-ray analysis seems to be more reasonable if we compare with sample 233 and 313, and therefore the X-ray result will only be used for sample 243.

All the concentrations are in mass percent, both in melt [wt.%] and in particles (wt.%) unless specified otherwise in the following tables.

10.2.1 Sample 410

Sample 410 was treated in an iron capsule without any element X for about 100 hours at 670°C and quenched in water. The initial content of nickel was 340 ppm. After the treatment ICP-AES analysis of the sample shows a reduction of 74% nickel (Table 10.4).

TABLE 10.4: ICP-AES analysis of sample 410 with only Mg-Al-Fe-Ni.

Sample no.	Temp (°C) / Time (hrs.)	End X	Start Fe/ End Fe [ppm]	Start Ni [ppm]	End Ni [ppm]	Phase	Ni in phase (wt.%)
410	670/100	-	390/-	345	89-92	FeAl	~5-6

Microprobe analyses of the sample indicates the presence of FeAl particles (Figure 10.13) with approximate 32 wt.% Al also containing 5-6 wt.% nickel. The size of the particles is approximately 10 µm and Figure 10.1 shows the FeAl particles identified in sample 410.

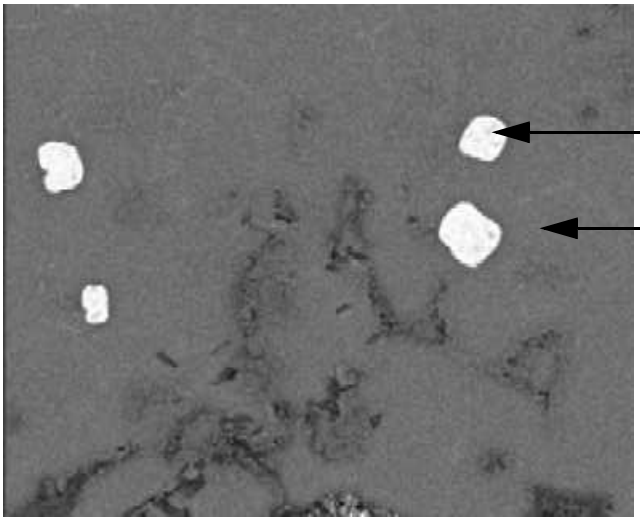

Figure 10.1: FeAl particles in sample 410 containing 5-6 wt.% nickel (X1000).

10.2.2 Samples treated with chromium pieces

Sample no. 418 was treated at 670°C for 100 hours with chromium pieces. The initial nickel content was 340 ppm. ICP-AES analysis of the sample gave a reduction of 83% nickel (Table 10.5).

TABLE 10.5: ICP-AES analysis of sample 418 after the treatment with Cr pieces.

Sample no.	Temp (^oC)/ Time (hrs.)	End X Cr [ppm]	Start Fe/ End Fe [ppm]	Start Ni/ End Ni [ppm]	Phase	Ni in phase (wt.%)	Cr in phase (wt.%)
418	670/100	<2	390/-	345/ 58-62	FeAl, $AlCr_2$	~1-2	8-10 ~80

Microprobe analysis of the sample indicates that aluminium reacts with the chromium surface. Aluminium and iron in molten magnesium reacts with solid chromium and results in the formation of $AlCr_2$ phase also containing 5-6 wt.% iron (Figure 10.2).

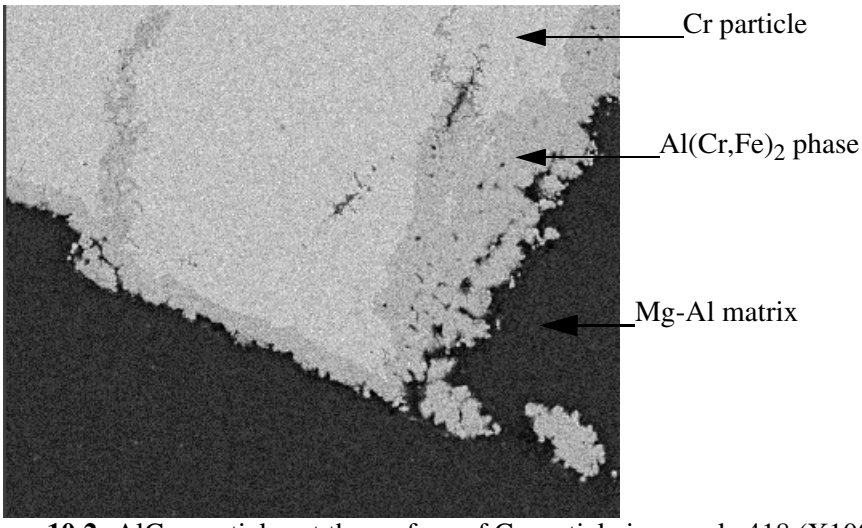

Figure 10.2: $AlCr_2$ particles at the surface of Cr particle in sample 418 (X1000).

Some FeAl particles were identified near the bottom of the sample. Figure 10.3 shows the FeAl particle containing 8-10 wt.% chromium and 1-2 wt.% nickel.

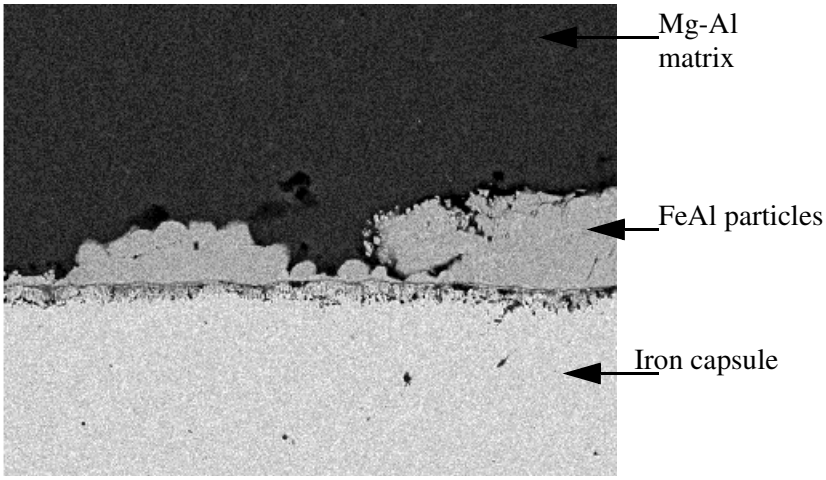

Figure 10.3: FeAl particles containing Cr and Ni in sample 418 (X1000).

10.2.3 Samples treated with hafnium wire

Two samples, 261 and 361, were treated with hafnium wire at 800°C and one sample, 251, was treated at 670°C for 48 hours. The initial content of nickel in samples 251 and 261 were 97 ppm and in 361 was 65 ppm. Nickel content in sample 261, 361, and 251 reduced by 47%, 26%, and 36% respectively (Table 10.6).

TABLE 10.6: ICP-AES and X-ray analysis of the samples after treatment with Hf.

Sample no.	Temp (^{o}C)/ Time (hrs.)	End X Hf [ppm]	Start Fe/ End Fe [ppm]	Start Ni/ End Ni [ppm]	Phase	Ni in phase (wt.%)	Hf in phase (wt.%)
261	800/48	(0.9%)[a]	71/ (0.5%) 884	97/ (290) 51			
361	800/48	(<20)	79/ (0.10%)	65/ (48)	FeAl	~1	-
251	670/48	(30)	71/ (105) 257	97/ (63) 62	$FeAl_2$	~1.3	4

a. Numbers in the parentheses are X-ray analysis and others are ICP-AES analysis results.

SEM analysis of samples indicated the presence of two different types of particles. The compositions of the particles correspond to $FeAl_2$ and FeAl phases (Figure 10.13). $FeAl_2$ particles were identified in sample 251 and FeAl particles were identified in sample 361. Some of these Fe-Al particles contained more than 1 wt.% nickel. The composition of the big particle ($FeAl_2$) in Figure 10.4 is 48 wt.% Fe, 49 wt.% Al and 1.3 wt.% Ni.

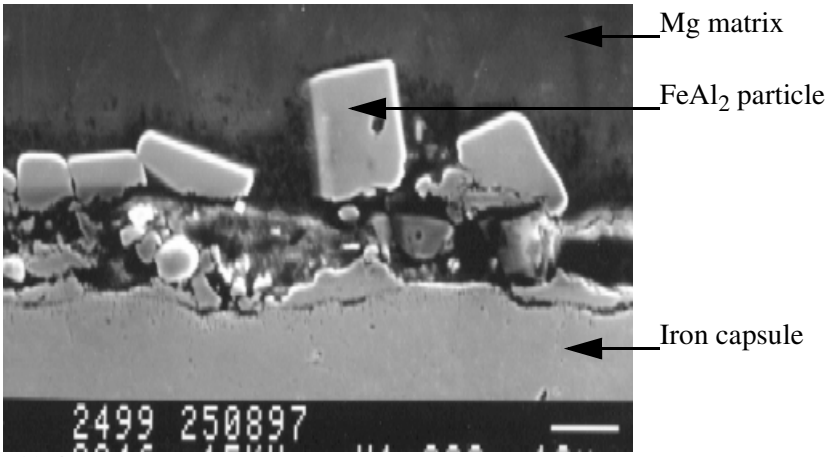

Figure 10.4: $FeAl_2$ particles in sample 251 treated with Hf wire (X1000).

10.2.4 Samples treated with manganese pieces

Samples number 312 and 222 were treated at 800°C. Start nickel content of sample 312 was 65 ppm and sample 222 was 97 ppm. X-ray and ICP-AES results showed a 17% and 27% reduction of nickel content after the treatment. Sample 252, 422 and 422' were treated at 670°C and gave a 79%, 83% and 80% reduction in the nickel content respectively (Table 10.7). The start content of nickel in sample 252 was 97 ppm, and 422 and 422' was 345. The samples 312, 222, and 252 were treated for 48 hours and samples 422, and 422' were treated for 100 hours.

TABLE 10.7: ICP-AES and X-ray analysis of the samples after treatment with Mn.

Sample no.	Temp. (°C)/ Time (hrs.)	End X Mn [%]	Start Fe/ End Fe [ppm]	Start Ni/ End Ni [ppm]	Phase	Ni in phase (wt.%)	Mn in phase (wt.%)
422	670±0.5 /100	0.10	390/-	345/ 55-59			

TABLE 10.7: ICP-AES and X-ray analysis of the samples after treatment with Mn.

Sample no.	Temp. (°C)/ Time (hrs.)	End X Mn [%]	Start Fe/ End Fe [ppm]	Start Ni/ End Ni [ppm]	Phase	Ni in phase (wt.%)	Mn in phase (wt.%)
422'	670±0.5 /100	0.07	390/-	345/ 67-71	FeAl	~2-5	~3
312	798±1/ 48	(0.91)[a]	79/ (350)	65/ (54)			
222	804±1/ 48	(1.8)	71/ (140)	97/ (71)			
252	676±0.5 /48	(0.36)	71/ (25) 15	97/ (35) 20	$Al_8(Mn,Fe)_5$	~0.3-0.7	~35

a. Numbers in the parentheses are X-ray analysis and others are ICP-AES analysis results.

Sample 252, 422 and 422' were analysed in microprobe. Figure 10.5 shows the shape and the size of the particles identified in sample 252. The composition of the particles corresponds to $Al_8(Mn,Fe)_5$ phase (Massalski et al. 1996) also containing small amounts of nickel. Due to the similarity between Mn and Fe, the phase Al_8Mn_5 may also contain some iron (Holta et al. 1996).

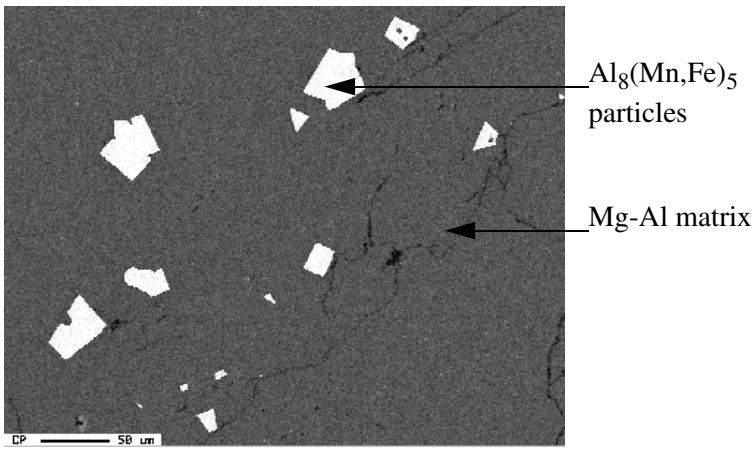

Figure 10.5: $Al_8(Mn,Fe)_5$ particles in sample 252 treated with Mn pieces (X250).

In sample 422', FeAl particles were identified also containing manganese and nickel. The size of the particles is around 10 µm and contain 2-5 wt.% nickel and 3-4 wt.% manganese. Shape of particles are similar to the particles in Figure 10.4.

10.2.5 Samples treated with molybdenum foil

Sample 243 and sample 313 with a start nickel content of 97 ppm and 65 ppm were treated at 800°C. X-ray and ICP-AES results showed about 54% and 22% reduction in nickel content. Sample number 233 with a start nickel content 97 ppm was treated at 670°C and showed a nickel reduction of 26%. All the three samples were treated for 48 hours (Table 10.8).

TABLE 10.8: ICP-AES and X-ray analysis of the samples after treatment with Mo.

Sample no.	Temp. (°C)/ Time (hrs.)	End X Mo [ppm]	Start Fe/ End Fe [ppm]	Start Ni/ End Ni [ppm]	Phase
313	798±1/48	(<20)[a]	79/(360)	65/(51)	
243	804±1/48	(2.1%)	71/(0.67%) 1.7%	97/(45),<5	
233	670±0.5/48	(<20)	71/(86)	97/(72)	

a. Numbers in the parentheses are X-ray analysis and others are ICP-AES analysis results.

Sample number 243 was further analysed in microprobe to identify the precipitated phases. No particle containing Al, Fe, Mo or Ni was identified in sample 243.

10.2.6 Sample treated with rare earths

Sample 419, with a start nickel content of 345 ppm, was treated at 670°C for about 100 hours. ICP-AES analysis of the sample gave a nickel removal of 45% (Table 10.9).

TABLE 10.9: ICP-AES analysis of sample 419 after treatment with RE.

Sample no.	Temp. (^{o}C)/ Time (hrs.)	End X RE	Start Fe/ End Fe [ppm]	Start Ni/ End Ni [ppm]	Phase	Ni in phase (wt.%)	RE in phase (wt.%)
419	670±0.5 /100		390/-	345/ 189-193	FeAl	~0.5	Ce-12% La-4%

The sample was further analysed using microprobe for identifying the precipitated phases. Because of the non-availability of the standards for Nd, Pr, Sm and B (boron) for microprobe analysis these elements could not be identified in the precipitated phases. Figure 10.6 indicates the morphology and size of the particles identified in sample 419. Small particles at the bottom contain mainly 31 wt.% Mg, 32 wt.% La, 19 wt.% Ce and 10 wt.% Al which sum up to 92%. The rest may be from Nd, Pr, Sm and/or B and could not be identified due to the non-availability of standards in microprobe. Large particles in Figure 10.6 are in the range 20-100 µm and have different composition from the small particles. The large particles have a composition of 20 wt.% La, 33 wt.% Ce and 24 wt.% Al.

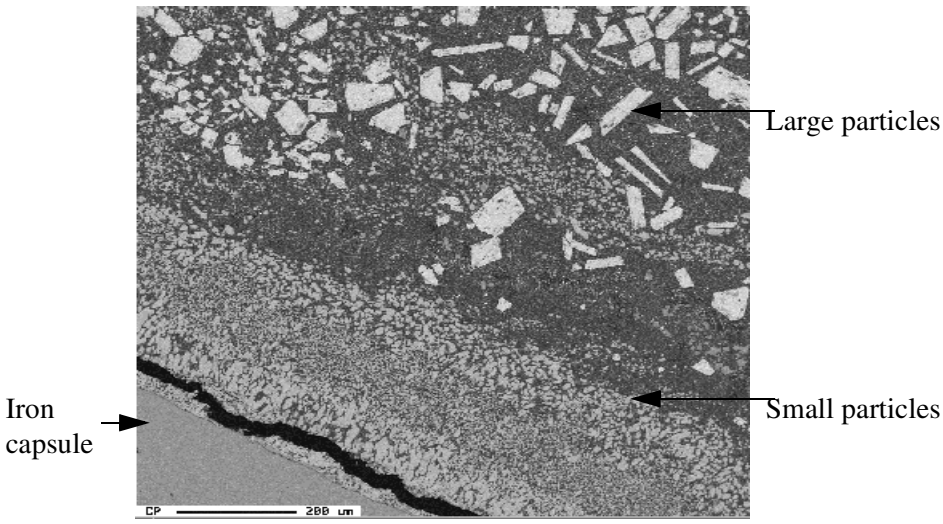

Figure 10.6: Particles in sample 419 treated with RE (X100).

Figure 10.7 shows the large particles along with some grey particles in the range 10-20 µm. These grey particles are FeAl particles with 0.5 wt.% nickel also containing 12 wt.% Ce and 4 wt.% La. The grey phase inside the large particle has different

composition from the grey particles near the big particle. The grey phase inside the big particle has 31 wt.% Mg, 30 wt.% La, 9 wt.% Al and 20 wt.% Ce.

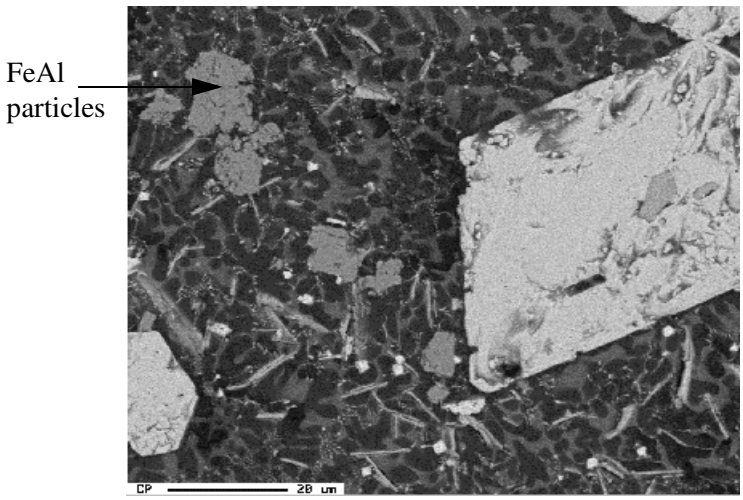

Figure 10.7: Large particle along with small grey particles in sample 419 treated with (X1000).

10.2.7 Samples treated with tantalum foil

Two samples, 314 and 224, were treated with tantalum foil at 800°C for 48 hours. Start nickel content in 314 and 224 was 65 ppm and 97 ppm, respectively. Sample 254 and 424 with start nickel content 97 ppm and 345 ppm were treated at 670°C for 48 hours and 100 hours respectively. X-ray and ICP-AES results show a reduction of 68%, 76%, 69% and 57% respectively, in the nickel content (Table 10.10).

TABLE 10.10: ICP-AES and X-ray analysis of the samples after treatment with Ta.

Sample no.	Temp. (^{o}C)/ Time (hrs.)	End X Ta [ppm]	Start Fe/ End Fe [ppm]	Start Ni/ End Ni [ppm]	Phase	Ni in phase (wt.%)	Ta in phase (wt.%)
314	798±1/ 48	(<20)[a]	79/(370) 321	65/(29) 21			
224	804±1/ 48	(<20)	71/(320) 410	97/(43) 23			

TABLE 10.10: ICP-AES and X-ray analysis of the samples after treatment with Ta.

Sample no.	Temp. (°C)/ Time (hrs.)	End X Ta [ppm]	Start Fe/ End Fe [ppm]	Start Ni/ End Ni [ppm]	Phase	Ni in phase (wt.%)	Ta in phase (wt.%)
254	676±0.5 /48	(<20)	71/(76) 130	97/(54) 30	FeAl	1-2	1.5
424	670±0.5 /100	<2	390/-	345/ 148-152	FeAl	5	-

a. Numbers in the parentheses are X-ray analysis and others are ICP-AES analysis results.

SEM analysis of particles in the samples indicates the formation of a FeAl phase (Figure 10.13) that contains up to 1.9 wt.% nickel. Some of the FeAl particles also showed the presence of tantalum. The composition of the big particle in Figure 10.8 is 62 wt.% Fe, 35 wt.% Al, 1.9 wt.% Ni and 1.5 wt.% Ta.

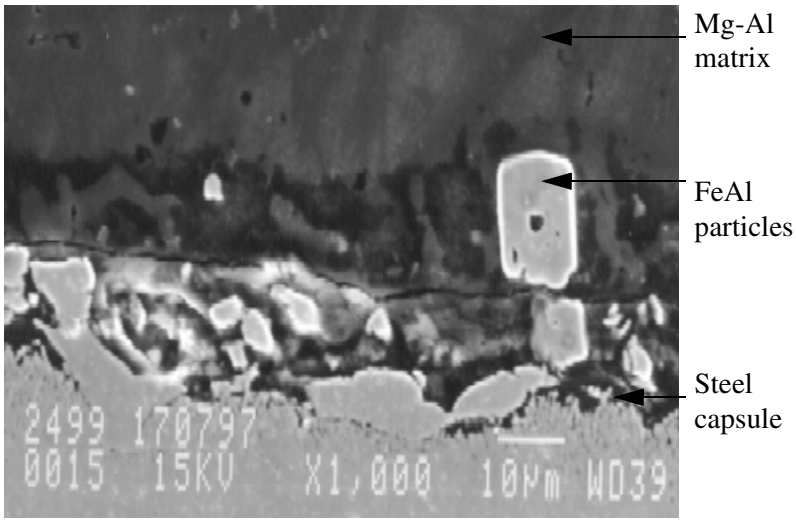

Figure 10.8: Sample 254 treated with Ta foil (X1000).

Sample 424 was analysed using the microprobe. Small FeAl particles in the range 5-8 µm were identified in sample 424 containing up to 5 wt.% nickel. No tantalum was indicated in the particles.

10.2.8 Samples treated with titanium foil

Samples number 225 and 345 with a start nickel content of 97 ppm and 65 ppm were treated at 804°C for 48 hours. X-ray and ICP-AES analysis showed a reduction of about 76% and 26% nickel, respectively. Sample numbers 235 and 425 with a start nickel content 97 ppm and 345 ppm were treated at 670°C for 48 hours and 100 hours and gave a reduction of 51% and 75% nickel (Table 10.11).

TABLE 10.11: ICP-AES and X-ray analysis of the samples treated with a Ti foil.

Sample no.	Temp. (^{o}C)/ Time (hrs.)	End X Ti foil [ppm]	Start Fe/ End Fe [ppm]	Start Ni/ End Ni [ppm]	Phase	Ni in phase (wt.%)	Ti in phase (wt.%)
345	804±1/ 48	(72)[a]	79/(360)	65/(48)			
225	804±1/ 48	(120)	71/(170) 235	97/(23) 14	FeAl	~0.1-0.2	~3-5
235	670±0.5 /48	(<20)	71/(76) 63	97/(47) 31			
425	670±0.5 /100	78-82	390/-	345/85-89	FeAl	~5	-

a. Numbers in the parentheses are X-ray analysis and others are ICP-AES analysis results.

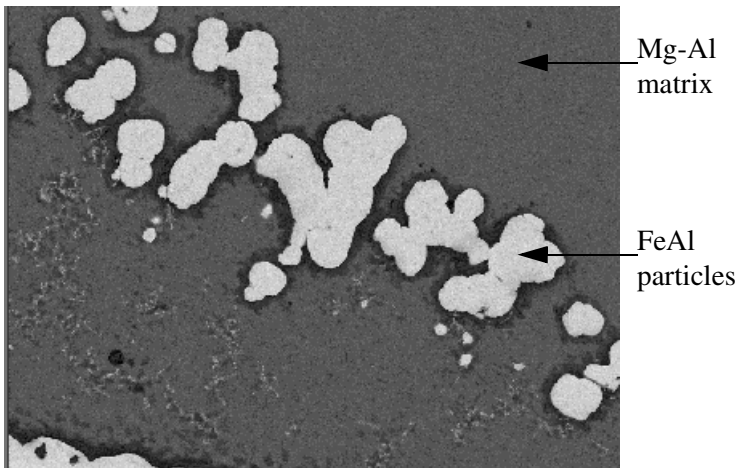

Figure 10.9: FeAl particles containing Ti and Ni in sample 225 (X500).

Sample numbers 225, 235 and 425 were analysed using the microprobe to identify the precipitated phases. The particles observed in sample 225 are shown in Figure 10.9. Typical composition of the particles is 28 wt.% Al, 66 wt.% Fe also containing titanium and very small amounts of nickel. The composition of the particles corresponds to the FeAl phase (Figure 10.13).

FeAl particles were also identified in sample 425 containing up to 5 wt.% nickel. Size of the particles is about 20 µm and no titanium is identified in the particles.

10.2.9 Samples treated with vanadium wire

X-ray and ICP-AES analysis of two samples, 316 and 246 with a start nickel content 65 ppm and 97 ppm, treated with vanadium wire showed a reduction of nickel content by 54% and 71%, respectively, treated at 798°C and 804°C for 48 hours. Sample 236 and 416 with start nickel content 97 ppm and 345 ppm, were treated at 670°C for 48 hours and 100 hours, respectively, and showed a reduction of about 63% and 80% in nickel content (Table 10.12).

TABLE 10.12: ICP-AES and X-ray analysis of the samples after treatment with V wire.

Sample no.	Temp. (°C)/ Time (hrs.)	End X V wire [ppm]	Start Fe/ End Fe [ppm]	Start Ni/ End Ni [ppm]	Phase	Ni in phase (wt.%)	V in phase (wt.%)
316	798±1/ 48	(<20)[a]	79/(300) 309	65/(41) 30	FeAl	~0.6	0.6
246	804±1/ 48	(<20)	71/(330) 300	97/(56) 28	FeAl	~0.3-0.7	2
236	670±0.5 /48	(<20)	71/(72) 65	97/(36) 22	FeAl	~0.3-0.9	0.2
416	670±0.5 /100	3-4	390/-	345/ 68-72	FeAlV	~0.05	24

a. Numbers in the parentheses are X-ray analysis and others are ICP-AES analysis results.

In all of the samples FeAl phase was identified. Some of the FeAl particles also contained a little more than 1 wt.% nickel. The shape and size of the particles are similar to those in Figure 10.4 and Figure 10.8.

10.2.10 Samples treated with zirconium foil

Samples number 347 and 227 with start nickel content 65 ppm and 97 ppm were treated at 804°C for 48 hours. X-ray and ICP-AES analysis (Table 10.13) gave a nickel reduction of about 38% and 51%. Sample number 237 with a start nickel content 97 ppm was treated at 670°C and gave a nickel reduction of 27%.

TABLE 10.13: ICP-AES and X-ray analysis of the samples after treatment with Zr foil.

Sample no.	Temp. (°C)/ Time (hrs.)	End X Zr foil [wt.%]	Start Fe/ End Fe [ppm]	Start Ni/ End Ni [ppm]	Phase	Ni in phase (wt.%)	Zr in phase (wt.%)
347	804±2/ 48	(0.32%)[a]	79/ (0.10%) 0.86%	65/(40) 365			
227	804±1/ 48	(0.12%)	71/ (0.10%) 900	97/ (48)91	Al-Fe-Zr particles	~0.1-0.9	15-53
237	670±0.5 /48	(2.9%)	71/ (0.45%)	97/(71)			

a. Numbers in the parentheses are X-ray analysis and others are ICP-AES analysis results.

Sample 227 was analysed in the microprobe to identify the precipitated phases containing nickel. Particles with an approximate size 20 µm were observed to have three contrasts (Figure 10.10). The aluminium content in all the three phases were in the range of 30 wt.% to 33 wt.%. The darkest phase contained the highest iron content at about 53 wt.% and the least zirconium content at 15 wt.%. Medium dark and lighter phases contain about 31 wt.% Fe, 38 wt.% Zr and 20 wt.% Fe, 53 wt.% Zr, respectively. These particles also contain small amounts of nickel.

ICP-AES analysis of the samples after treatment with X at 670°C and 800°C for 48 and 100 hours gave a reduction of nickel content in the range 22-86%. Figure 10.11, and Figure 10.12 show a comparison of start nickel versus end nickel after treatment

with various elements X at 670°C, and 800°C, respectively. Only ICP-AES analysis results are used, X-ray analysis results are used where ICP-AES analysis results are not available.

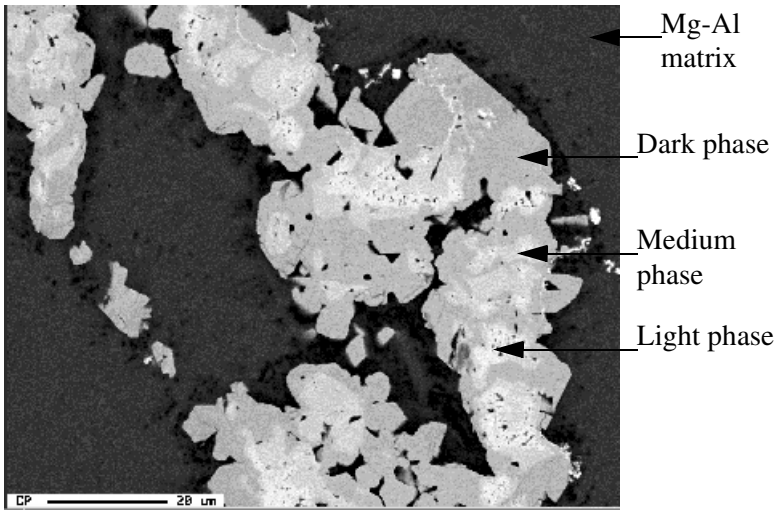

Figure 10.10: Particles containing Al, Fe and Zr in sample 227 (X1000).

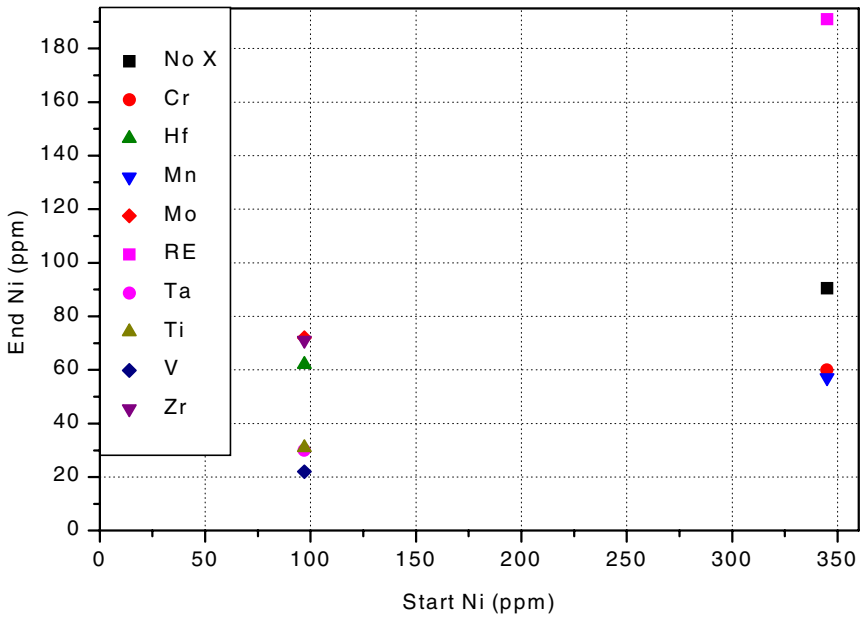

Figure 10.11: Comparison of start nickel versus end nickel for different X at 670°C.

Figure 10.11 shows that sample 410 gave a removal of nickel to 74% without any use of element X. FeAl particles were identified in sample 410 containing 5-6 wt.% Ni. At 670°C the samples treated with Cr, Mn, Ti, Ta and V also gave best removal of nickel.

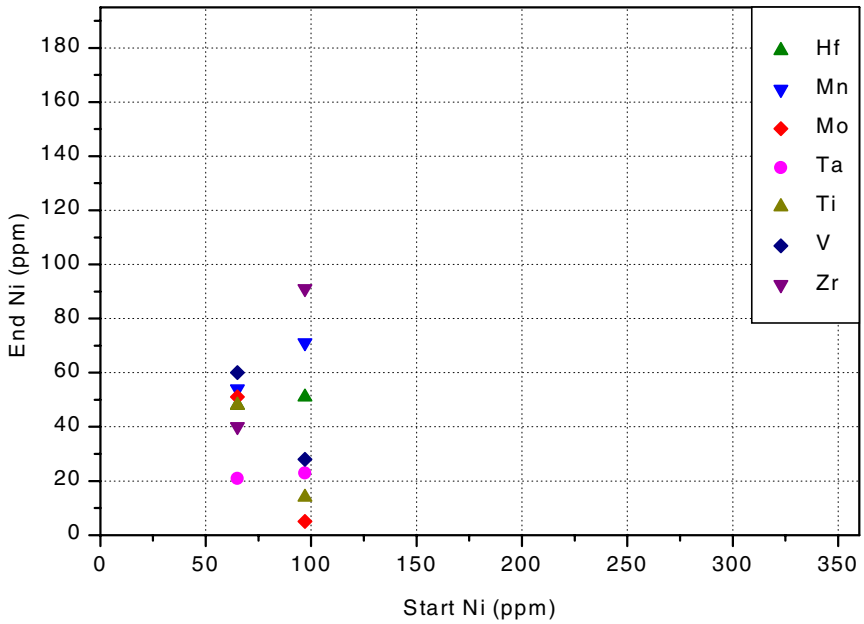

Figure 10.12: Comparison of start nickel versus end nickel for different X at 800°C.

At 800°C Mo, Ti, Ta and V gave the best reduction (Figure 10.12).

SEM and Microprobe analysis of the samples indicated the presence of Al-Fe phases containing small amounts of nickel. The presence of $Al_8(Mn,Fe)_5$ phase also containing small amounts of Ni in the sample with X = Mn indicates that Fe and Ni can be removed by the phase Al_8Mn_5. Microprobe analysis of the sample containing Cr also gave a reduction of nickel to 84%. FeAl particles were identified containing 8-10 wt.% Cr and 1-2 wt.% Ni.

The results indicate that iron and manganese play a major role in removing nickel from Mg-Al alloy. Figure 10.13 shows various phases that aluminium forms with iron. AlFe is a stable phase with a concentration range of approximately 24-51 at.% Al at 700°C

As AlFe is the dominating phase in most of the samples, eight more samples were treated in iron capsules without an addition of element X. The samples were kept at

700°C for 29 days and 30 days respectively, and the contents of aluminium and nickel in the walls of iron capsule were determined using the microprobe. Table 10.14 shows the start and end values in the melt for aluminium, iron, and nickel, respectively, along with the nickel content in the AlFe particles treated at 700°C for 29 days and 30 days. In addition the samples in which particles containing nickel were identified in the previous tables are summarised in Table 10.14

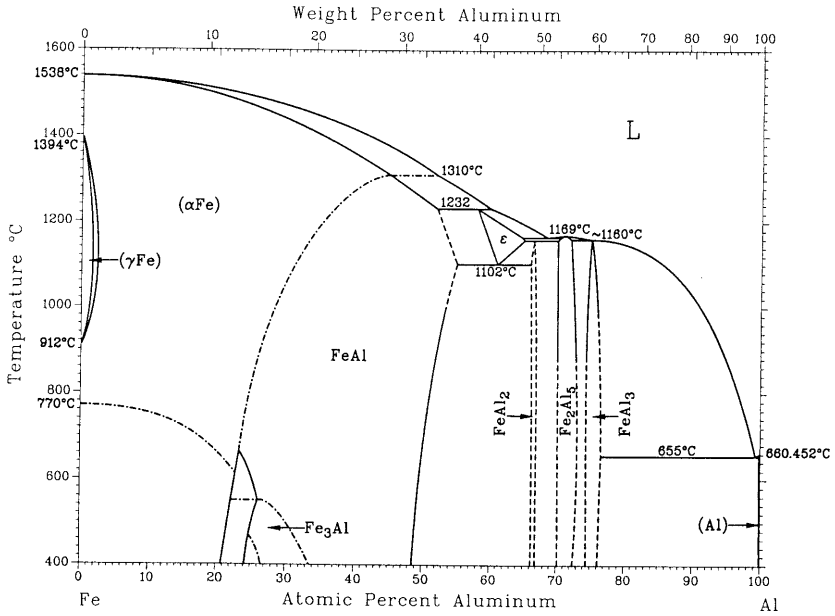

Figure 10.13: AlFe phase diagram (Massalski 1990, p. 148)

For the samples analysed by ICP-AES and microprobe the relative accuracies are better than ±10% at these concentration levels.

TABLE 10.14: Mg-Al-Ni samples treated in iron capsules at 700°C for 29 and 30 days. The samples from the previous tables in which particles containing Ni were identified are also given. Notice that samples 418, 361, 251, 422', 252, 419, 254, 424, 225, 425, 316, 246, 236, 416, and 227 were treated with an additional element X.

Sample no./ (Temp.°C)	Time (hrs.)	Start Al/ End Al [wt.%]	Start Fe/ End Fe [ppm]	Start Ni/ End Ni [ppm]	Phase (at.%Al/ at.%Fe)	Ni in phase (wt.%)
9A/ (700)	29 days	5.66/ 2.68	410/ 128	915/ 147	AlFe (1.0)	2.3
9B/ (700)	29 days	5.69/ 2.67	280/ 980	917/ 100	AlFe (1.0)	2.5
9C/ (700)	29 days	5.65/ 1.76	400/ 139	2000/ 138	AlFe (1.1)	5.7
9D/ (700)	29 days	5.67/ 2.02	460/ 24	2000/ 2.80wt.%	AlFe (1.1)	5.9
13A/ (700)	30 days	3.00/ 0.526	-/1160	340/200	AlFe (0.53)	2.4
13B/ (700)	30 days	3.00/ 0.320	-/660	300/160	AlFe (0.45)	3.5
13C/ (700)	30 days	3.00/ 0.469	-/2030	340/150	AlFe (0.52)	2.0
13D/ (700)	30 days	3.00/ 0.368	-/550	400/230	AlFe (0.47)	0.7
410/ (670)	100	5.11/3.91	390/-	345/90	AlFe (1.1)	6.2
418Cr/ (670)	100	5.11/3.7	390/-	345/60	AlFe (1.2)	1.8
361Hf/ (800)	48	4.8/1.9	79/0.10%	65/48	AlFe (1.1)	1.1
251Hf/ (670)	48	5.4/4.4	71/257	97/62	Al_2Fe (2.1)	1.3
422'Mn/ (676)	100	5.11/3.51	390/-	345/69	AlFe (1.2)	5.4
252Mn/ (676)	48	5.4/3.6	71/15	97/20	$Al_8(Mn,Fe)_5$	0.7
419RE/ (670)	100	5.11/2.5	390/-	345/191	(Fe,Al,Ce,La)	0.5

TABLE 10.14: Mg-Al-Ni samples treated in iron capsules at 700°C for 29 and 30 days. The samples from the previous tables in which particles containing Ni were identified are also given. Notice that samples 418, 361, 251, 422', 252, 419, 254, 424, 225, 425, 316, 246, 236, 416, and 227 were treated with an additional element X.

Sample no./ (Temp.°C)	Time (hrs.)	Start Al/ End Al [wt.%]	Start Fe/ End Fe [ppm]	Start Ni/ End Ni [ppm]	Phase (at.%Al/ at.%Fe)	Ni in phase (wt.%)
254Ta/ (676)	48	5.4/4.1	71/130	97/30	AlFe (1.1)	1.9
424Ta/ (670)	100	5.11/3.59	390/-	345/150	AlFe (1.2)	4.9
225Ti/ (804)	48	5.4/2.5	71/235	97/14	AlFe (0.87)	0.2
425Ti/ (670)	100	5.11/3.66	390/-	345/87	AlFe (1.2)	5.3
316V/ (798)	48	4.8/1.9	79/309	65/30	AlFe (0.87)	0.6
246V/ (804)	48	5.4/2.6	71/300	97/28	AlFe (0.88)	0.7
236V/ (670)	48	5.4/4.3	71/65	97/22	AlFe (1.2)	0.9
416V/ (670)	100	5.11/3.97	390/-	345/72	AlFeV	0.05
227Zr/ (804)	48	5.4/2.5	71/900	97/91	AlFeZr	0.9

In the following figures the data from Table 10.14 will be used. Figure 10.14 shows the nickel content in all the phases identified versus nickel in the melt. The numbers in the parentheses are the end aluminium [wt.%] in the melt. The end aluminium values are rounded off to two digits in Figure 10.14 and Figure 10.15. The data from sample 9D is not included in the figure as the end nickel content is unreasonably high.

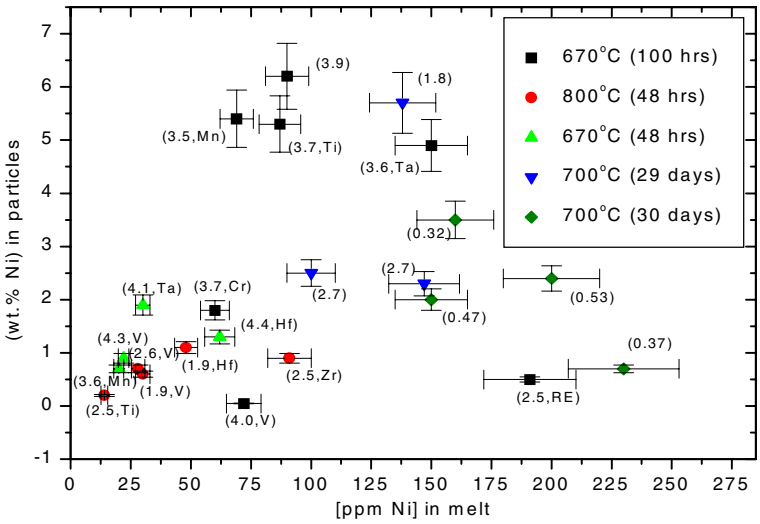

Figure 10.14: (wt.% Ni) in the particles versus ppm nickel in the melt at various temperatures and holding time for various X and various intermetallic phases. The numbers in the parentheses are final [%Al] in the melt. The additional element X used for the treatment are also given in parentheses (see Table 10.14).

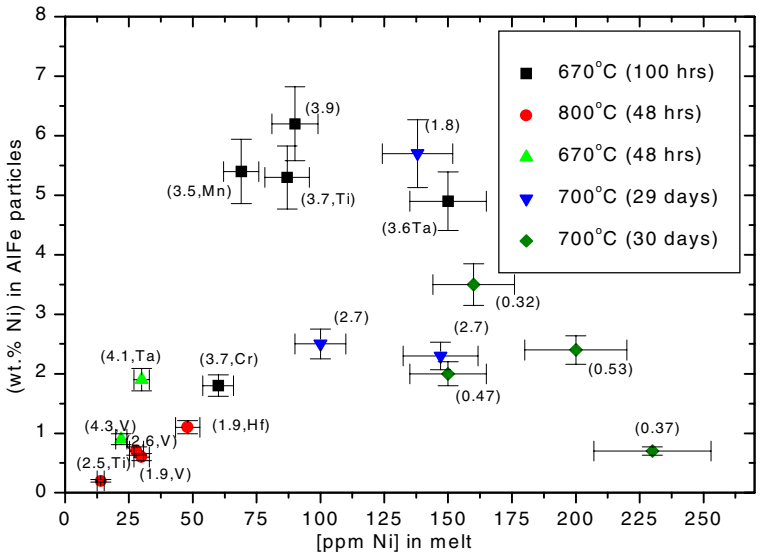

Figure 10.15: (wt.% Ni) in particles versus nickel in melt at various temperatures and holding times for the AlFe phase only. The numbers in the parentheses are final [%Al] in the melt. The additional element X used for the treatment are also given in parentheses (see Table 10.14).

Figure 10.15 shows a relation between nickel content in only AlFe phase in equilibrium with nickel in the melt at various temperature and holding time. The numbers in the parentheses are the end aluminium [wt.%] in the melt. From Figure 10.14 and Figure 10.15 we notice that the nickel content in the melt tends to be high with low aluminium content in the melt.

10.3 Discussion

We regard Al(Fe,Ni) as a dilute solution of AlNi in AlFe:

Al(Fe,Ni) = AlFe + AlNi

As nickel in the melt is assumed to be in equilibrium with nickel in the particles:

a(Ni) in the melt = a(Ni) in the particles

Using the Gibbs energy of dissolution of AlNi in magnesium (estimated using equation (6.19)), the activity of AlNi in Al(Fe,Ni) can be calculated corresponding to the contents of nickel and aluminium in the melt and the temperature.

$$a_{\mathrm{AlNi}} = \frac{[\%\mathrm{Al}][\%\mathrm{Ni}]}{\exp\left(\frac{73.2}{R} - \frac{77100}{RT}\right)} \tag{10.1}$$

The mole fraction AlNi is given by:

$$X_{\mathrm{AlNi}} = \frac{\frac{(\%\mathrm{Ni})}{58.69}}{\frac{(\%\mathrm{Ni})}{58.69} + \frac{(\%\mathrm{Fe})}{55.85}} \tag{10.2}$$

In equation 10.2 the iron content is calculated by subtracting nickel content (in AlFe) from the iron (67 wt.%) in the line compound AlFe

The relative accuracy calculated for activity and mole fraction AlNi is ±14%. The accuracy for the value for Gibbs energy of dissolution of AlNi is not taken into account.

Figure 10.16 shows a relation between the activity of AlNi with the mole fraction AlNi in AlFe particles calculated using equations (10.1) and (10.2). The numbers in the parentheses are the ratio of at.% Al to at.% Fe in the particles (Table 10.14, column 6). The slope of the line gives the activity coefficient γ_{AlNi}, that is 1.16±0.32.

It seems that the deviation from the line does not seem to depend in any systematic manner on the Al/Fe ratio. When the melt is treated with manganese, rare earth, and zirconium the particles formed are different from AlFe. Therefor these elements will are not included in Figure 10.16 and Figure 10.17. The effect of manganese addition on nickel solubility is treated in Chapter 9. Zirconium forms various forms with iron in pure magnesium. These phases are given in Figure 7.13.

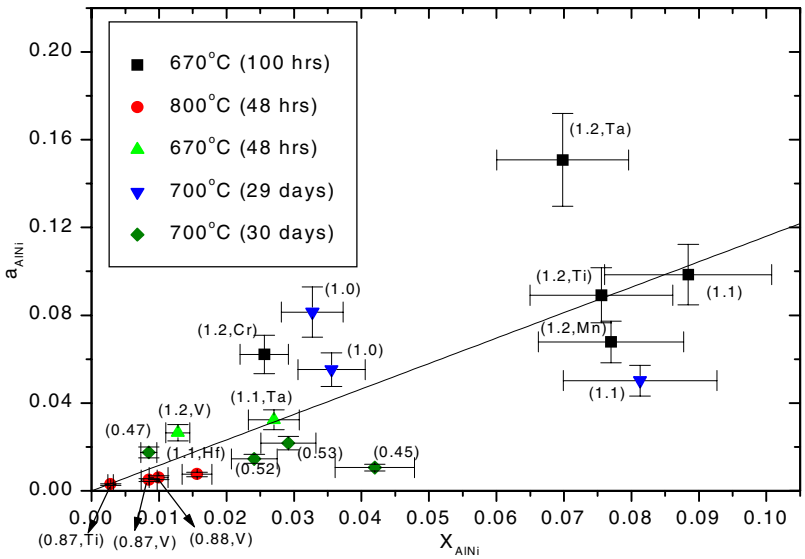

Figure 10.16: Activity of AlNi versus mole fraction AlNi in AlFe particles using equations (10.1) and (10.2). The numbers in the parentheses are ratio of at.% Al to at.% Fe in the particles (see Table 10.14). The elements used for treatment are also given in the parentheses. Notice that Mn, RE and Zr are not included that form particles different from AlFe.

Activity of AlNi is recalculated based on the Gibbs energy of formation of AlNi (equation (6.12)) in magnesium and is given by:

$$a_{AlNi} = \frac{[\%Al][\%Ni]}{\exp\left(\frac{77.9}{R} - \frac{80000}{RT}\right)} \tag{10.3}$$

The activity values calculated by equation (10.3) are plotted against mole fraction AlNi in Figure 10.17. The slope of line gives the activity coefficient γ_{AlNi} that is 0.95±0.32.

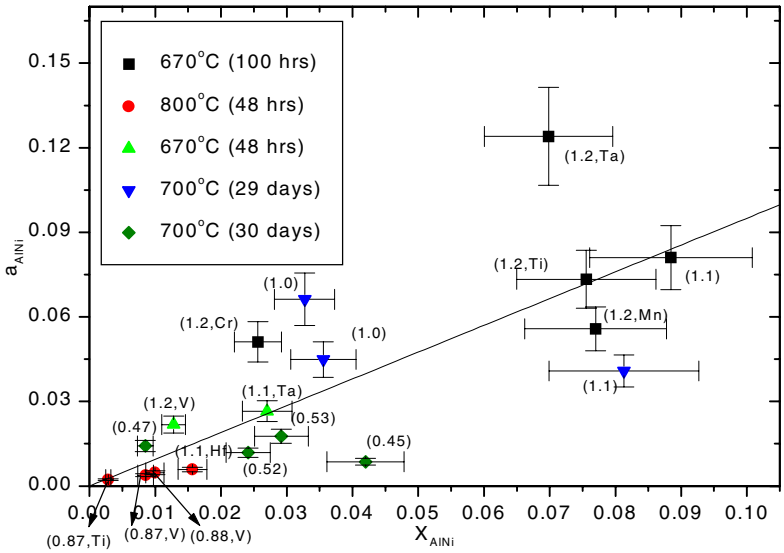

Figure 10.17: Activity of AlNi versus mole fraction AlNi in AlFe particles using equation (10.2) and (10.3). The numbers in the parentheses are ratio of at.% Al to at.% Fe in the particles (see Table 10.14). The elements used for the treatment are also given in the parentheses. Notice that Mn, RE and Zr are not included that form particles different from AlFe.

For the experiments lasting 29 and 30 days one may suspect that there no longer is equilibrium between nickel in the particles and the nickel and aluminium in the melt. During this period a large part of the initial aluminium has gone into the walls.

One reason for deviations may be the different nickel content in various AlFe particles in one sample. For instance nickel content in Sample 9A varies from 1.2 - 2.3 wt.% (Table 10.15). It is mentioned previously that the highest nickel content in the particles is used in figures.

TABLE 10.15: Ni content in various AlFe particles in Sample 9A.

Particle no.	(wt.%Ni)
1	2.3
2	1.2
3	1.3
4	2.3
5	2.2
6	1.4

In the following a mass balance is set up to check that the content of nickel in the particles is reasonable. The reduction of aluminium content will be used to estimate the content of AlFe phase formed. In these calculations aluminium and nickel removed to walls is neglected.

Let M be the mass of melt and M_p be the total mass of AlFe intermetallic particles. The total mass of particles means the amount of intermetallics in the melt plus intermetallics in the capsule walls.

The mass balance for aluminium is:

Total mass of aluminium in AlFe phase (M_{Al}) = Reduction of aluminium fraction times the mass of melt (M)

$$M_{\mathrm{Al}} = \frac{[\%\mathrm{Al}]_{\mathrm{start}} - [\%\mathrm{Al}]_{\mathrm{end}}}{100} M$$

AlFe contains 67% iron by weight. Therefor the mass of intermetallics will be given by:

Mass of intermetallic particles (M_p)= mass of aluminium (M_{Al}) + mass of iron (~$2M_{Al}$)

Mass balance nickel:

$$\frac{(\%\text{Ni})M_p}{100} + \frac{[\%\text{Ni}]_{\text{end}} \times M}{100} = \frac{[\%\text{Ni}]_{\text{start}} \times M}{100} \tag{10.4}$$

where (%Ni) is the nickel content in the particles. $[\%\text{Ni}]_{\text{start}}$ is initial content of nickel in the melt and $[\%\text{Ni}]_{\text{end}}$ is the final nickel content in the melt after the treatment.

Table 10.16 shows a comparison of calculated nickel content in AlFe particles calculated using equation (10.4) and nickel content measured using microprobe or SEM for some of the samples.

TABLE 10.16: Comparison of nickel content calculated from equation (10.4) with measured nickel content in FeAl particles.

Sample no.	(%Ni) Calculated	(%Ni) Measured
246V	0.075	0.3-0.7
361Hf	0.018	1
316V	0.04	0.6
225Ti	0.09	0.1-0.2
9A	0.85	1.68
9B	0.89	1.79
9C	1.58	4

Table 10.16 shows that the calculated nickel content in particles is significantly lower than the measured nickel content. This can be explained by the fact that aluminium penetrates into the capsule walls. In equation (10.4) M_P is too large and thus (%Ni) is too small. Figure 10.18 and Figure 10.19 give the contents of aluminium and nickel inside the capsule walls in samples 9A, 9B, 9C, and 9D. These samples were kept at 700°C for 29 days. The aluminium and nickel content were measured using microprobe point analysis.

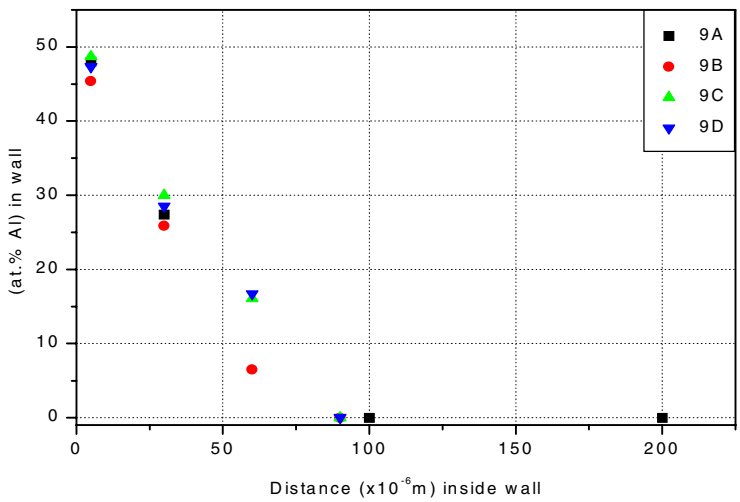

Figure 10.18: Content of aluminium inside the capsule wall. 0 on x-axis is the capsule surface in contact with the melt.

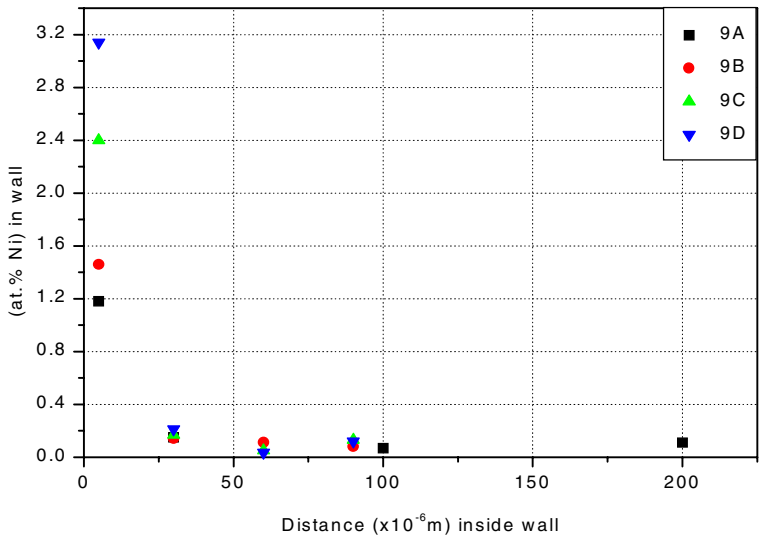

Figure 10.19: Content of nickel inside the capsule walls. 0 on x-axis is the capsule surface in contact with the melt.

10.4 Conclusion

The possibility of removing nickel from Mg-Al alloys has been studied by precipitating with another element X in a temperature range 670-800°C. Element X in this study was Cr, Zr, Mo, Mn, V, Hf, RE, Ti or Ta, and there was always an excess of element X in the melt. Some samples were treated without any addition of element X.

For aluminium contents between 3-5%, FeAl is the equilibrium phase in Mg-Al alloys saturated with iron. Addition of elements Ta, Cr, Hf, V, Ti and small amounts of Mn do not seem to significantly change the composition of the precipitated FeAl particles. Figure 10.16 and Figure 10.17 indicate that nickel in the FeAl particles may be regarded as an ideal solution of NiAl in FeAl.

Higher amounts of Mn, RE and Zr give precipitates different from FeAl.

10.5 Application

If no aluminium is lost to the walls of the iron capsule, the mass balance given by equation (10.4) can be employed with a distribution coefficient $K = (\%\mathrm{Ni})/[\%\mathrm{Ni}]$ to get:

$$\frac{[\%\mathrm{Ni}]_{\mathrm{end}}}{[\%\mathrm{Ni}]_{\mathrm{start}}} = \frac{M}{M_P K + M} \tag{10.5}$$

If distribution coefficient is known, it is easy to calculate the amount of intermetallics needed to reduce nickel content to a lower level in a given amount of melt.

Example:

What will be the amount of AlFe required to lower the nickel content from 50 ppm to 10 ppm in a magnesium melt of 100 kg?

Solution:
From Figure 10.15 the distribution coefficient (K) at 800°C is approximately 200.

$[\%\mathrm{Ni}]_{\mathrm{start}}$	= 50 ppm
$[\%\mathrm{Ni}]_{\mathrm{end}}$	= 10 ppm
Amount of melt (M)	= 100kg

Using equation (10.5) the amount of AlFe (M_p) will be 2 kg.

Chapter 11

Summary of thermodynamic results and recommendations

11.1 Mg-X, Mg-Ni systems

Partial excess Gibbs energies of dissolution of various elements *i* in magnesium are reviewed in Table 3.1. The activity coefficients calculated at 1000K are also given.

The standard Gibbs energy for solution of 1 mass% nickel in liquid magnesium calculated from activity data by Feufel (1993) is found to be:

$$\mathrm{Ni(s)} = \underline{\mathrm{Ni}} \qquad \Delta\overline{G}^{\circ}(\%) = -43500 - 22.2T$$

Standard Gibbs energy for solution of 1 mass% nickel in liquid magnesium calculated from Kubachewski et al. (1993) is more negative and is:

$$\mathrm{Ni(s)} = \underline{\mathrm{Ni}} \qquad \Delta\overline{G}^{\circ}(\%) = -25375 - 55T$$

11.2 Mg-Al-Ni system in Al_2O_3 crucible

The solubility of nickel in liquid Mg-Al alloys has been measured in the temperature range 650-900°C and for 1-10% aluminium content in the alloys. Compared to pure magnesium the solubility in magnesium-aluminium alloys shows a marked reduction. Addition of only 1 wt.% aluminium reduces nickel solubility from about 37.5 wt.% to about 0.52 wt.% at 700°C whereas at 5 wt.% aluminium the solubility further reduces to 0.22-wt.%.

Linear relationships between the logarithm of solubility of aluminium and nickel, as a function of the inverse of the absolute temperature fit the experimental data well.

SEM analysis of samples taken at various temperatures and compositions shows that the precipitated phases in equilibrium with the melt are AlNi and Al_3Ni_2 with the latter becoming more dominant as the aluminium concentration increases.

Thermodynamic data obtained by fitting and "bootstrapping" for the precipitation of AlNi from dissolved aluminium and nickel (Al + Ni = AlNi) in magnesium in mass percent are given below.

Parameters	Fitting	Bootstrap
$\Delta H°$ J/mol	-77100	-76900±3000
$\Delta S°$ J/molK	-73.2	-73.0±3.0
e_{Al}^{Ni}	-0.032	-0.033±0.004
e_{Ni}^{Al}	-0.075	-0.075±0.009

11.3 Mg-Ni-Fe-X system in iron capsule

In an iron capsule the possibility of removing dissolved nickel from (pure) magnesium has been studied by precipitating with another element X. Element X in this study was Zr, Mo, Mn, V, Hf, Ti or Ta. X was always present as separate phase (in excess). ICP-AES and SEM analysis of samples treated with molybdenum, tantalum, and hafnium did not show any removal of nickel.

Manganese forms a γ(Fe,Mn) phase containing small amounts of nickel. The results with vanadium indicate that vanadium can remove iron even though the solubility of vanadium in magnesium is low.

The ICP-AES analysis results show the reduction of nickel from 200 ppm to less than 50 ppm in the case of zirconium. SEM analysis of samples treated with zirconium indicated the presence of various Zr-Fe phases also containing nickel. Titanium also reduced the nickel content to some extent.

Compositions of the phases formed are determined by quantitative analysis in SEM and are compared with phase diagrams. From the SEM analysis it is found that zirconium and titanium dissolve in magnesium and form various intermetallic phases with iron. Microprobe investigations confirmed the formation of Fe-Zr particles also containing nickel. These particles contain different amounts of nickel depending on the phase. Three different phases were observed having different shapes and compositions.

Shape	Plate	Needle	Speck
at.% Ni	2.36	2.08	1.40
at.% Fe	28.69	14.12	15.80
at.%Zr	64.31	48.83	78.08
Phase	Zr_2(Fe,Ni)	Zr_3(Fe,Ni)	Zr_4(Fe,Ni)

In summary, zirconium and titanium remove nickel from magnesium by forming various intermetallic phases with iron also containing nickel. The various phases identified are Zr_2(Fe,Ni), Zr_3(Fe,Ni), Zr_4(Fe,Ni), Ti(Fe,Ni) and Ti(Fe,Ni)$_2$.

11.4 Mg-Al-Fe-Ni system in Al_2O_3 crucible

The solubilities of iron and nickel in Mg-Al alloys have been determined in the temperature range 650-900°C and 0.70-9.01 wt.%Al content in the alloys. For Mg-Al alloys saturated with iron and nickel, microprobe analysis of the samples shows that the composition of the precipitated phases contain small amounts of iron but is close to AlNi composition. The iron content in the particles is below 3.5 at.%. The nickel content in the melt remains below 2.5 wt.% and the iron content below 284 ppm by mass. The thermodynamic data obtained by fitting and bootstrapping for the precipitation of stoichiometric Al($Ni_{0.89,}Fe_{0.11}$) phase in magnesium alloy melt are

Parameters	Fitting	Bootstrap
$\Delta H°$ J/mol	-75300	-74100±3900
$\Delta S°$ J/molK	-69.3	-68.0±3.8
e_{Al}^{Fe}	0	0
e_{Fe}^{Al}	0	0

For $Al(Ni_{0.89,}Fe_{0.11})$ = $\underline{Al}$ + 0.89$\underline{Ni}$ + 0.11$\underline{Fe}$ in Mg-Al melt, the Gibbs energy is given by:

$\Delta G^{\circ}(\%)$ = 75300 - 69.3T

and for AlNi = $\underline{Al}$ + $\underline{Ni}$ in Mg-Al melt (see equation 6.20)

$\Delta G^{\circ}(\%)$ = 77100 - 73.2T

The $\Delta G^{\circ}(\%)$ for the formation of AlNi are close to $\Delta G^{\circ}(\%)$ for the formation of $Al(Ni_{0.89,}Fe_{0.11})$ indicating that iron has little or no effect on the solubility of nickel in Mg-Al alloys.

11.5 Mg-Al-Ni-Mn system in Al_2O_3 crucible

The solubilities of manganese and nickel in Mg-Al alloys has been measured in the temperature range 650-900°C and aluminium content 1-10wt.%. The amount of manganese and nickel was added such that there was an excess of these elements at 900°C. The 'line compounds' determined using solubility data at various aluminium contents and their Gibbs energy of formation is:

For 9.96-10.8% Al
$Al(l) + 0.5Mn(s) + 0.4Ni(s) = AlMn_{0.5}Ni_{0.4}(s)$, ΔG° = -67096 + 5.2T

For 2.91-4.53% Al
$Al(l) + 0.6Mn(s) + 0.3Ni(s) = AlMn_{0.6}Ni_{0.3}(s)$, ΔG° = -81332 + 16.8T

For 0.38-1.37% Al
$Al(l) + 1.1Mn(s) + 0.55Ni(s) = AlMn_{1.1}Ni_{0.55}(s)$, ΔG° = -79337 - 11.7T

The solubility of nickel is higher in Mg-Al alloys saturated with manganese as compared to pure Mg-Al alloys.

11.6 Mg-Al-Ni-Fe-X system in iron capsule

The possibility of removing nickel from Mg-Al alloys saturated with iron has been studied by precipitating with element X in a temperature range 670-800°C. Element X in this study was Cr, Zr, Mo, Mn, V, Hf, RE, Ti or Ta. X was always present as a separate phase (in excess). Some samples were treated without any addition of element X.

For aluminium contents between 3-5%, FeAl is the equilibrium phase in Mg-Al alloys saturated with iron. Addition of elements Ta, Cr, Hf, V, Ti and small amounts of Mn do not seem to significantly change the composition of the precipitated FeAl particles. Higher amounts of Mn, RE and Zr give precipitates different from FeAl.

The results indicate that nickel in the FeAl particles may be regarded as an ideal solution of NiAl in FeAl.

11.7 Recommendations for further work

There seems to be a large scatter in the published data for important Mg-*i* binary systems. For example, there is a considerable scatter in the data for Fe, Mn, and Zr in magnesium. Therefore thermodynamic data for Mg-*i* systems should be critically evaluated, and if required more experiments should be performed.

The distribution coefficient of nickel in the melt to the nickel in the AlFe particles should be determined at various temperatures and alloy compositions. These experiments should be conducted in an Al_2O_3 or MgO crucible to avoid loss of aluminium to steel walls. It should be important to study the kinetics for the removal of nickel from Mg-Al alloys using AlFe particles. The possibility of employing other elements like carbon should also be studied. Finally the process should be applied on an industrial scale, and the various ways of suspending AlFe particles in Mg-alloy melts and also the possibility of using AlFe particles as a filter should be studied.

References

Aune, T. K., Bakke, P., Westengen, H., Mellerud, T. and Albright, D. L., (1997), "Potential for Improving Recycling Friendliness of High Purity Magnesium Die Casting Alloys", *NADCA*, Minneapolis, Minnesota, Nov. 1997.

Bakke, P., (1992), "Measurement and Removal of Inclusions and Hydrogen in Magnesium", Dr. Ing. Thesis, Division of Metallurgy NTH, Trondheim, Norway.

Bakke, P. and Karlsen, D. O., (1997), "Inclusion Assessment in Magnesium and Magnesium Base Alloys", *SAE Technical Paper* 970330.

Bakke, P., Sannes, S. and Albright, D., (1999), "Effects of Ni, Cu, Si and Co on the Corrosion Properties of Permanent Mould Cast Medallions and Die Cast Plates of Magnesium Alloy AZ91", *SAE Technical Paper* 1999-01-0926.

Bakke, P., Fuerst, C. D. and Westengen, H., (2000a), "Solidification Induced Inhomogenities in Magnesium-Aluminium Alloy AZ91 Ingots", *Magnesium Technology 2000*, *Ed.: H.I. Kaplan, J. Hryn, and B. Clow,* TMS-AIME, Warrendale, PA, USA, pp. 201-210.

Bakke, P., Pettersen, K., Guldberg, S. and Sannes, S., (2000b), "The Impact of Metal Cleanliness on Mechanical Properties of Die Cast Magnesium Alloy AM50*", Magnesium Alloys and their Applications, Ed.: K. U. Kainer,* 5th Intl. Magnesium Conference, Munich, Germany*,* Sept. 26-29, pp. 739-745.

Bakken, H. E., (1926), "Magnesium - aluminium alloy", US Patent 1,584,688.

Bale, C.W. and Pelton, A.D., (1990), "The Unified Interaction Parameter Formalism-Thermodynamic Consistency and Applications", *Met. Trans. A*, Vol. 21A, pp. 1997-2002.

Beck, A and Schmidt, W., (1929), "Verfahren zur Entfernung von suspendierten Teilchen von Eisen und ahnlichen fein verteilte Verureinungen von nicht salzartigem

Charakter aus Magnesium und hochprozentigen Magnesiumlegierungen", German Patent No. 604 580.

Berkmortel, R., Wang, G. and Bakke, P., (2000), "Fluxless In-house Recycling of High Purity Magnesium Die Cast Alloys at Meridian Operations", *Proceedings of the 57th IMA Annual World Conference*, Vancouver, BC, Canada.

Brassard, C. and Riopelle, L., (1997), "Recycling of Magnesium Scrap, A Necessity", *Light Metals 1997. Ed.: R. Huglen*, TMS-AIME Warrendale, PA, USA, pp. 1,111-1,114.

Byun, J. Y., Shim, J. D., Moon, J. H. and Paik, Y.H., (1997), "Iron Solubility in AZ91D Alloy", *Light Metals*, 36th Annual Conference of Metallurgists of CIM, p. 103-114.

Cussler, E. L., (1997), *Diffusion. Mass Transfer in Fluid Systems,* Cambridge University Press, New York, USA.

Edgar, R. L., (1999), "Magnesium Supply and Demand 1998", *Proceedings of the 56th IMA Annual World Magnesium Conference,* Rome, Italy, pp. 1-6.

Elliott, R. P., (1965), *Constitution of Binary Alloys, First Supplement*, McGraw-Hill Book Company, New York, USA.

Emley, E. F. and Fox, F. A., (1945), "Improvements in or Relating to the Treatment of Magnesium and Magnesium Base Alloys", UK patent 594,152, March 22.

Emley, E. F., (1966), *Principles of Magnesium Technology*, Pergamon Press Ltd., Oxford, UK.

Engh, T. A., (1992), *Principles of Metal Refining*, Oxford University Press, Oxford, UK.

FACT-Win 3.05-Thermochemical Database Computing System Copyright 1976-1999 Thermfact/CRCT, Ecole Polytechnique de Montréal, Québec, Canada.

Farner, S., (2000), "Remelting of Aluminium by Continuous Submersion of Rolled Scrap", Dr. Ing. Thesis, Department of Materials Technology and Electrochemistry, NTNU, Trondheim, Norway.

Faure, P., (1995), "Process for the Recovery of Magnesium from Magnesium Alloys Waste", U.S. Patent 5,476,529.

Fenstad, J., (2000), "Liquidus Relations and Thermochemistry within the System Fe-Mn-C-O" Dr. Ing. Thesis, Department of Materials Technology and Electrochemistry, NTNU, Trondheim, Norway.

Feufel, H., (1993), "Thermodynamic Examination of Binary and Ternary Magnesium Alloys", Ph. D. Thesis, Faculty for Chemistry, University of Stuttgart (In German).

Foerster, G. S., (1975), "Removal of Nickel from Molten Magnesium Metal", U. S. Patent 3,869,281.

Fox, F. A. and Bushrod, C. J., (1944), "Improvements in or Relating to Production of Magnesium Base Alloys", UK patent 591,225, Aug. 8.

Friesen, K. J., Utigard, T. A., Dupuis, C. and Martin, J. P., (1997), "Coalescence Behaviour of Molten Aluminium Droplets under a Molten Salt Flux Cover", *Light Metals 1997, Ed.: R. Huglen*, TMS-AIME Warrendale, PA, USA, pp. 857-864.

Frisvold, F., Bakke, P., Øvrelid, E., Hald, N. E. and Engh, T. A. (1996), "Hydrogen and Inclusion Content in Recycled Aluminium at Holmestrand Rolling Mill", *Light Metals 1996, Ed.: W. Hale*, TMS-AIME Warrendale, PA, USA, pp. 1011-1016.

Gaskell, D.R., (1995), *Introduction to the Thermodynamics of Materials,* 3rd ed., Taylor and Francis, Washington DC, USA.

Haerle, A. G., Mikucki, B. A. and Mercer II, W. E. (1996), "A New Technique for Quantifying Non-Metallic Inclusion Content in Magnesium", *Light Metal Age*, Aug. 1996, pp. 22-29, Haerle, A. G., Mikucki, B. A. and Mercer II, W. E. (1996) "Premium Quality Recycled Magnesium Alloys Through Analysis and Process Control", *Proceedings of Metallurgie du et recherche d'alegement dans l'industrie des transports*, 1996, pp.11-23 and Haerle, A. G., Murray, R. W., Mercer II, W. E, Mikucki, B. A. and Miller, M. H.,. (1997) "The Effect of Non-Metallic Inclusions on the Properties of Die Cast Magnesium", *SAE Technical Paper* 970331.

Hallstedt, B., (1993), "The Magnesium-Oxygen System", *CALPHAD*, Vol. 17, No. 3, pp. 281-286.

Hanawalt, J. D., Nelson, C. E. and Holdeman, G. E., (1941), "Removal of Iron from Magnesium-base Alloys", U.S. Patent 2,267,862.

Hanawalt, J. D., Nelson, C. E. and Peloubet, J. A. (1942), "Corrosion Studies of Magnesium and its Alloys", *Trans. AIME,* 147, pp. 273-299.

Haugland, E., (1998), “Removal of Inclusions by Gas Purging”, Dr. Ing. Thesis, Department of Metallurgy NTNU, Trondheim, Norway.

Hillis, J. E., (1983), “The Effect of Heavy Metal Contamination on Magnesium Corrosion Performance”, *SAE Technical Paper* 830523, *SAE Trans.,* Vol.92.

Hillis, J. E. and Green, W. G., (1988), “Method for Removing Iron Contamination from Magnesium”, U.S. Patent 4,773,930.

Hillis, J. E. and Mercer II, W. E., (2000), “Separation of Non-Metallic Contaminants in Fluxless Melting and Refining of Magnesium Alloys*”, SAE Technical Paper 2000-01-1125.*

Ho, F. K. and Sahai, Y., (1990), “Interfacial Phenomena in Molten Aluminium and Salt Systems”, *2nd Intl. Symp. - Recycling of Metals and Engineered Materials, Eds.: J.H.L. van Linden, D. Stewart and Y. Sahai*, TMS-AIME, Warrendale, PA, USA, pp. 85-103.

Holdeman, G. E., (1941), “Removing Iron from Magnesium Alloys”, US patent 2,304,093, Dec. 16.

Holta, O., Westengen, H. and Røen, J., (1996), “High Purity Magnesium Die Casting Alloys. Impact of Metallurgical Principles on Industrial Practice”, *3rd Intl. Magnesium Conference*, Manchester, UK, April 10-12.

Housh, S. E. and Petrovich, V., (1992), “Magnesium Refining: A Fluxless Alternative”, *SAE Technical Paper* 920071.

Hu, H. and Luo, A., (1996), “Inclusions in Molten Magnesium and Potential Assessment Techniques”, *JOM*, Vol. 48, Nr. 10, pp. 47-51.

Hultgren R., Desai, P.D., Hawkins, D.T., Gleiser, M. and Kelly, K.K., (1973), *Selected Values of the Thermodynamic Properties of Binary Alloys,* American Society for Metals, Metals Park, Ohio, USA.

Höllrigl-Rosta, F., Just, E., Köhler, J. and Melzer, H. J., (1980), “Magnesium in Volkswagen”, *Proceedings of the 37th IMA Annual World Magnesium Conference*, pp. 38-45.

Ichkawa, R. and Saito, R., (1965), “The Distribution of Beryllium in Solid Magnesium Alloys Containing Beryllium at High Temperatures” *Trans. JIM*, Vol. 6, pp. 78-82.

Jacques, R. P., Gupta, R. D. and Haerle, A. G., (1997), "Evaluation of Recycled AZ91D Magnesium Alloy for Steering Column Components", *SAE technical paper 970332.*

King, J. F. and Thistlethwaite, S., (1994), "Magnesium Recycling for the European Die Casting Industry", *EFM-Aalen Magnesium Abnehmerzeminar*, Sept. 15-16.

Komura, A., Imanga, H. and Watanabe, N., (1973), "Dispersion of Mg in the Electrolysis of $MgCl_2$-KCl Melts", *Denki Kagaku*, Vol. 41, Nr. 4, pp. 281-286.

Kubaschewski, O. and Hopkins, B. E., (1962), *Oxidation of Metals and Alloys*, 2nd ed., Butterworths & Co. Ltd, London, UK.

Kubaschewski, O. and Alcock, C.B., (1979), *Materials Thermochemistry,* 5th ed., Pergamon Press, Oxford, UK.

Kubaschewski, O., Alcock, C.B. and Spencer, P.J., (1993), *Materials Thermochemistry,* 6th ed., Pergamon Press, Oxford, UK.

Leontis, T. E. and Rhines, F. N., (1946), *Trans. Amer. Inst. min. (metall.) Engrs.* Vol.166, pp. 265.

Lide, D. R. (Ed.), (1990), *CRC Handbook of Chemistry and Physics*, 71th ed.CRC Press, Inc., Boca Raton, Florida.

Lupis, C. H. P. and Elliott, J. E., (1966), "Generalised Interaction Coefficients," *Acta Metallurgica*, Vol. 14, p. 529-538.

Lupis, C.H.P., (1983), *Chemical Thermodynamics of Materials*, Elsevier Science Publishing Co., Inc., New York.

Massalski, T. B., (1990), *Binary Alloy Phase Diagrams*, 2nd ed., ASM International, Metals Park, Ohio, USA.

Massalski, T.B., Okamoto, H., Subramanian, P.R. and Kacprzak, L., (1996), "Binary Alloy Phase Diagrams", 2nd ed. (A Data Programme), ASM International, Metals Park, Ohio, USA.

Nayeb-Hashemi, A. A. and Clark, J. B., (1988), *Phase Diagrams of Binary Magnesium Alloys*, ASM International, Metals Park, Ohio, USA.

Origin User Manual version 5, Microcal Software Inc. 1997, Northampton, USA.

Pinfold, P. M. D. and Øymo, D., (1993), "An Evaluation of Refined, Recycled AZ91D Alloy", *SAE Technical Paper* 930420.

Petrovich, V. W. and Waltrip, J. S., (1988), "Flux-free Refining of Magnesium Die Cast Scrap", *Light Metals 1989, Ed.: P.G. Campbell*, TMS-AIME, Warrendale, PA, USA, pp. 749-755.

Polmear, I. J., (1994), "Magnesium Alloys and Applications", *Materials Science and Technology*, Vol. 10, Jan., pp. 1-15.

Press, H. P., Teukolsky, S. A., Vetterling, W. T. and Flannery, B. P., (1992), *Numerical Recipes in C:* The Art of Scientific Computing, 2nd ed., Cambridge University Press, UK.

Reding J. N., (1976), "Apparatus and Method for Refining Magnesium", U.S. Patent 1,424,543.

Rosenqvist, T., (1983), *Principles of Extractive Metallurgy*, 2nd ed., McGraw-Hill, New York, USA.

Schmitz & Apelt LOI, (2000), "Fluxless Recycling in Continuous Operation", *Commercial Brochure.*

Schneider, V. A. and Stendel, J., (1960), "Ausfällung intermetallischer Phasen aus einem flüssigen Lösungsmetall", *Z. f. Anorg. Chemie*, Vol. 303, pp. 227-246.

Siebel, V. G., (1948), "On the Solubility of Iron, Manganese, and Zirconium in Magnesium and Magnesium Alloys", *Zeitschrift für Metallkunde,* Vol. 39, pp. 22-27 (In German).

SigmaPlot for Windows Version 4.00 Copyright 1986-1997 SPSS Inc. 444 North Michigan Avenue, Chicago, IL 60611.

Simensen, C. J. and Oberländer, B., (1980), "A Survey of Inclusions in Magnesium", *Z. Praktische Metallographie*, B.17, H.3, pp. 125-136.

Simensen, C. J., (1981), "Impurities in Light Metals", *Støperitidende*, Vol.47, pp.176-184 (In Norwegian).

Simensen, C. J., Oberländer, B. C., Svalestuen, J. and Thorvaldsen, A., (1989), "The Effect of Iron on Mg-4 wt.%Al-Mn Alloys", *Zeitschrift für Metallkunde*, Vol. 80, Nr. 2, p. 101-103.

Simensen, C. J. and Kolby, P., (1995), "Removal of Nickel from Molten Magnesium Alloys", SINTEF Report STF24 F95046 (Restricted), Trondheim, Norway.

Simensen, C. J. and Horst, J. A. (1996), "Analysis of Intermetallic Phases in Materials of AZ91 Contaminated with Nickel", SINTEF Report STF24 F96017 (Restricted), Trondheim, Norway.

Squires, G. L., (1989), *Practical Physics, 3rd ed.*, Cambridge University Press, Cambridge, UK.

Tathgar, H. S., Bakke, P., Øvrelid, E., Fenstad, J., Frisvold, F. and Engh, T. A., (2000a), "Solubility of Nickel in Molten Magnesium-Aluminium Alloys above 650°C", *Magnesium Technology 2000. Ed.: H.I. Kaplan, J. Hryn, and B. Clow,* TMS-AIME, Warrendale, PA, USA, pp. 181-189.

Tathgar, H. S., Bakke, P. and Engh, T. A., (2000b), "Impurities in Magnesium and Magnesium Based Alloys and their Removal", *Magnesium Alloys and their Applications, Ed.: K. U. Kainer,* 5th Intl. Magnesium Conference, Munich, Germany, Sept. 26-29, pp. 767-779.

Toya, T. and Kato, A., (1983), *Practical Techniques for Microprobe Analysis,* JOEL Training Centre.

Unsworth, W. and King, J. F., (1986), "Recent Casting Alloy Developments", *Proc. of Intl. Conf. on Magnesium Technology*, London, UK, pp. 25-29.

Wagner, C., (1952), *Thermodynamics of Alloys*, Addison-Wesly Publishing Company, Inc., Reading, Massachusetts, USA.

Wallevik, O. and Rønhaug, J. B., (1992), "Method and Apparatus for Melt-Down and Refining of Magnesium and Magnesium Alloys", Norwegian patent 171120 (In Norwegian).

Waltrip, J. S., (1990), "Magnesium Casting Scrap Value Recovery", *SAE Technical Paper* 900789.

Wang, J. S. and Engell, H. J., (1992), "Investigation of the Thermodynamic Properties of Ni-Al Compounds by an EMF Method" *Steel Research*, Vol. 63, Nr. 8, pp. 320-323.

Weast, R. C. (Ed.), (1980), *CRC Handbook of Chemistry and Physics*, 60th ed., CRC Press, Inc., Boca Raton, Florida.

Ye, J. and Sahai, Y., (1996), "Interfacial Behaviour and Coalescence of Aluminium Drops in Molten Salts", *Materials Trans, JIM*, Vol.37, Nr. 2, pp. 175-180.

Øvrelid, E. J., (1997), "Hydrogen Solubility in Magnesium and Magnesium Alloys. Removal of Hydrogen", Dr. Ing. Thesis, Department of Metallurgy, NTNU, Trondheim, Norway.

Øvrelid, E. J., Frisvold, F. and Engh T. A. (1997), "Removal of Nickel from Pure Magnesium. A Laboratory Study of the Feasibility of Using Elements Zr, Mo, Mn, V, Hf, Ti, and Ta as Media for Removal of Ni", SINTEF report STF24 F96626 (Restricted), Trondheim, Norway.

Øymo, D., Holta, O., Hustoft, O. M. and Henriksson, J., (1992), "Magnesium Recycling in the Die Casting Shop", *Proceedings of the 1992 conference on the recycling of metals*, Düsseldorf/Neuss, Germany, 13-15th May, pp. 143-150.

Øymo, D., Karlsen, D. O., Pinfold, P. M. D., Mellerud, T. and Lie, O., (1994), "Particle Removal in Pure Magnesium", *Light Metals 1994. Ed.: U. Mannweiler*, TMS-AIME, Warrendale, PA, USA, pp. 251-258.

APPENDIX A

Certificate of analysis (Capsule experiments)

Chemical compositions of the materials used in Chapter 4, Table 4.1.

Table A.1: Steel capsule (ST 37) analysed by SINTEF MOLAB, MO, Norway

%Al	%As	%B	%C	%Co	%Cr	%Cu	%Mn	%Mo
0.041	0.002	0.0001	0.09	0.003	0.026	0.083	0.50	0.004

%Nb	%Ni	%P	%S	%Si	%Sn	%Ti	%V	%W
0.001	0.023	0.016	0.013	0.02	0.004	0.001	0.001	0.01

Table A.2: Magnesium pieces (Stock No. 36193) analysed by Johnson Matthey.

%Al	%Ca	%Cu	%Fe	%Mn	%Si
0.001	<0.001	<0.001	<0.001	<0.001	<0.001

Table A.3: Hafnium (Stock No. 00139) analysed by Johnson Matthey in ppm.

Al	B	C	Ca	Cd	Cl	Co	Cr	Cu
<25	<0.25	38	<20	<2	<5	<5	<20	<25

Fe	H	Mg	Mn	Mo	N	Nb	Ni	O
165	<3	<10	<20	<10	26	<50	<25	280

Pb	Si	Sn	Ta	Ti	U	V	W	Zr
<5	<25	<10	<100	<25	<1	<10	<20	1.72%

Table A.4: Manganese pieces (Stock No. 36221) analysed by Johnson Matthey in ppm.

Ca	Mg
<10	<10

Table A.5: Tantalum foil (Stock No. 00335) analysed by Johnson Matthey in ppm.

Al	B	C	Ca	Co	Cr	Cu	Fe
<5	<5	10	5	<5	<5	5	5

H	Mg	Mn	Mo	N	Na	Nb	Ni
<10	<5	<5	<5	10	ND	30	<5

O	Si	Sn	Ta	Ti	W	Zr
70	<5	<5	Balance	<5	<25	<5

Table A.6: Vanadium wire (Stock No. 00395) analysed by Johnson Matthey in ppm.

Al	B	C	Cr	Cu	Fe	H	Hf
340	<5	25	<100	<50	210	<5	<50

Mo	N	Nb	Ni	O	P	S
280	33	<50	<50	210	<30	<20

Si	Sn	Ta	Ti	U	W	Zr
290	<100	<100	<50	<1	<30	<50

Table A.7: Zirconium foil (Stock No. 00415) analysed by Johnson Matthey in ppm.

Ag	Al	As	Au	Be	Bi	C	Ca
<0.15	5	ND	<0.1	ND	ND	9	0.2

Cd	Cl	Co	Cr	Cu	F	Fe	Ga
ND	10	ND	0.8	2.2	ND	20	0.1

Ge	H	In	K	Li	Mg	Mn	Mo
ND	<1	<0.1	1.5	ND	<0.1	ND	<0.1

N	Na	Nb	Ni	O	P	Pb	Pd
<1	<0.1	<0.1	9	11	0.12	<0.1	<0.1

Pt	Rh	S	Sb	Si	Sn	Ta	Te
<0.1	ND	1	<0.1	5	2	ND	ND

Ti	V	W	Zn
<0.1	ND	<0.1	0.86

Table A.8: Rare-Earth analysed by Norsk Hydro Research Centre, Porsgrunn, Norway

%Al	%B	%Ca	%Ce	%Cr	%Fe
0.016	0.0085	0.045	31.5	<0.002	0.045

%K	%La	%Mg	%Mn	%Na	%Nd
<0.01	54.4	0.009	0.004	<0.001	8.4

%Ni	%P	%Pb	%Pr	%Sm	%Zn
0.026	0.016	0.0019	5.1	<0.001	0.0026

Table A.9: Titanium foil (Stock No. 00971) analysed by Johnson Matthey

%C	%Fe	%H	%N	%O
0.005	0.12	0.0032	0.002	0.075

APPENDIX B

Certificate of analysis (Solubility experiments)

Chemical compositions of materials given in chapter 5, Table 5.1.

Table B.1: Chemical composition of materials.

Material	Mg1	Mg2	AlNi	Al	Mn	Fe
Impurities (%)						
Al	0.001	0.0005				
As						<0.0002
C			0.034			
Ca	<0.001	0.001			<10ppm	
Cl						<0.002
Cu	<0.001					<0.002
Fe	<0.001	0.0001	<0.10			
Mg					<10ppm	
Mn	<0.001					<0.002
O			0.14			
Pb						<0.002
S						<0.002
Si	<0.001	0.0005				
Unknown						<0.1
Zn						<0.002

APPENDIX C

Least squares fitting (Mg-Al-Ni system)

Determination of ΔH°, ΔS° and e_{Al}^{Ni} for the dissolution of AlNi in magnesium using equation (6.19) and solving by the least squares method.

MgAlNi system

delta H 77087.8
delta S 73.2399
e(Al-Ni) -0.0321

Using Wagnerian formalism

Sample nr	%Al	[%Ni]	T	Y1	e(Al-Al)	e(Ni-Ni)	Y2	(Y1-Y2)^2	Y3
515A	9.35	1.36	1173	2.54286	-0.000241	0.012045	2.5857	0.0018	0.0724
525A	8.9	0.63	1073	1.72402	-3.55E-05	0.014161	1.7302	4E-05	
535A	8.8	0.25	973	0.78846	0.000212	0.016712	0.8027	0.0002	
545A	8.8	0.15	926	0.27763	0.000347	0.018101	0.3123	0.0012	
513B	3.6	1.5	1169	1.6864	-0.000233	0.012122	1.5696	0.0137	
523B	3.3	0.62	1073	0.71589	-3.55E-05	0.014161	0.7632	0.0022	
533B	3.2	0.26	959	-0.1839	0.000251	0.017112	-0.3	0.0135	
543B	3	0.17	924	-0.6733	0.000353	0.018164	-0.7048	0.001	
523C	1.1	2.7	1169	1.08856	-0.000233	0.012122	1.1921	0.0107	
523C	0.63	1.7	1073	0.06859	-3.55E-05	0.014161	0.3469	0.0775	
533C	0.33	1.2	959	-0.9263	0.000251	0.017112	-0.761	0.0273	
543C	0.26	0.98	924	-1.3673	0.000353	0.018164	-1.1493	0.0475	
71B	1.14	2.65	1126	1.10559	-0.000149	0.012993	0.8883	0.0472	
72B	0.88	1.99	1077	0.5603	-4.44E-05	0.014069	0.4346	0.0158	
73B	0.59	1.49	1019	-0.1289	9.2E-05	0.015476	-0.1312	6E-06	
74B	0.52	1.26	985	-0.4228	0.00018	0.016379	-0.4689	0.0021	
75B	0.47	1.11	943	-0.6507	0.000296	0.017583	-0.9053	0.0649	
								0.3267	

Y1 = LN[%Al][%Ni], Y3 = st. error of estimate

Y2 = (deltaS/R-deltaH/RT)-2.3[%Ni][e(Ni-Ni)+e(Al-Ni)]-2.3[%Al][e(Al-Al)+e(Ni-Al)]

Using solver to minimise the sum of (Y1-Y2)^2 by changing e(Al-Ni), deltaH and deltaS

The Bootstrap Method for estimating error in the parameters (Press et al. 1992, p. 691):

This method is used when the underlying process, or the nature of measurement errors are not known. In this method a new data set is produced by using the obtained data set.

Suppose we have a N data points. We will make a new data set of N points by randomly picking out N points from the original data points (sampling with replacement). Because of the replacement, we do not simply get back our original data set each time, but in average, e^{-1}~37% of the data will be duplicated. The parameters are fitted to the new data in the same way as before, and a new set of parameters are obtained. This is repeated to gain a large number n (50 in our case) of parameters set (A_j, B_j,.....) where j = 1, 2.....,M.

We will assume that the bootstrap parameters are normally distributed. The mean for each parameter will be given by:

$$\bar{A} = \sum_{j=1}^{n} \frac{A_j}{n}$$

and the bootstrap estimate of the standard deviation for each parameter will be:

$$s(A) = \left(\sum_{j=1}^{n} \left(\frac{A_j - \bar{A}}{n-1} \right) \right)^{\frac{1}{2}}$$

APPENDIX D

Least squares fitting (Mg-Al-Ni-Fe system)

Start contents of aluminium, iron, and nickel in the three alloys used for the study of mutual solubility of iron and nickel in Mg-Al alloys.

Table D.1: Start contents of Al, Ni, and Fe in the three Mg-Al alloys. The rest is Mg.

Alloy	Start wt.% Al	Start wt.% Ni	Start wt.% Fe
Mg-(8.7-9.0)% Al	10.0	2.0	0.2
Mg-(4.9-5.4)% Al	6.0	2.3	0.2
Mg-(0.7-2.3)% Al	2.4	3.8	0.2

The three alloys were heated to 15-20°C above 900°C. Argon gas was bubbled through the melt for four hours such that the melt is saturated with nickel and iron at that temperature. The temperature of the furnace was lowered to 900°C, 800°C, 700°C, and 650°C respectively for taking samples.

Determination of ΔH°, ΔS°, e_{Al}^{Fe}, and α for the dissolution of $Al(Ni^{\alpha}, Fe^{(1-\alpha)})$ in magnesium using equation (8.7) and solving by the least squares method.

Mutual solubility of iron and nickel in Mg-Al alloys.

	Mg-Al	Known	
delta H	75286	e(Al-Ni)	-0.032
delta S	69.335	e(Ni-Al)	-0.075
e(Al-Fe)	0.8522		
Alfa	0.8886		

Sample n	Temp.(C)	[%Al]	[%Ni]	[%Fe]	%[Ni+Fe]	1/T(K)	T (K)	Y1 ln[%Al][%Ni]^e(Al-Al)	e(Ni-Ni)	Y2	(Y2-Y1)^2	Y4 [Ni]est.
612A	900	8.64	1.28	0.028	1.3084	0.000853	1173	1.97888787	-0.0002	0.012	1.956	0.000531	1.2472
622A	791.5	9.01	0.65	0.005	0.6551	0.000939	1065	1.22733867	-2E-05	0.0144	1.233	3.25E-05	0.6542
632A	702	8.7	0.29	0.003	0.2931	0.001026	975	0.4196972	0.00021	0.0167	0.387	0.001078	0.2795
642A	644.5	8.67	0.16	0.003	0.1634	0.00109	917.5	-0.1018984	0.00037	0.0184	-0.209	0.011545	0.1418
612B	900	5.43	1.17	0.01	1.18	0.000853	1173	1.31826365	-0.0002	0.012	1.493	0.030435	1.4238
622B	796	5.38	0.66	0.003	0.663	0.000935	1069	0.66612682	-3E-05	0.0143	0.717	0.002602	0.699
632B	705	5.14	0.31	0.002	0.312	0.001022	978	-0.0961507	0.0002	0.0166	-0.126	0.000863	0.2999
642B	648.5	4.93	0.16	0.002	0.162	0.001085	921.5	-0.7255595	0.00036	0.0182	-0.734	6.52E-05	0.1586
612C	900	2.28	2.51	0.025	2.535	0.000853	1173	1.23083003	-0.0002	0.012	1.044	0.03476	2.0349
622C	800	1.67	1.44	0.006	1.446	0.000932	1073	0.2667244	-4E-05	0.0142	0.209	0.003338	1.3493
632C	697.5	0.7	0.7	0.02	0.72	0.00103	970.5	-1.1095449	0.00022	0.0168	-0.896	0.045717	0.8904
												0.130968	

Y1 = ln[%Al][%Ni]^(Alfa)[%Fe]^(1-Alfa)

Y2 = (delS/R-delH/RT)-2.3{e(Al-Al)[%Al]+e(Al-Ni)[%Ni]+e(Al-Fe)[%Fe]+Alfa(e(Ni-Ni)[%Ni]+e(Ni-Al)[%Al])}

APPENDIX E

Sigma plot values

Sigma plot values from Chapter 6.

Y=a.exp(b/X+c)

			Al	Ni	Mg
9.35	1.35	89.3	8.9	0.64	90.46
3.6	1.48	94.92	3.3	0.73	95.97
1.1	2.59	96.31	0.63	1.97	97.4
0	58	42	0	51.5	48.5

900 C

Parameter	Value	StdErr	CV(%)	Dependencies
a	5.48E+02	2.18E+01	3.98E+03	0.999787
b	1.12E+03	5.03E+01	4.49E+03	0.999992
c	2.47E+02	9.10E+00	3.69E+03	0.999988

R sq.=0.999997328 Norm=0.079569094

8.8	0.25	90.95	8.8	0.14	91.06
3.2	0.29	96.51	3	0.18	96.82
0.33	1.37	98.3	0.26	0.97	98.77
0	37.5	62.5	0	32	68

800 C

Parameter	Value	StdErr	CV(%)	Dependencies
a	5.48E+02	2.18E+01	3.98E+03	0.999787
b	1.12E+03	5.03E+01	4.49E+03	0.999992
c	2.47E+02	9.10E+00	3.69E+03	0.999988

R sq.=0.999999529 Norm=0.029941434

700 C

Parameter	Value	StdErr	CV(%)	Dependencies
a	2.50E+02	1.07E+03	4.27E+05	0.999888
b	1.65E+03	4.32E+03	2.61E+05	0.999988
c	3.30E+02	5.87E+02	1.78E+05	0.999974

R sq.=0.997179973 Norm=1.695992291

650 C

Parameter	Value	StdErr	CV(%)	Dependencies
a	1.40E+02	7.16E+02	5.12E+05	0.999951
b	1.41E+03	4.05E+03	2.87E+05	0.999995
c	2.60E+02	5.04E+02	1.94E+05	0.999988

R sq.=0.998239942 Norm=1.147349962